

TRANSITION METAL (OXY)NITRIDES AND OXIDES FOR ENERGY  
MATERIALS

A Dissertation

Presented to the Faculty of the Graduate School

of Cornell University

In Partial Fulfillment of the Requirements for the Degree of

Doctor of Philosophy

by

Ryo Henry Wakabayashi

August 2016

© 2016 Ryo Henry Wakabayashi

# TRANSITION METAL (OXY)NITRIDES AND OXIDES FOR ENERGY MATERIALS

Ryo Henry Wakabayashi, Ph. D.

Cornell University 2016

In order to fulfill the increasing demands for electricity without further contributions to climate change, we must generate and store electricity using carbon-free sources. Although fuel cells are a promising emerging candidate as an environmentally friendly alternative to internal combustion engines, there are several materials-related challenges that need to be addressed in order to improve performance and lower the cost of fuel cells. The catalyst support, carbon, is not thermodynamically stable under operating conditions, leading to corrosion over time. In addition, the catalyst at the cathode, Pt, is both inefficient and expensive.

Many nitrides and oxynitrides are conductive, durable and resistant to oxidation, making them especially attractive as fuel cell catalyst support. I prepared mesoporous mixed metal oxynitrides of various compositions by a co-precipitation method and subsequent ammonolysis. I investigated the effects of combination of several metal oxynitrides in terms of chemical and electrochemical stability in acidic and alkaline environments.

Many oxides are also conductive and durable, especially in alkaline media. Several conductive oxides have been reported as potentially useful alternatives to platinum as catalysts for the oxygen reduction reaction (ORR). In order to explore this

relatively new field, several collaborators have deposited thin film oxides. I developed an apparatus to perform rotating disk electrode voltammetry (RDE) using thin films as the electrode, enabling a quantitative characterization. By using the apparatus, I identified a very attractive oxide, albeit unreported in the literature. I synthesized the compound in powder form. The powder sample showed catalytic activities comparable to Pt in activity for the ORR, and comparable to  $\text{RuO}_2$  for the OER.

Lithium-ion batteries are one of the most promising energy storage devices. However, with the theoretical capacity of the current anode technology under 400 mAh/g and with the cathode even lower, development of new materials for both anodes and cathodes is crucial for advancement in energy storage. Metal nitrides react with lithium at low voltage, which makes them viable candidates as alternative materials as anodes in lithium-ion batteries. I investigated capacity and cyclability of metal nitride anodes as a function of metal compositions as well as annealing temperatures.

## BIOGRAPHICAL SKETCH

Ryo H. Wakabayashi and his twin brother grew up in the suburbs of Tokyo, Japan, and moved to the San Francisco Bay Area when he was in 6<sup>th</sup> grade. While the transition to a completely different culture was difficult, his passion for baseball helped him learn the language and adjust to the new environment.

He had always liked math and science, but his decision to pursue a degree in science was heavily influenced by his AP Chemistry, AP Physics and AP Biology teachers, Mr. Paul, Mr. Fortgang, and Ms. Hamilton (since deceased), who made science exciting, challenging, and yet very easy to understand. He attended the University of California, Berkeley, where he chose to major in Chemistry, as he thought that a way to make a difference in the world was to partake in a research on alternative energy materials. He started doing research in the fall semester of his sophomore year, an unusually early start for someone at a top-tier research university, under the guidance of Prof. Angy Stacy and her graduate students, first Jocelyn Scheintaub and then Daniel Kelly. Ryo credits the Stacy group for his fondness in research science, which heavily impacted his decision to pursue a graduate degree in chemistry.

Immediately following graduation from Berkeley, he arrived at Cornell, where he started working under Profs. DiSalvo and Abruña.

To my family and friends, especially Kei

## ACKNOWLEDGMENTS

I would first like to thank my advisors, Prof. Frank DiSalvo and Prof. Héctor Abruña. I chose to study chemistry specifically because I wanted to work on alternative energy-related materials, and they gave me the opportunity that I coveted, in addition to being caring and patient mentors. I do not think I could have found a better situation for myself. I would also like to thank Prof. Tobias Hanrath for helpful discussions on my research, as well.

I would also like to thank my collaborators and colleagues. I have had the privilege of working with many collaborators, including but not limited to Dr. Hanjong Paik (Schlom group), Xin Huang (Brock group), Marc Murphy (van Dover group), and Elliot Padget (Muller group). I would like to thank every DiSalvo and Abruña group members as well, especially Dr. James McKone, Dr. Eric Rus, Dr. Jie Gao, Abby Van Wassen, James Pastore, and Dr. Minh Nguyen, for extensive discussions, mentorship and collaborations. In addition, I would like to thank staff scientists, members and building managers, including but not limited to Mick Thomas (CCMR), John Grazul (CCMR), Steve Kriske (CCMR), Kelly Case (chemistry), Suzanne Koehl (EMC<sup>2</sup>), Dave Niesh (chemistry/building), Larry Stull (chemistry/building) for their assistance and support.

I was also blessed to have amazing friends here at Cornell. I could not have survived here without their support. I would like to thank all of my friends, from my intramural sports teammates to Ryan Dwyer, my roommate for two years.

Finally, I would like to thank my family members for their support, though all the ups and downs.

## TABLE OF CONTENTS

Biographicla Sketch .....	iv
Acknowledgments .....	vii
Table of Contents .....	viii
List of Figures.....	xiii
List of Tables.....	xxii
1. Introduction to Alternative Energy Systems	
1.1 Introduction to Fuel Cells And Batteries .....	1
1.1.1 Non-fossil Fuel Energy .....	1
1.1.2 Fuel Cells .....	1
1.1.3 Lithium-ion Batteries .....	4
1.2 Outline of the Dissertation .....	6
References .....	8
2. Synthesis and Electrochemical Characterization of $Ti_xTa_yAl_zN_{1-\delta}O_\gamma$ for Fuel Cell Catalyst Supports	
2.1 Abstract .....	10
2.2 Introduction .....	10
2.3 Experimental	
2.3.1 Synthesis of rock-salt $Ti_xTa_yAl_zN_{1-\delta}O_\gamma$ ( $x+y+z = 1$ ) .....	13
2.3.2 Synthesis/Deposition of Pt nanoparticles .....	14
2.3.3 Physical Characterization .....	14
2.3.4 Stability Testing .....	14
2.3.5 Electrochemical Characterization .....	15
2.4 Results and Discussions	

2.4.1	Structure and Compositions .....	16
2.4.2	Conductivity Measurements .....	22
2.4.3	Surface Area .....	23
2.4.4	Additional Discussion on Effects of Zn .....	24
2.4.5	Electrochemical Behavior	
	2.4.5.1 Acidic Media .....	27
	2.4.5.2 Alkaline Media .....	28
2.4.6	Chemical Stability	
	2.4.6.1 Acidic Media .....	31
	2.4.6.2 Alkaline Media .....	33
2.4.7	Pt Deposition and Electrochemistry Using Pt/ Ti <sub>x</sub> Ta <sub>y</sub> Al <sub>z</sub> N <sub>1-x-y-z</sub> δO <sub>γ</sub> .....	36
2.5	Conclusions .....	39
2.6	Future Directions .....	40
2.7	Acknowledgments .....	40
	References .....	40
3.	Methods: Rotating Disk Electrode Voltammetry of Thin Films of Novel Oxide Materials	
3.1	Abstract .....	45
3.2	Introduction .....	45
3.3	Methods/Description of the Instrument	
	3.3.1 Instrumentation .....	48
	3.3.2 EIS .....	50
	3.3.3 CV and RDE .....	50
	3.3.4 Deposition Methods	
	3.3.4.1 Au .....	51

3.3.4.2 MBE .....	51
3.3.4.3 Co-sputtering .....	52
3.4 Operations/Results and Discussions	
3.4.1 EIS .....	54
3.4.2 CV and RDE of $K_3[Fe(CN)_6]$ .....	56
3.4.3 ORR on Pt thin film .....	59
3.4.4 ORR and OER on MBE Samples(from the Schlom Group) .....	60
3.4.5 ORR and OER on Co-sputtered Samples (from the van Dover Group) .....	63
3.5 Conclusions .....	66
References .....	67
4. New $Mn_xRu_{1-x}O_2$ ( $x \leq 0.2$ ), a High Performance, Low Cost Catalyst for the Oxygen Reduction and Evolution Reactions	
4.1 Abstract .....	71
4.2 Introduction .....	71
4.3 Experimental	
4.3.1 Synthesis of the Powder $Mn_xRu_{1-x}O_2$ ( $x \leq 0.2$ ) .....	75
4.3.2 Physical Characterization .....	76
4.3.3 Electrochemical Characterization .....	76
4.4 Results and Discussions .....	78
4.5 Conclusions .....	92
4.6 Future Directions .....	92
4.7 Acknowledgements .....	92
References .....	93

5. Performance and Mechanism of Niobium (Oxy)nitrides as Lithium-ion Battery Anode	
5.1 Introduction .....	97
5.2 Experimental	
5.2.1 Synthesis of $Nb_{1-x}O_xN_{1-\gamma}$ .....	101
5.2.2 Physical Characterization .....	101
5.2.3 Coin Cell Testing .....	102
5.2.4 <i>Operando</i> X-ray Diffraction and X-ray Absorption Spectroscopy .....	102
5.3 Results and Discussions	
5.3.1 Survey of a Few Metal Nitrides .....	103
5.3.2 In-depth Look at Niobium (Oxy)nitride .....	104
5.3.3 <i>Operando</i> X-ray Techniques .....	113
5.4 Conclusions .....	115
5.5 Future Directions .....	116
5.6 Acknowledgments .....	116
References .....	116
6. An attempt to Synthesize and Characterize Ionically Conductive Materials	
6.1 Introduction .....	119
6.2 Experimental	
6.2.1 Synthesis .....	123
6.2.2 Physical Characterization .....	124
6.2.3 Ionic Conductivity Measurement .....	124
6.3 Results and Discussions	
6.3.1 Development of Impedance Spectroscopy Methods ..	125
6.3.2 In Search of New Ionic Conductors .....	128

6.4 Conclusions and Future Directions .....	133
6.5 Acknowledgements .....	134
References .....	135
7. Concluding Remarks .....	137

## LIST OF FIGURES

<b>Figure 1.1.</b> Renewable energy generation (yellow: solar, blue: wind), and back up/storage needed (red) to meet energy demand (black line) in a typical winter week in Germany .....	1
<b>Figure 1.2.</b> Schematic of a fuel cell .....	3
<b>Figure 1.3.</b> Schematic of a lithium-ion battery .....	4
<b>Figure 2.1.</b> pXRD patterns of $Ti_xTa_yAl_zN_{1-\delta}O_\gamma$ (a) synthesized at 950 °C. (b) shows a zoomed region containing the first two peaks .....	17
<b>Figure 2.2.</b> Lattice constant as a function of x in $Ti_xTa_yAl_zN_{1-\delta}O_\gamma$ synthesized at 950 °C. Red dots: y=z (Ta = Al); purple dots: y = 0 (only Ti or Ta); green dot: literature value of TiN .....	18
<b>Figure 2.3.</b> Lattice constants as a function of x in $Ti_xTa_yAl_zN_{1-\delta}O$ where y=z. Red dots were samples heated under ammonia at 950 °C, pink at 800 °C .....	19
<b>Figure 2.4.</b> EDX results of atomic composition (atom %) of the $Ti_xTa_yAl_zN_{1-\delta}O_\gamma$ samples (nominal ratios in quotation marks) synthesized at 800 °C. Error bars are one standard deviation calculated from ten measurements. ....	20
<b>Figure 2.5.</b> SEM images of of $Ti_xTa_yAl_zN_{1-\delta}O_\gamma$ synthesized at 800 °C where x:y:z = (a) 1:0:0, (b) 0.7:0.15:0.15, (c) 0.33:0.33:0.33, (d) 0.7:0.3:0 and (e) 0.7:0:0.3. Scale bars are 200 nm. ....	24
<b>Figure 2.6.</b> pXRD patterns of $Ti_{0.33}Ta_{0.33}Al_{0.33}O_x$ , with various amount of zinc oxide. Numbers are molar ratios of Zn: (Ti+Ta+Al) .....	25
<b>Figure 2.7.</b> SEM images of of $Ti_{0.33}Ta_{0.33}Al_{0.33}N_{1-\delta}O_\gamma$ , with varying amount of zinc ions in oxide precursor: a) no Zn b) Zn: (Ti+Ta+Al) = 1:1, c) 2:1, d) 4:1 and e) 6:1.	

Scale bars are 200 nm. .... 26

**Figure 2.8.** BET surface area of samples made with Zn precursors (“with Zn”) and without Zn. “with Zn” data are replication of Table 2.3. Error bars are sample standard deviation. .... 26

**Figure 2.9.** Cyclic voltammograms of  $Ti_xTa_yAl_zN_{1-\delta}O_\gamma$  synthesized at 800 °C where  $x:y:z =$  (a) 1:0:0, (b) 0.7:0.15:0.15, (c) 0.33:0.33:0.33, (d) 0.7:0.3:0 and (e) 0.7:0:0.3 in 0.1M  $H_2SO_4$ , scanned continuously for 24 h at 50 mV/s. Shown CVs are taken at 0 h (blue), 4 h (red) and 24 h (green) after the start of the experiment. (f) is Vulcan XC-72 as a comparison. .... 28

**Figure 2.10.** Cyclic voltammograms of  $Ti_xTa_yAl_zN_{1-\delta}O_\gamma$  where  $x:y:z =$  (a) 1:0:0, (b) 0.7:0.15:0.15, (c) 0.33:0.33:0.33, (d) 0.7:0.3:0 and (e) 0.7:0:0.3 in 0.1M NaOH, scanned continuously for 24 h at 50 mV/s. Shown CVs are taken at 0 h (blue), 4 h (red) and 24 h (green) after start of the experiment. (f) is the glassy carbon substrate. .... 29

**Figure 2.11** Cyclic voltammograms of  $Ti_xTa_yAl_zN_{1-\delta}O_\gamma$  where  $x:y:z =$  (a) 1:0:0, (b) 0.7:0.15:0.15, (c) 1:0:0, ink made without Nafion (binder) and (d) 0.7:0.15:0.15, ink made without Nafion in 0.1M NaOH, scanned continuously for 24 h at 50 mV/s. Shown CVs are taken at 0 h (blue), 4 h (red) and 24 h (green) after start of the experiment. .... 29

**Figure 2.12.** pXRD patterns and photographs (bottom) of  $Ti_xTa_yAl_zN_{1-\delta}O_\gamma$  samples synthesized at 800 °C after 21 days of stability testing in 0.1M  $H_2SO_4$  at 60°C. In the photograph, the particles in vials (a) and (e) are white. .... 31

**Figure 2.13.** EDX results of  $Ti_xTa_yAl_zN_{1-\delta}O_\gamma$  samples (nominal ratio in quotation

marks; synthesized at 800 °C) after 21 days of stability testing in 0.1M H<sub>2</sub>SO<sub>4</sub> at 60°C.  
 Error bars are one standard deviation calculated from ten measurements. .... 32

**Figure 2.14.** SEM images of Ti<sub>x</sub>Ta<sub>y</sub>Al<sub>z</sub>N<sub>1-δ</sub>O<sub>γ</sub> synthesized at 800 °C where x:y:z = (a) 1:0:0, (b) 0.7:0.15:0.15, (c) 0.33:0.33:0.33, (d) 0.7:0.3:0 and (e) 0.7:0:0.3 after 21 days of stability test in 0.1M H<sub>2</sub>SO<sub>4</sub> at 60°C. Scale bars are 200 nm. .... 32

**Figure 2.15.** pXRD patterns and photographs (inset) of Ti<sub>x</sub>Ta<sub>y</sub>Al<sub>z</sub>N<sub>1-δ</sub>O<sub>γ</sub> samples after 21 days of stability test in 0.1M NaOH at 60 °C. .... 34

**Figure 2.16.** SEM images of Ti<sub>x</sub>Ta<sub>y</sub>Al<sub>z</sub>N<sub>1-δ</sub>O<sub>γ</sub> synthesized at 800 °C where x:y:z = (a) 1:0:0, (b) 0.7:0.15:0.15, (c) 0.33:0.33:0.33, (d) 0.7:0.3:0 and (e) 0.7:0:0.3 after 21 days of stability test in 0.1M NaOH at 60°C. Scale bars are 200 nm. .... 35

**Figure 2.17.** EDX results of Ti<sub>x</sub>Ta<sub>y</sub>Al<sub>z</sub>N<sub>1-δ</sub>O<sub>γ</sub> samples (nominal ratio in quotation marks; synthesized at 800 °C) after 21 days of stability testing in 0.1M NaOH at 60°C. Error bars are one standard deviation calculated from ten measurements..... 35

**Figure 2.18.** pXRD patterns of Pt/Ti<sub>x</sub>Ta<sub>y</sub>Al<sub>z</sub>N<sub>1-δ</sub>O<sub>γ</sub>. .... 36

**Figure 2.19.** SEM images of Pt/Ti<sub>x</sub>Ta<sub>y</sub>Al<sub>z</sub>N<sub>1-δ</sub>O<sub>γ</sub> synthesized at 800 °C where x:y:z = (a) 1:0:0, (b) 0.7:0.15:0.15, (c) 0.7:0.3:0. Scale bars are 20 nm. .... 37

**Figure 2.20.** Representative bright-field TEM images of Pt/Ti<sub>x</sub>Ta<sub>y</sub>Al<sub>z</sub>N<sub>1-δ</sub>O<sub>γ</sub> synthesized at 800 °C where x:y:z = 1:0:0 (left), 0.7:0.15:0.15 (right). Scale bars are 50 nm. Rod-like objects on the right are parts of the TEM grid. .... 37

**Figure 2.21.** Stationary CVs of Pt/nitride samples of Ti<sub>x</sub>Ta<sub>y</sub>Al<sub>z</sub>N<sub>1-δ</sub>O<sub>γ</sub> where x:y:z = (a) 1:0:0, (b) 0.7:0.15:0.15, (c) Pt/C in 0.1M H<sub>2</sub>SO<sub>4</sub>, scanned continuously for 24 h at 20 mV/s. Shown CVs are taken at 0 h (blue), 8 h (red) and 24 h (green) after start of

the experiment. ....	39
<b>Figure 2.22.</b> RDE voltammograms (1600 rpm) of representative samples of (a) Pt / TiN <sub>1-δ</sub> O <sub>γ</sub> (20 wt. %) and (b) Pt / Ti <sub>0.7</sub> Ta <sub>0.15</sub> Al <sub>0.15</sub> N <sub>1-δ</sub> O <sub>γ</sub> (20 wt. %) synthesized at 800 °C in O <sub>2</sub> -saturated 0.1M H <sub>2</sub> SO <sub>4</sub> , taken at the start of the experiment, 8 hours after the start, and 24 hours after the start of the experiment. (c) is Pt/C for comparison. ....	39
<b>Figure 3.1.</b> Schematic of the custom-made rotating disc electrode system. ....	48
<b>Figure 3.2.</b> Photographs of the custom-made 3-compartment electrochemical cell and the custom-made rotating disk electrode. Ruler unit is in inches. ....	50
<b>Figure 3.3.</b> Nyquist plots of Au film (blue) and bulk Au (red) in 0.1M KCl, at OCP, 5 mV AC, 20,000 Hz – 1 Hz (Z' and Z'' increase as the frequency decreases) ....	55
<b>Figure 3.4.</b> Nyquist plots of Au film with RE in its own compartment (red) and with the reference electrode moved directly adjacent to the working electrode (blue) in 0.1M KCl, at OCP, 5 mV AC, 20,000 Hz – 1 Hz (Z' and Z'' increase as the frequency decreases) ....	55
<b>Figure 3.5.</b> Cyclic voltammograms of bulk (a) and film (b) Au in 0.1M KCl. Scan rate 20 mV/s. Red: potential range used for CV of K <sub>3</sub> [Fe(CN) <sub>6</sub> ]. ....	56
<b>Figure 3.6.</b> Cyclic voltammogram of 0.81 mM K <sub>3</sub> [Fe(CN) <sub>6</sub> ] in 0.1 M KCl on bulk (a) Au and sputtered gold (approx. 50 nm thick; b), and peak-to-peak separations of the oxidation and reduction peaks (c is for bulk Au, d is for thin film Au). Scan rates are 10 (red), 20 (orange), 50 (mustard), 70 (light green), 85 (green) and 100 (light blue) mV/s. ....	57
<b>Figure 3.7.</b> Rotating disk electrode voltammetry of 0.81 mM K <sub>3</sub> [Fe(CN) <sub>6</sub> ] in 0.1 M KCl on bulk Au (a) and Au film (b). (c) Levich plots at 0.06 V vs. Ag/AgCl of bulk	

Au and Au film (d). .....	59
<b>Figure 3.8</b> (a) RDE voltammogram of sputtered Pt in oxygen-saturated 0.1M NaOH, measured using a home-made electrode setup. (b) Levich plot, generated from current densities at -0.4 V (green), -0.6 V (red) and -0.8 V (blue) vs. Ag/AgCl, with equations for the linear regression lines for the data from -0.6V and -0.8 V. ....	60
<b>Figure 3.9</b> Nyquist plots of selected MBE pyrochlore samples. A glassy carbon electrode is a standard electrode (the RDE electrode setup described in this work is not used). OCP, 10 mV AC, 20,000 Hz – 1 Hz ( $Z'$ and $Z''$ increase as the frequency decreases). .....	61
<b>Figure 3.10.</b> (a) RDE metacomparison of the oxygen reduction reaction in oxygen-saturated 0.1M NaOH using MBE-grown pyrochlore electrodes. The voltammogram of Pt is copied from Figure 2 (b) Comparison of OER in oxygen-saturated 0.1M NaOH using MBE-grown pyrochlore electrodes. Dotted lines indicate different samples of the same nominal composition. (c) (d) (e) are part (a) divided into three groups of compounds. Colors are matched for same samples on (a) and (b). All samples are (111), unless otherwise specified. ....	63
<b>Figure 3.11.</b> (a) RDE metacomparison of ORR in O <sub>2</sub> -saturated 0.1 M NaOH using thin film oxide samples deposited by co-sputtering methods. The voltammogram of Pt is copied from Figure 2. (b) Comparison of OER in oxygen-saturated 0.1M NaOH using thin film oxide samples deposited by co-sputtering methods. Colors are matched between (a) and (b). .....	65
<b>Figure 3.12.</b> RDE voltammograms of Mn <sub>x</sub> Ru <sub>y</sub> O <sub>2</sub> “E8” in O <sub>2</sub> -saturated 0.1 M NaOH. Inset: Levich plot from current densities at -0.6 V vs. Ag/AgCl. ....	66

**Figure 4.1.** (a) X-ray diffraction patterns of  $\text{Mn}_{0.2}\text{Ru}_{0.8}\text{O}_2$  (red),  $\text{RuO}_2$  (blue),  $\text{Mn}_{0.33}\text{Ru}_{0.67}\text{O}_2$  (green), of  $\text{Mn}_{0.2}\text{Ru}_{0.8}\text{O}_2$  heated at 160 °C in ambient air (purple),  $\text{Mn}_{0.2}\text{Ru}_{0.8}\text{O}_2$  made with carbon black in the bomb autoclave (navy), and  $\beta\text{-MnO}_2$  (orange). (b): zoom of the first three major peaks of  $\text{Mn}_{0.2}\text{Ru}_{0.8}\text{O}_2$  (red),  $\text{RuO}_2$  (blue), and  $\beta\text{-MnO}_2$  (orange). with labels of lattice planes for  $\text{RuO}_2$  peaks and black lines drawn at peak locations of  $\text{RuO}_2$ . Peaks of  $\text{Mn}_{0.2}\text{Ru}_{0.8}\text{O}_2$  are slightly shifted from  $\text{RuO}_2$ , especially the peaks with lattice planes that do not contain a z component, indicating some lattice constant change. .... 79

**Figure 4.2.** Lattice constants (a on left, c on right) of the rutile structure products as a function of % Ru. Red dots are literature values of  $\beta\text{-MnO}_2$  and  $\text{RuO}_2$ . ....79

**Figure 4.3.** X-ray diffraction patterns of  $\text{Mn}_{0.2}\text{Ru}_{0.8}\text{O}_2$  (red), another sample of  $\text{Mn}_{0.2}\text{Ru}_{0.8}\text{O}_2$  heated at 160 °C in ambient air (light purple), and  $\text{Mn}_{0.2}\text{Ru}_{0.8}\text{O}_2$  heated at 160 °C in ambient air (darker purple). Darker purple and red traces are replicated from Figure 4.1. .... 81

**Figure 4.4.** SEM images of  $\text{Mn}_{0.2}\text{Ru}_{0.8}\text{O}_2$  (a and b),  $\text{RuO}_2$  (c),  $\text{MnO}_2$  (d), and  $\text{Mn}_{0.2}\text{Ru}_{0.8}\text{O}_2$  made without using a bomb autoclave (e). Scale bars are 200 nm. .... 83

**Figure 4.5.** High-resolution EELS image of  $\text{Mn}_{0.2}\text{Ru}_{0.8}\text{O}_2$ , after removing noise by principal component analysis. Region in red dotted box on the top right was mapped. Mn is red and Ru is cyan in the bottom left (Image by Elliot Padgett) ..... 84

**Figure 4.6.** RDE voltammograms of  $\text{Mn}_{0.2}\text{Ru}_{0.8}\text{O}_2/\text{C}$  in  $\text{O}_2$ -saturated 0.1 M NaOH. Inset: Levich plot from current densities at -0.8 V vs. Ag/AgCl. .... 85

**Figure 4.7.** RDE voltammograms (1600 rpm) of  $\text{Mn}_{0.2}\text{Ru}_{0.8}\text{O}_2/\text{C}$  (red),  $\text{RuO}_2/\text{C}$  (blue), and  $\beta\text{-MnO}_2/\text{C}$  (yellow), carbon black (green),  $\text{Mn}_{0.2}\text{Ru}_{0.8}\text{O}_2$  “E8” thin film (pink, by Murphy in Ch. 3), phase-segregated “ $\text{Mn}_{0.2}\text{Ru}_{0.8}\text{O}_2$ ”/C (purple), physical mixture of  $\text{MnO}_2/\text{RuO}_2/\text{C}$  (2:8 Mn:Ru metal basis, brown), physical mixture of  $\text{Mn}_2\text{O}_3/\text{RuO}_2/\text{C}$  (2:8 Mn:Ru metal basis, magenta), and Pt/C (gray) in  $\text{O}_2$ -saturated 0.1 M NaOH..... 87

<b>Figure 4.8.</b> Rotation-rate normalized RDE voltammograms of $\text{Mn}_{0.2}\text{Ru}_{0.8}\text{O}_2$ in $\text{O}_2$ -saturated 0.1 M NaOH. ....	89
<b>Figure 4.9.</b> RDE voltammogram of $\text{Mn}_{0.2}\text{Ru}_{0.8}\text{O}_2/\text{C}$ (a; partial reproduction of previous figure) and of $\text{Mn}_{0.2}\text{Ru}_{0.8}\text{O}_2$ without C (b), at 0 h and after 2000 CVs (lighter shade). ....	90
<b>Figure 4.10.</b> Linear sweep voltammograms in $\text{O}_2$ -saturated 0.1 M NaOH, investigating the OER, of $\text{Mn}_{0.2}\text{Ru}_{0.8}\text{O}_2/\text{C}$ (red), $\text{RuO}_2$ (blue), and $\beta\text{-MnO}_2$ (yellow), carbon black (green), $\text{Mn}_{0.2}\text{Ru}_{0.8}\text{O}_2$ “E8” thin film (magenta), phase-segregated “ $\text{Mn}_{0.2}\text{Ru}_{0.8}\text{O}_2$ ”/C (purple), physical mixture of $\text{MnO}_2/\text{RuO}_2/\text{C}$ (2:8 Mn:Ru metal basis, brown), and physical mixture of $\text{Mn}_2\text{O}_3/\text{RuO}_2/\text{C}$ (2:8 Mn:Ru metal basis, magenta) in $\text{O}_2$ -saturated 0.1 M NaOH. ....	91
<b>Figure 4.11.</b> (a) Linear region used to calculate the Tafel slope, and their values. Purple line is on top of the red line. (b) Tafel plot. ....	91
<b>Figure 5.1.</b> A simple schematic of the experimental set-up of X-ray Absorption Spectroscopy, taken from DeBeer. ....	103
<b>Figure 5.2.</b> (a) Discharge capacities of various metal nitride samples prepared by Dr. Minghui Yang (except NbN, which is my own work). (b) pXRD of the highest-capacity VN, cast on Cu. Red and blue lines are database peaks of ammonium metavanadate (red) and copper (blue) respectively. ....	104
<b>Figure 5.3.</b> Powder XRD patterns of $\text{Nb}_{1-x}\square_x\text{O}_\gamma\text{N}_{1-\gamma}/\text{C}$ , made under flowing $\text{NH}_3$ at different synthesis temperatures. ....	105
<b>Figure 5.4.</b> TEM image of $\text{Nb}_{1-x}\square_x\text{O}_\gamma\text{N}_{1-\gamma}$ , synthesized at 500 °C. ....	105
<b>Figure 5.5</b> Charge-discharge curves (red: 1 <sup>st</sup> cycle; blue: 2 <sup>nd</sup> cycle) of $\text{Nb}_{1-x}\square_x\text{O}_\gamma\text{N}_{1-\gamma}$ synthesized at (a) 500 °C (b) 600 °C (c) 700 °C (d) 800 °C. Cycled at 20 mA/h (approx. C/50). ....	107
<b>Figure 5.6.</b> Charge-discharge curves (red: 1 <sup>st</sup> cycle; blue: 2 <sup>nd</sup> cycle) of niobium oxide	

(made at 450 °C). Two different curves are from two different coin cells. Cycled at C/20. ....	107
<b>Figure 5.7.</b> Discharge capacity of $\text{Nb}_{1-x}\text{O}_x\text{N}_{1-\gamma}$ over 100 cycles. Cycled at 20 mAh/g (C/50). Blue trace is still cycling as of this writing. ....	108
<b>Figure 5.8.</b> Powder patterns of $\text{Nb}_{1-x-y}\text{M}_y\text{O}_x\text{N}_{1-\gamma}$ , where M = Al (blue), Ta (red), Si (yellow and green) made under flowing $\text{NH}_3$ at 500 °C. Black trace is a replication from Figure 5.2, as a comparison/reference. ....	109
<b>Figure 5.9.</b> Discharge capacity of $\text{Nb}_{1-x-y}\text{M}_y\text{O}_x\text{N}_{1-\gamma}$ over 100 cycles. M = Al cycled at approximately C/50, all others at C/20. ....	110
<b>Figure 5.10.</b> Discharge capacity of $\text{Nb}_{1-x}\text{O}_x\text{N}_{1-\gamma}$ made at 700 °C, cycled at 20 mAh/g (approx. C/50, blue) and C/20 (purple). Blue trace is a replication from Figure 5.7. ....	112
<b>Figure 5.11.</b> <i>Operando</i> XRD diffraction of $\text{Nb}_{1-x}\text{O}_x\text{N}_{1-\gamma}$ (made at 500 °C). Curve on the left is the charge-discharge behavior, and the colored graph on the right side is the XRD peaks at corresponding state. The black streaks correspond to beam fill at CHESS. (Figure by James Pastore) ....	113
<b>Figure 5.12.</b> <i>Operando</i> XAS of $\text{Nb}_{1-x}\text{O}_x\text{N}_{1-\gamma}$ (made at 500 °C), (a) discharge process and (b) charge process. (c) Summarizes the beginning and end of scans shown in (a) and (b). (Figure by James Pastore) ....	115
<b>Figure 6.1.</b> Binary metal oxides that are thermodynamically stable upon contact with metallic lithium (a) and metallic sodium (b) are highlighted in yellow. ....	121
<b>Figure 6.2.</b> pXRD patterns of $\text{Li}_7\text{La}_3\text{Zr}_2\text{O}_{12}$ . (b) is a zoom into 10-40°. Vertical lines are database peak locations for cubi and tetragonal polymorphs of $\text{Li}_7\text{La}_3\text{Zr}_2\text{O}_{12}$ . ...	126

<b>Figure 6.3.</b> Images of the Electrochemical cell used for all-solid-state EIS. ....	127
<b>Figure 6.4.</b> Nyquist Plot of $\text{Li}_7\text{La}_3\text{Zr}_2\text{O}_{12}$ , taken at 40 mV AC (red) and 10 mV AC (green). (b) is a zoomed-in plot of (a) at low Z (or high frequency). AC frequency 1 MHz to 1 Hz ( $Z'$ and $Z''$ increase as the frequency decreases) (c) is the model used for fitting. ....	128
<b>Figure 6.5.</b> pXRD of mixture of $\text{Li}_2\text{O}:\text{CaO}:\text{Al}_2\text{O}_3$ mixed in 1:2:7 ratio (using Pechini method), and heated at 900 °C. The vertical lines are database peak locations for the phases indicated. (b) is a zoomed version of (a). ....	130
<b>Figure 6.6.</b> Phase diagram of $\text{Li}_2\text{O}-\text{CaO}-\text{Al}_2\text{O}_3$ , at 900 °C. Blue dots: experimental reactant compositions; red dots = known phases, brown lines = sides of compatibility triangles implied from the obtained diffraction patterns. ....	131
<b>Figure 6.7.</b> pXRD of mixture of $\text{Na}_2\text{O}:\text{La}_2\text{O}_3:\text{Al}_2\text{O}_3$ mixed in 1:2:7 ratio (using Pechini method), and heated at 1000 °C. The vertical lines are database peak locations. ....	132
<b>Figure 6.8.</b> Phase diagram of $\text{Na}_2\text{O}-\text{La}_2\text{O}_3-\text{Al}_2\text{O}_3$ , at 1000 °C. Blue dots: experimental reactant compositions, red dots = known phases, brown lines = sides of compatibility triangles, implied from the obtained diffraction peaks. Points circled in green only showed majority $\text{LaAlO}_3$ peaks. ....	133

## LIST OF TABLES

<b>Table 2.1.</b> N/O/H amounts and corresponding proposed chemical formulas of the $Ti_xTa_yAl_zN_{1-\delta}O_\gamma$ samples synthesized at 800 °C. Mol of every ions is normalized so sum of anions add up to 1. ....	21
<b>Table 2.2.</b> Powder conductivity of $Ti_xTa_yAl_zN_{1-\delta}O_\gamma$ samples synthesized at 800 °C measured using home-built powder conductivity measurement device. ....	22
<b>Table 2.3.</b> Surface area and standard deviation of the $Ti_xTa_yAl_zN_{1-\delta}O_\gamma$ synthesized at 800 °C. ....	23
<b>Table 2.4.</b> Particle size analysis (average and standard distribution) of Pt particles on $Ti_xTa_yAl_zN_{1-\delta}O_\gamma$ from analyses of at least 100 particles. ....	37
<b>Table 4.1.</b> EDX results of $Mn_{0.2}Ru_{0.8}O_2$ made with and without using the bomb autoclave. Standard deviation calculated from at least 8 measurements. ....	81
<b>Table 5.1.</b> Calculated theoretical capacities of metal nitrides as lithium-ion battery anodes, and carbon for comparison. Molar mass of C is for “C <sub>6</sub> ”. ....	99
<b>Table 5.2.</b> Number of Nb, cationic vacancies, O, and N, if the product is written as $Nb_{1-\square}O_\gamma N_{1-\gamma}$ , and average oxidation state of Nb as a result. “***” indicates an unphysical value, but we attribute that to sampling error (less than 3%).....	111

## CHAPTER 1

### INTRODUCTION TO ALTERNATIVE ENERGY SYSTEMS

#### *1.1 Introduction to Fuel Cells and Batteries*

##### *1.1.1 Non-fossil Fuel Energy*

Since the industrial revolution, the human population has relied heavily on fossil fuels to meet its energy demands. As a result, CO<sub>2</sub> levels in the atmosphere have reached their highest<sup>1</sup> in recorded history, which has resulted in global warming and all the undesired consequences associated with it. Therefore it is clear that, in order to sustain (and improve in the developing world) our lifestyle, a shift to renewable energies is dearly needed. Harnessing solar energy is likely a promising and plausible contribution to that end, but our energy use and the sun are almost completely phase-mismatched (Figure 1.1), and the sparseness of sunlight makes it difficult to directly power automobiles (and other vehicles) from the sunlight. In other words, there is a clear need to store the energy from the sunlight.

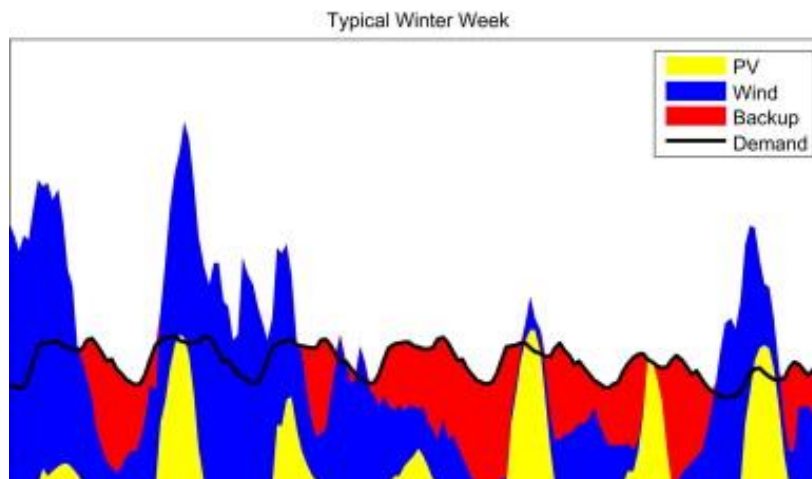
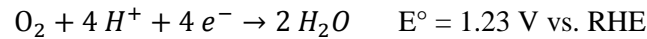


**Figure 1.1** Renewable energy generation (yellow: solar, blue: wind), and back up/storage needed (red) to meet energy demand (black line) in a typical winter week in Germany<sup>2</sup>

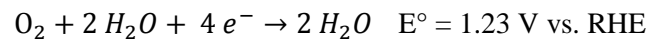
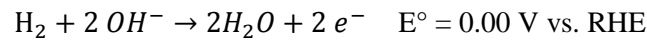
##### *1.1.2 Fuel Cells*

One possible storage technology is to generate hydrogen using the energy from the sun, store it, and use that it a fuel to power fuel cells, a “holy grail” of renewable energy as

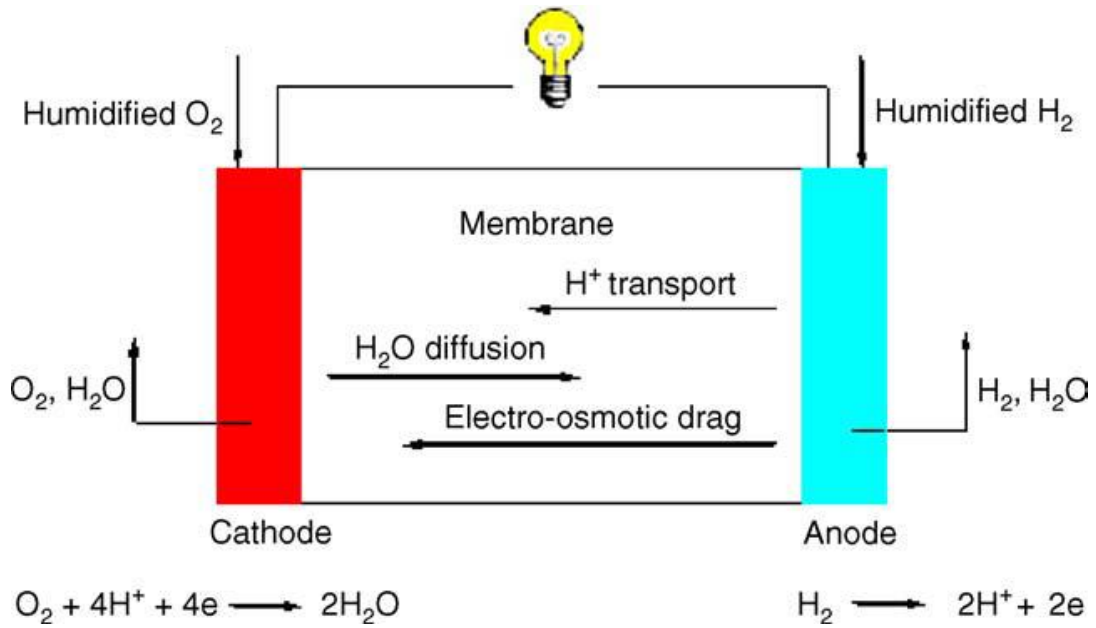
described by two distinguished electrochemists back in 1995.<sup>2</sup> Fuel cells convert the chemical energy of a fuel and oxidant (typically hydrogen and oxygen from air, respectively) into electrical energy by the following reactions in polymer electrolyte membrane fuel cells (PEMFC):



Or, in alkaline fuel cells (AFC):



These two half-reactions do not produce any persistent greenhouse gasses (water vapor is a greenhouse gas, but excess water in the atmosphere precipitates in a short period cycle of days to weeks). In addition to being “clean”, fuel cells provide the possibility of a high energy density and a fast “charging process”, at least in comparison to batteries. The efficiencies of fuel cells are also not limited by the Carnot cycle as are heat-based fossil fuel technologies including internal combustion engines (ICE). Therefore, in theory, fuel cells can achieve much higher energy efficiencies than ICE can be achieved. In fact, DOE reports that the stack efficiencies of fuel cell stacks today are already over 50%<sup>3</sup>, much higher than those of ICE (about 20%<sup>4</sup>).



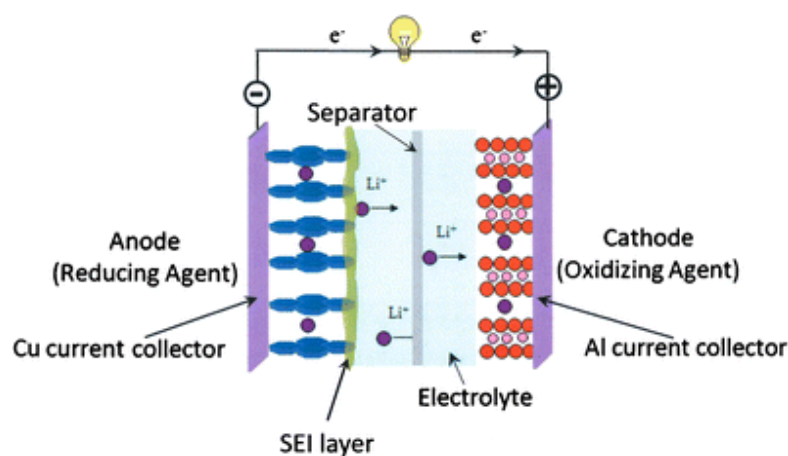
**Figure 1.2.** Schematic of a fuel cell<sup>5</sup>

Figure 1.2 shows a simple schematic of a single fuel cell. Fuel cells consist of gas diffusion layers, ion exchange membrane (typically Nafion in the case of PEMFC, as shown in Figure 2), and anode and cathode catalyst layers, which consist of catalysts (typically platinum) dispersed on a conductive support layer (carbon black). Multiple fuel cells are usually joined together by bipolar plates (represented by the black and the gray boxes) to form what is commonly called a fuel cell stack.

Many of the components listed above pose significant challenges to the wide scale deployment of fuel cells. Nafion is expensive, even though it has been over thirty years since its discovery. In fact, the Department of Energy estimates that it accounts for nearly 30 % of the cost of fuel cell stacks at low production rate (~1,000 systems/year).<sup>3</sup> The cost of Nafion, however, is expected to drop to 10% of the stack once mass-produced (500,000 stacks/year). However, mass-production does not help alleviate the high cost-per-stack of the platinum-containing catalyst layers. They account for approximately 20 % of the cost at low production and 45 % at mass-production scale. This is because the catalysts used for both the anode and

the cathode are Pt (or Pt-based), one of the most expensive and the least abundant metals. Also, the carbon support used to disperse Pt efficiently and make electrical connections to the rest of the system is not thermodynamically stable to corrosion under typical operating conditions<sup>6</sup>, which, as a result, shortens the lifespan of a fuel cell stack. Finally, in order to replace the internal combustion engine-based automobiles, a completely new infrastructure of hydrogen fill stations would have to be built to replace traditional gasoline stations.

### 1.1.3 Lithium-ion batteries

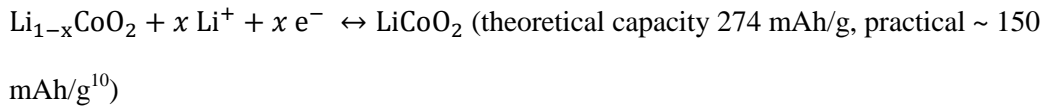
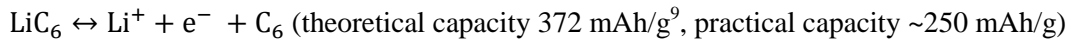


**Figure 1.3.** Schematic of a lithium-ion battery<sup>9</sup>

It is at least as appealing to convert the energy from the sunlight into electricity using photovoltaic cells and storing that electricity directly in the form of chemical energy. There are many types of secondary (rechargeable) batteries available commercially, but the most common, and the most promising, is the lithium-ion battery. Lithium is the lightest non-gas element and has the lowest formal reduction potential of any element, which makes its use highly advantageous in terms of energy density. Realization of the intercalation chemistry by Whittingham in the 1970s<sup>7</sup> revolutionized energy storage. Figure 1.3 (taken from Goodenough et al.<sup>8</sup>) shows a schematic of a lithium-ion battery. In a typical lithium-ion battery, graphitic carbon is used as the anode and a layer-structured oxide, such as LiCoO<sub>2</sub>, LiFePO<sub>4</sub>, LiMn<sub>2</sub>O<sub>4</sub>, and Li(Ni, Mn, Co)O<sub>2</sub> mixed with carbon, is used as the cathode. All of these electrodes are

so-called intercalation electrodes, in which lithium diffuses in and out of the material with minimal structural changes.

Assuming that the anode is graphitic carbon and cathode is  $\text{LiCoO}_2$ , the two half-reactions are as follows:



These reactions are, as mentioned above, intercalation reactions. As such, the benefit of these two half-reaction is that is that the solid phases do not change their structure. This is the central reason for their excellent cyclability and lack of the so-called memory effect upon cycling.

However, advancements in cell capacity have been slow. Even if the carbon anode and the lithium cobalt/nickel/manganese oxide were optimized to their theoretical maximum capacity, lithium-ion batteries would only improve by less than a factor of two compared to the state-of-the-art product(s) in the market as of this writing.  $\text{CoO}_2$ -based cathodes, in particular, are unlikely to reach their theoretical capacity, as removing more than 0.5 unit of Li from  $\text{LiCoO}_2$  may result in release of  $\text{O}_2$  gas by oxidizing the oxide anion, which can lead to fires and explosions. In short, further breakthroughs in electrical energy-storage devices are needed to implement electrical storage on the massive scale needed.

One way to do so is to change the chemistry of lithium-ion batteries. While intercalation electrodes, with no structural change, have the benefit of high reversibility, it also means that only a limited amount of charge (and therefore lithium) can be exchanged. In order to incorporate more lithium, alloying or phase conversion chemistry may provide the needed advancement. There are many compounds that react with lithium to form solid solutions or ordered phases with lithium that may be used as the anode, but many plausible compositions

are relatively unexplored in the battery field. They include, but are not limited to, silicon<sup>11,12</sup>, germanium<sup>13</sup>, and metal fluorides,<sup>14</sup>. However, in general they all suffer from cyclability issues stemming from phase changes, surface-electrolyte interface (SEI) formation, poor electrical conductivity, and/or volume expansion/contraction.

Finally, another way to radically change how batteries work is to use lithium metal (or another alkali earth metal like sodium) as the anode. Doing so would dramatically increase the anode capacity and may allow for different chemistry at the cathode, including lithium-sulfur<sup>15</sup> and lithium-air<sup>17</sup> batteries. However, issues such as sulfur dissolution<sup>18</sup> and poor reversibility<sup>17,19</sup> continue to be roadblocks towards realization of such technologies. In addition, dendrite formation<sup>20</sup> that shorts the batteries is a big barrier in achieving that goal. One way to prevent dendrite formation is to have a physical separator also act as the electrolyte—a solid electrolyte. Currently, there are several polymer electrolytes that can be used,<sup>20,21,22</sup> though dendrites can still penetrate through them. As such, electrolytes made of inorganic materials, such as oxides, have great appeal. In fact, the use of  $\beta''$ -alumina<sup>23</sup> has allowed the technology of a molten sodium-sulfur battery to be commercialized<sup>24</sup>. However, diffusion of metal ions through most solids is notoriously slow at room temperature, in the order of  $10^{-12}$  cm<sup>2</sup>/s or lower in many cases.

## ***1.2 Outline of the Dissertation***

A significant portion of these problems can be addressed with some combination of solid state chemistry and electrochemistry. As someone co-advised by a solid state chemist and an electrochemist, it is almost a gold mine of opportunities to attempt to advance the field of fuel cells and batteries. So, the majority of this thesis will focus on materials that can improve upon the issues raised above.

In Chapter 2, I will explore an alternative to the carbon catalyst support in fuel cells. The required properties for a better catalyst support materials include high conductivity, high

surface area, and high chemical and electrochemical stability. I will demonstrate that mixed transition metal nitrides consisting of titanium, tantalum and aluminum are possible candidates.

In Chapter 3, I will explore a series of thin-film oxide catalysts for the oxygen reduction reaction (ORR). Most non-noble metals are not stable under the acidic conditions of PEMFC, but in alkaline fuel cells (AFC), many are stable. So, with collaborators, I developed a method to perform electrochemical experiments on thin films deposited using vapor deposition processes on non-conductive substrates.

In Chapter 4, I will show my successful approach for the synthesis of a new mixed oxide in powder form and its electrochemical characterization. This chapter was inspired by one result shown in Chapter 3, which gave comparable results to platinum in the alkaline media. The highly active compound turned out to be a mixed oxide of ruthenium and manganese that was previously unknown in the literature.

In Chapter 5, I will explore the use of transition metal nitrides as anode electrodes in lithium-ion batteries. Most of them are thought to react with lithium to form lithium nitride and the elemental metal at low potentials vs. lithium. As long as such reactions are reversible, they would be a viable alternative to carbon anodes. However, little is known about their performance and mechanisms of reaction in batteries. Equipped with the knowledge of nitride synthesis from the fuel cell catalyst support work and blessed with collaborators who excel in battery performance testing and *operando* X-ray techniques for mechanistic studies, I explore the use of transition metal nitrides in lithium-ion batteries.

Chapter 6 explores an attempt at finding a new phase that conducts lithium or sodium ions at sufficiently high rate at room (or near room) temperature to serve as potential battery electrolytes. In this chapter I also explore the development of a method to test for ionic conductivity of thin pellets of oxides.

In Chapter 7, I will present concluding remarks and present an outlook for future research.

## REFERENCES

- (1) ESRL Global Monitoring Division - Global Greenhouse Gas Reference Network <http://www.esrl.noaa.gov/gmd/ccgg/trends/global.html> (accessed Apr 17, 2016).
- (2) Bard, A. J.; Fox, M. A. Artificial Photosynthesis: Solar Splitting of Water to Hydrogen and Oxygen. *Acc. Chem. Res.* **1995**, *28*, 141–145.
- (3) Marcinkoski, J.; Spendelow, J. S.; Wilson, A.; Papageorgopoulos, D. C. DOE Fuel Cell Technologies Office Record 15015: Fuel Cell System Cost - 2015 [https://www.hydrogen.energy.gov/pdfs/15015\\_fuel\\_cell\\_system\\_cost\\_2015.pdf](https://www.hydrogen.energy.gov/pdfs/15015_fuel_cell_system_cost_2015.pdf) (accessed Apr 17, 2016).
- (4) Improving IC Engine Efficiency <http://courses.washington.edu/me341/oct22v2.htm> (accessed Apr 17, 2016).
- (5) Wang, B. Recent development of non-platinum catalysts for oxygen reduction reaction. *J. Power Sources* **2005**, *152*, 1–15.
- (6) Ioroi, T.; Akita, T.; Asahi, M.; Yamazaki, S.; Siroma, Z.; Fujiwara, N.; Yasuda, K. Platinum–titanium alloy catalysts on a Magnéli-phase titanium oxide support for improved durability in Polymer Electrolyte Fuel Cells. *J. Power Sources* **2013**, *223*, 183–189.
- (7) Whittingham, M. S. Electrical Energy Storage and Intercalation Chemistry. *Science* **1976**, *192*, 1126–1127.
- (8) Goodenough, J. B. Rechargeable batteries: challenges old and new. *J. Solid State Electrochem.* **2012**, *16*, 2019–2029.
- (9) Croguennec, L.; Palacin, M. R. Recent Achievements on Inorganic Electrode Materials for Lithium-Ion Batteries. *J. Am. Chem. Soc.* **2015**, *137*, 3140–3156.
- (10) Melot, B. C.; Tarascon, J.-M. Design and Preparation of Materials for Advanced Electrochemical Storage. *Acc. Chem. Res.* **2013**, *46*, 1226–1238.
- (11) Bourderau, S.; Brousse, T.; Schleich, D. M. Amorphous silicon as a possible anode material for Li-ion batteries. *J. Power Sources* **1999**, *81–82*, 233–236.
- (12) Chan, C. K.; Peng, H.; Liu, G.; McIlwrath, K.; Zhang, X. F.; Huggins, R. A.; Cui, Y. High-performance lithium battery anodes using silicon nanowires. *Nat. Nanotechnol.* **2008**, *3*, 31–35.
- (13) Silberstein, K. E.; Lowe, M. A.; Richards, B.; Gao, J.; Hanrath, T.; Abruña, H. D. Operando X-ray Scattering and Spectroscopic Analysis of Germanium Nanowire Anodes in Lithium Ion Batteries. *Langmuir* **2015**, *31*, 2028–2035.
- (14) Amatucci, G. G.; Pereira, N. Fluoride based electrode materials for advanced energy storage devices. *J. Fluor. Chem.* **2007**, *128*, 243–262.
- (15) Werner, J. G.; Johnson, S. S.; Vijay, V.; Wiesner, U. Carbon–Sulfur Composites from Cylindrical and Gyroidal Mesoporous Carbons with Tunable Properties in Lithium–Sulfur Batteries. *Chem. Mater.* **2015**, *27*, 3349–3357.
- (16) Ji, X.; Lee, K. T.; Nazar, L. F. A highly ordered nanostructured carbon–sulphur cathode for lithium–sulphur batteries. *Nat. Mater.* **2009**, *8*, 500–506.
- (17) Christensen, J.; Albertus, P.; Sanchez-Carrera, R. S.; Lohmann, T.; Kozinsky, B.; Liedtke, R.; Ahmed, J.; Kojic, A. A Critical Review of Li/Air Batteries. *J. Electrochem. Soc.* **2012**, *159*, R1–R30.
- (18) Gao, J.; Lowe, M. A.; Kiya, Y.; Abruña, H. D. Effects of Liquid Electrolytes on the Charge–Discharge Performance of Rechargeable Lithium/Sulfur Batteries:

- Electrochemical and in-Situ X-ray Absorption Spectroscopic Studies. *J Phys Chem C* **2011**, *115*, 25132–25137.
- (19) Shao, Y.; Park, S.; Xiao, J.; Zhang, J.-G.; Wang, Y.; Liu, J. Electrocatalysts for Nonaqueous Lithium–Air Batteries: Status, Challenges, and Perspective. *ACS Catal.* **2012**, *2*, 844–857.
- (20) Baskakova, Y. V.; Yarmolenko, O. V.; Efimov, O. N. Polymer gel electrolytes for lithium batteries. *Russ. Chem. Rev.* **2012**, *81*, 367.
- (21) Crowther, O.; West, A. C. Effect of Electrolyte Composition on Lithium Dendrite Growth. *J. Electrochem. Soc.* **2008**, *155*, A806–A811.
- (22) Kezuka, K.; Hatazawa, T.; Nakajima, K. The status of Sony Li-ion polymer battery. *J. Power Sources* **2001**, *97–98*, 755–757.
- (23) Lu, X.; Xia, G.; Lemmon, J. P.; Yang, Z. Advanced materials for sodium-beta alumina batteries: Status, challenges and perspectives. *J. Power Sources* **2010**, *195*, 2431–2442.
- (24) Rokkasho village, Aomori, Japan | Case Studies | NAS  
[https://www.ngk.co.jp/nas/case\\_studies/rokkasho/](https://www.ngk.co.jp/nas/case_studies/rokkasho/) (accessed Apr 16, 2016).

## CHAPTER 2

### SYNTHESIS AND ELECTROCHEMICAL CHARACTERIZATION OF $Ti_xTa_yAl_zN_{1-\delta}O_\gamma$ FOR FUEL CELL CATALYST SUPPORTS

Ryo H. Wakabayashi, Héctor D. Abruña\*, Francis J. DiSalvo\*

Department of Chemistry, Cornell University, Ithaca, New York 14853-1301

*As of submission of the dissertation (June 2016), all but sections 2.4.4, 2.4.5.2, 2.4.6.2 and 2.6 are under review for publication in the Journal of Power Sources.*

#### **2.1 Abstract**

Quinary  $Ti_xTa_yAl_zN_{1-\delta}O_\gamma$  of various compositions have been prepared by a co-precipitation method followed by ammonolysis. The nitride samples were examined as potential catalyst supports in polymer electrolyte membrane fuel cells. The nitride products crystallized in the rock salt (NaCl) structure over a wide range of compositions. The addition of Ta and Al was highly beneficial towards improving the chemical and electrochemical stability of TiN, without a significant loss of electrical conductivity. Platinum particles were successfully deposited on the (oxy)nitride samples, and the composite samples at some compositions were found to be comparable to Pt/carbon in their stability and catalytic activity even without optimizing the Pt deposition and dispersion processes.

#### **2.2 Introduction**

Fuel cells represent an environmentally friendly alternative to the internal combustion engine in applications such as automotive propulsion, since in principle they can operate at very high energy efficiencies, and depending on how the fuel is generated, emit zero carbon at the source of use.<sup>1</sup> However, prior to widespread deployment, there are several materials-related challenges that still need to be addressed in order to improve their cost, performance and durability. Currently, proton-exchange membrane fuel cells (PEMFC) use high-surface area carbon black (Vulcan)<sup>2</sup> as the catalyst support, but carbon is not thermodynamically

stable under typical operating conditions. Its formal oxidation potential is only +0.207 V vs. RHE, significantly lower than the working potential of fuel cell cathodes,<sup>3</sup> although the overpotential for oxidation is high. In addition, the carbon support can be oxidized at the anode of a fuel cell under fuel starvation conditions.<sup>4</sup> Corrosion of the carbon support can result in detachment and coalescence/sintering of catalyst (Pt) particles,<sup>5</sup> lowering the efficiency and lifetime of the fuel cell stack.<sup>3</sup>

Potential alternative catalyst support materials must have high electrical conductivity, chemical and electrochemical durability, high surface area, and binding affinity towards the catalyst nanoparticles.<sup>6</sup> Alternate candidates include carbides,<sup>7,8</sup> nitrides,<sup>9,10,11</sup> and oxides.<sup>12,13</sup> Of these, metal nitrides are especially promising, as many metal transition nitrides are metallic conductors, highly durable, and can be synthesized as high-surface area nanoparticles. Titanium nitride, for example, has been used as a coating material on bipolar plates of fuel cells by General Motors.<sup>14</sup>

Metal nitrides such as those of nickel,<sup>15</sup> molybdenum<sup>16,17,18</sup>, niobium,<sup>19</sup> iron<sup>20</sup> and chromium<sup>21</sup> have previously been reported as viable materials in electrochemical systems such as fuel cells. Of these, titanium nitride (TiN) is a particularly interesting and attractive candidate, since it is a metallic conductor ( $1.3 \times 10^4$  S/cm<sup>22</sup>) and is known for its mechanical durability. TiN has previously been examined as a possible alternative fuel cell catalyst support material<sup>23</sup>. In addition, titanium nitride is one of the hardest materials known (9 Mohs).<sup>24</sup> Although oxidation of nitrides to the corresponding oxides is thermodynamically favorable,<sup>25</sup> the kinetics of the reaction are very slow, sometimes resulting in the formation of only a thin surface oxide/oxy-nitride layer a few nanometers thick.<sup>26</sup> Pure TiN, however, is known to passivate (build up a thicker, insulating oxide layer) easily under acidic conditions.<sup>27</sup> In order to mitigate this tendency, several binary and ternary nitrides have been previously explored.<sup>19</sup>

Tantalum and aluminum nitrides<sup>10,28</sup> have been used as dopants in titanium nitride and other nitrides to enhance corrosion resistance. Tantalum nitride (as well as titanium nitride) is used as a diffusion barrier in semiconductor devices,<sup>29</sup> pointing to its durability. Aluminum doping of TiN has been shown to improve the oxidation resistance of TiN at higher temperatures<sup>30</sup>. Thin-film studies of (Ti,Al)N<sup>28,31,32,33</sup> have been reported, and studies of thin-films of (Ti,Ta)N<sup>34,35,36</sup> and (Ti,Ta,Al)N<sup>37,38,39</sup> have been published, in which increased oxidation resistance was generally observed.

We have previously investigated the physical<sup>40</sup> and electrochemical<sup>41</sup> properties of co-sputtered (Ti,Ta,Al)N thin films over a wide composition range, and found that (Ti,Ta,Al)N crystallizes in the rock-salt structure over a broad range of compositions. In addition, even a small amount of titanium nitride introduces considerable electrical conductivity, but the optimum conductivity and durability under electrochemical conditions was obtained at relatively high titanium content (approx. 70 %). However, while thin films are useful for screening and identifying new materials, they are not presently used as catalyst supports in fuel cells due to the expense of deposition methods, the low surface area, and poor scalability. In addition, thin films and powder particles do not always show the same corrosion behavior, and to our knowledge, no powder synthesis or characterization of (Ti,Ta,Al)N (or oxynitride) has been reported. To this end, we report here on the co-precipitation synthesis of mesoporous oxynitride particles and the comparative characterization of a range of compositions.

Various synthetic methods have been reported to form powders of transition metal nitrides. They include reaction of metal alkoxides with anhydrous hydrazine<sup>42</sup>, ligand exchange of TiCl<sub>4</sub> with NH<sub>3</sub>,<sup>43</sup> and direct nitridation of Ti powder in a nitrogen or ammonia atmosphere at high temperature. We have chosen to use the ammonolysis method with flowing ammonia, starting with oxide precursors derived from co-precipitation. This method is facile, versatile, produces high surface area particles, and is very tunable as has been shown in

the literature<sup>44,45,46,47</sup>. However, with this method no full conversion of the oxide to the nitride is possible, that is to say, some oxygen remains in the nitrides even after reaching equilibrium, or at least steady-state under the reaction conditions.

### 2.3 Experimental

#### 2.3.1 Synthesis of rock-salt $Ti_xTa_yAl_zN_{1-\delta}O_y$ ( $x+y+z = 1$ )

Ti(OBu)<sub>4</sub> (Aldrich 97%), Ta(OEt)<sub>5</sub> (Alfa Aesar 99.95%), Al(NO<sub>3</sub>)<sub>3</sub>·9H<sub>2</sub>O (Sigma-Aldrich, ACS reagent), Zn(NO<sub>3</sub>)<sub>2</sub>·6H<sub>2</sub>O (Sigma-Aldrich, ACS reagent), ethanol (200 proof, KOPTEC), and NH<sub>4</sub>OH (EMD) were used as received. In a typical synthesis procedure, a stoichiometric amount (0.003 mol total Ti + Ta + Al precursors) of Al(NO<sub>3</sub>)<sub>3</sub>·9H<sub>2</sub>O and excess Zn(NO<sub>3</sub>)<sub>2</sub>·6H<sub>2</sub>O were placed in a three-neck round-bottom flask. Addition of zinc ions to increase macroporosity is a method that we have previously reported for synthesis of nitrides from bulk, crystalline oxides.<sup>48,49</sup> The flask was then evacuated to 60 mtorr or lower on a Schlenk line. Metal nitrates are known to at least partially dehydrate under low pressure<sup>50</sup>. After backfilling the flask with Ar, 20 mL of ethanol were added into the flask using a syringe, followed by the addition of stoichiometric amounts of the remaining metal alkoxide reagents, and stirred for several minutes. The solution was then transferred, using the cannula transfer technique, into approximately 30 mL of 1.5 M NH<sub>4</sub>OH under rapid stirring, which resulted in the instantaneous formation of a white gel. The gel was then centrifuged to remove excess solvent and zinc ions, and was heated to 100°C to form a dry gel, followed by calcination at 450°C to form an amorphous mixed oxide precursor.

This precursor was subsequently ball-milled using a Fritsch Pulverisette 7 planetary mill to ensure that all particles were well below 1 micron in size. The mixed oxide was then heated under NH<sub>3</sub> (Airgas, anhydrous) flow (approx. 6 L/h) at 800 °C for up to 24 hours, yielding fine black powders. Zn has a very high vapor pressure under the reaction conditions, and therefore sublimates away when heated at high temperature, as described in our previous

work.<sup>48,49,51</sup> Some samples were heated up to 950 °C in order to obtain particles that exhibit sharper XRD peaks for better fits in lattice parameter refinements.

### 2.3.2 *Synthesis/Deposition of Pt nanoparticles*

In order to deposit platinum, the polyol method<sup>52</sup> was employed. Briefly, the nitride sample and appropriate amount of H<sub>2</sub>PtCl<sub>6</sub>·6H<sub>2</sub>O (Sigma-Aldrich) to deposit 20 wt. % Pt on the nitride were dissolved in 50 mL of ethylene glycol (Malinckrodt AR), and heated at 125-150 °C overnight. The product was then vacuum filtered, washed repeatedly with copious amount of water, and dried in air at 80°C overnight.

### 2.3.3 *Physical Characterization*

All samples, including precursors at various stages of synthesis, were characterized via powder X-ray diffraction using a Rigaku Ultima IV with Cu-K $\alpha$  radiation ( $\lambda=1.5406$  Å and 1.5444 Å for K $\alpha_1$  and K $\alpha_2$  respectively). Rietveld refinements were obtained using PDXL (Rigaku). Scanning electron microscopy (SEM) and energy-dispersive X-ray spectroscopy (EDX) were performed using a LEO-1550 field emission SEM. Nitrogen and oxygen contents were measured using a LECO ONH836 N/O/H analyzer (by LECO Corporation, St. Joseph, Michigan). Silicon nitride (NIST 8983) was used as the standard, and samples were dried for 1 hour at 105 °C. Nitrogen adsorption/desorption isotherms were measured and surface areas were calculated using the Brunauner-Emmett-Teller theory at 77 K using a Micrometrics ASAP 2020. All samples were degassed at 150 °C for 24h on a vacuum line prior to isotherm measurements. Conductivities of the powder samples, compressed at 200 PSI, were measured using a home-built four-point probe system we described in a previous report.<sup>53</sup>

### 2.3.4 *Stability Testing*

To explore a variety of fuel cell corrosion conditions, we studied the reactivity of the (oxy)nitride products (without Pt) in acidic environments. Approximately 10 mg of the products were immersed in approximately 2 mL of 0.1M H<sub>2</sub>SO<sub>4</sub> (Alfa Aesar, 99.9999%) or

0.1 M NaOH (Malinckrodt AR) in small glass vials, which were covered by Parafilm (Benis). The vials were immersed for 21 days in an oil bath kept at 60 °C. A photograph of the samples in vials was taken approximately every two days to monitor any visual changes, and solutions were replenished whenever the solution level decreased noticeably. After testing, the samples were washed repeatedly with de-ionized (DI) water and dried in air before taking XRD and SEM data.

### *2.3.5 Electrochemical Characterization*

Glassy carbon (5 mm diameter) electrodes were polished using 1  $\mu\text{m}$  diamond polishing paste (Buehler) followed by 0.3 and 0.05  $\mu\text{m}$  alumina powder (Extec and Buehler), and were rinsed using Millipore water (18 M $\Omega$ /cm Thermo Scientific Barnstead Nanopore). These electrodes were then sonicated in 0.1 M NaOH (Malinckrodt AR) for 5 minutes to activate the surface prior to deposition of the sample inks.

Inks were prepared by weighing out the appropriate amounts of sample (typically 3.9 mg) and ultrasonating (Microson Ultrasonic Cell Disruptor XL) in 1 mL of 0.02 wt. % Nafion (Sigma 5 wt. % in ethanol, diluted with 200 proof ethanol from KOPTEC) for at least 15 minutes. Within half an hour after sonication, 5  $\mu\text{L}$  of the specific ink were deposited onto a glassy carbon electrode. Inks were prepared such that Pt-containing samples would result in 20  $\mu\text{g}/\text{cm}^2$  of Pt loading on the electrode. For CVs of the nitride samples without Pt deposited on them, 7.8 mg of samples were used to make inks, and deposited on the electrodes.

Cyclic voltammetry was performed in 0.1 M H<sub>2</sub>SO<sub>4</sub> (Alfa Aesar, 99.9999%) or 0.1 M NaOH (Malinckrodt AR) at room temperature. A platinum wire was used as the counter electrode and a home-made reversible hydrogen electrode (RHE) was used as the reference electrode. Samples without platinum were scanned at 50 mV/s and samples with platinum were scanned at 20 mV/s, using a Bioanalytical Systems CV-27 potentiostat. The oxygen reduction reaction on Pt/nitride samples was studied at room temperature using rotating disk

electrode (RDE) voltammetry at 20 mV/s. The solution was saturated with O<sub>2</sub> (Airgas, Ultra High Pressure) by bubbling for 15 minutes initially and for 7 minutes after every scan to ensure that the solution remained saturated with oxygen for each scan.

## 2.4 Results and Discussions

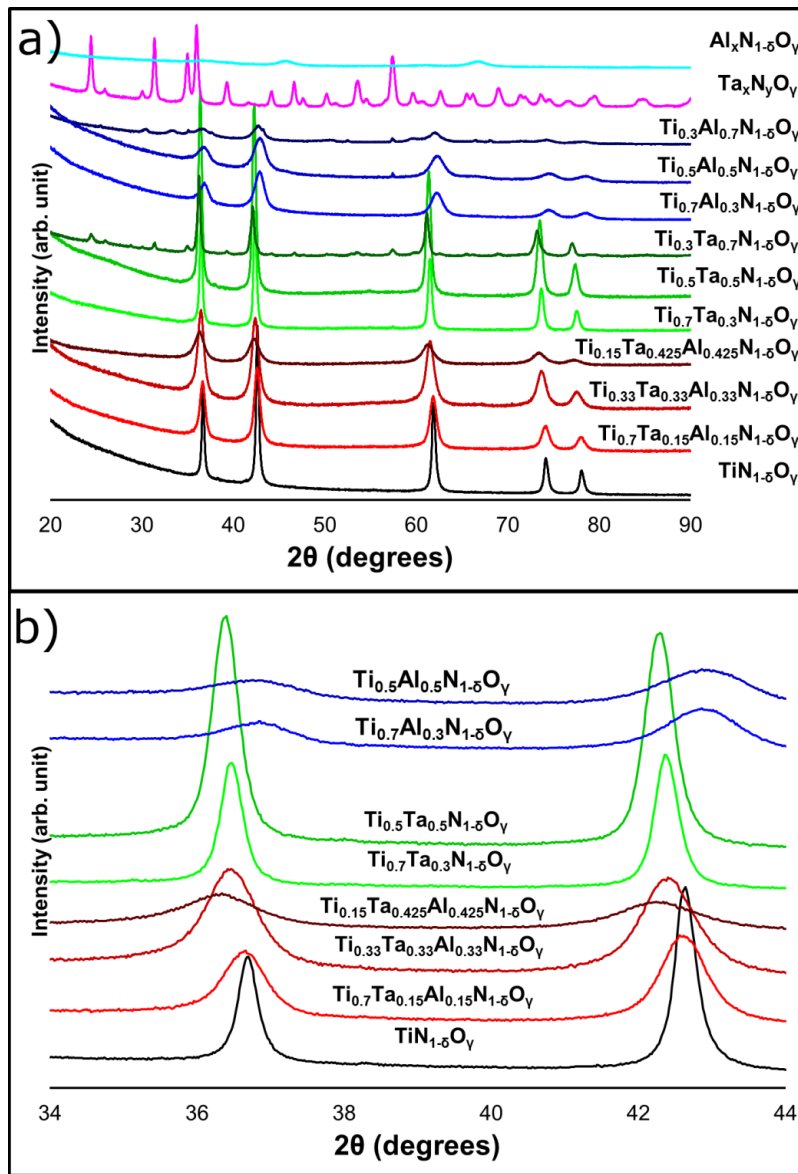
### 2.4.1 Structure and Compositions

Figure 2.1 shows pXRD patterns of Ti<sub>x</sub>Ta<sub>y</sub>Al<sub>z</sub>N<sub>1-δ</sub>O<sub>γ</sub> of various compositions ( $0.15 \leq x \leq 1$ ), formed by heating the mixed oxides of the desired metal stoichiometry under ammonia at 950 °C. The nitrides crystallize in the rock salt (*Fd-3m*) structure over a wide range of compositions with no visible impurity phases for medium to high Ti content ( $0.15 \leq x$  if  $y = z$  and  $0.5 \leq x$  if  $y$  or  $z = 0$ ). At low Ti content (Ti<sub>0.3</sub>Ta<sub>0.7</sub>N<sub>1-δ</sub>O<sub>γ</sub> and Ti<sub>0.3</sub>Al<sub>0.7</sub>N<sub>1-δ</sub>O<sub>γ</sub>), crystalline Ta<sub>3</sub>N<sub>5</sub> and Al<sub>2</sub>O<sub>3</sub> impurities were observed, respectively. We reported similar behavior results in a previous study of thin films deposited via co-sputtering in Ar/N<sub>2</sub>.<sup>40</sup>

In the specific case of TiN<sub>1-δ</sub>O<sub>γ</sub>, the lattice constant was found to be  $a = 4.239 \text{ \AA}$ . This is in general agreement with other reported syntheses of titanium nitride using similar synthetic methods ( $4.22\text{-}4.23 \text{ \AA}$ <sup>54</sup>,  $4.242 \text{ \AA}$ <sup>55</sup>,  $4.218 \text{ \AA}$ <sup>51</sup>). The observed lattice constant is also slightly smaller than the value of  $4.242 \text{ \AA}$  reported in the ICDD (00-038-1420). The reported lattice parameter of bulk TiN (ICDD 00-038-1420) was made on a pristine single crystalline sample prepared by the high temperature nitridation of elemental titanium, and therefore had very low levels of oxygen impurities. Therefore the lattice constant of the TiN<sub>1-δ</sub>O<sub>γ</sub> sample reported in this paper suggests the presence of oxygen on nitrogen sites, since O<sup>2-</sup> = 126 pm and N<sup>3-</sup> = 132 pm.<sup>56,57</sup>

When precipitated Ta<sub>2</sub>O<sub>5</sub> and Al<sub>2</sub>O<sub>3</sub> are heated under ammonia under identical conditions, orthorhombic, deep red Ta<sub>3</sub>N<sub>5</sub> and an amorphous, slightly-gray powder (Figure 2.1) were observed, respectively. Apparently, when TiN is present at a sufficiently high concentration, it catalyzes the crystallization of a cubic (rock salt) products of Ta and Al

nitrides.



**Figure 2.1.** pXRD patterns of  $Ti_xTa_yAl_zN_{1.5}O_y$  (a) synthesized at 950 °C. (b) shows a zoomed region containing the first two peaks.

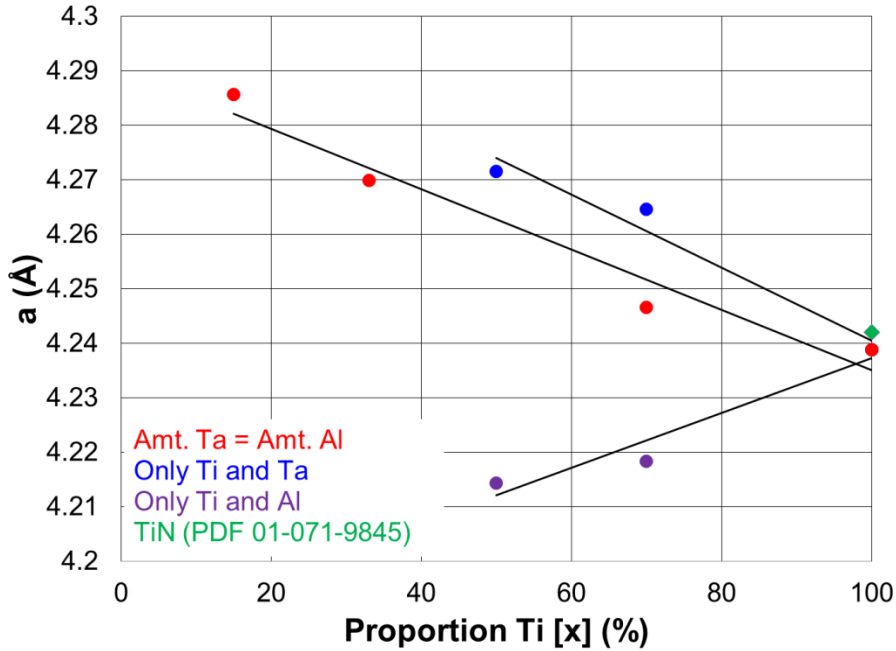


**Figure 2.2.** Lattice constant as a function of  $x$  in  $\text{Ti}_x\text{Ta}_y\text{Al}_z\text{N}_{1-\delta}\text{O}_\gamma$  synthesized at  $950^\circ\text{C}$ . Red dots:  $y=z$  ( $\text{Ta} = \text{Al}$ ); purple dots:  $y = 0$  (only Ti or Ta); green dot: literature value of TiN.

The lattice constants of  $\text{Ti}_x\text{Ta}_y\text{Al}_z\text{N}_{1-\delta}\text{O}_\gamma$  follow Vegard's law (see Figure 2.2). Addition of an element with a larger atomic radius than Ti ( $\text{Ti}^{3+} = 81 \text{ pm}$ ,  $\text{Ta}^{3+} = 86 \text{ pm}$ , though  $\text{Ta}^{5+} = 78 \text{ pm}^{56,57}$ ) increases the lattice constants slightly, while addition of an element with a smaller atomic radius than titanium ( $\text{Al}^{3+} = 67.5 \text{ pm}^{56,57}$ ) decreases the lattice constant. When equal amounts of both tantalum and aluminum ( $y = z$ ) were added, only a slight increase in the lattice parameter was observed as the composition changed. The X-ray peak intensity ratios between (111) and (200) near  $36.8^\circ$  and  $42.6^\circ$  change from 0.62:1 for  $\text{TiN}_{1-\delta}\text{O}_\gamma$  (literature value for pure TiN: 0.75:1) to 1.01:1 in the case of  $\text{Ti}_{0.33}\text{Ta}_{0.33}\text{Al}_{0.33}\text{N}_{1-\delta}\text{O}_\gamma$ , which is an effect that has been previously observed.<sup>10</sup> These results are similar to those reported in a recent study of sputtered thin film nitrides published by our collaborators.<sup>40</sup> The X-ray data suggest that the sample compositions are homogeneous, at least at the nanometer scale. A

slight offset from the literature value of the lattice constant of TiN suggests that there are oxygen impurities in the synthesized samples (oxygen ion is smaller than nitrogen ion<sup>56,57</sup>). Samples synthesized at lower temperature (800°C) showed smaller lattice constants (by 0.015 Å) when compared to those synthesized at 950°C (Figure 2.3).

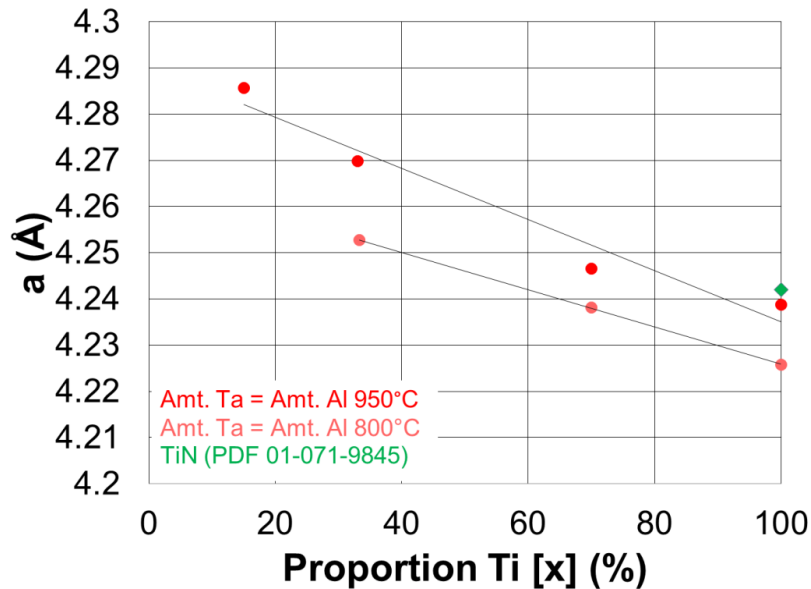


**Figure 2.3.** Lattice constants as a function of x in  $Ti_xTa_yAl_zN_{1-\delta}O$  where  $y=z$ . Red dots were samples heated under ammonia at 950 °C, pink at 800 °C.

Figure 2.4 shows EDX data of nitride samples (heated at 800 °C) at different starting/nominal metal compositions. N and O are not reported here, as the small difference in their energies (0.392 and 0.595 keV for N and O, respectively<sup>58</sup>) makes them very difficult to distinguish by EDX. The ratio of the three metals is within the expected measurement error of the nominal ratio, further suggesting a uniform mixture of the metal ions in the nitride samples. As expected, no Zn was observed, as expected, since it sublimed out of the product under reducing conditions at elevated temperature (see Experimental section for details).

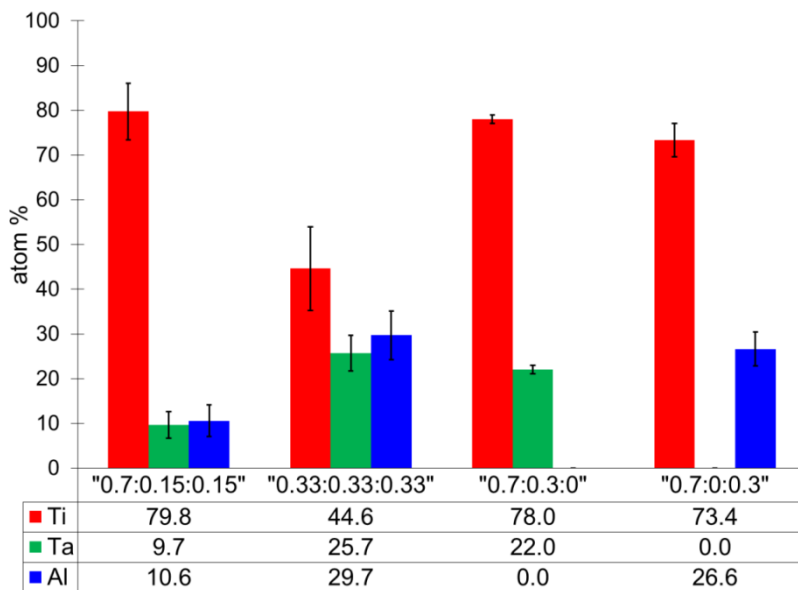


**Figure 2.4.** EDX results of atomic composition (atom %) of the  $Ti_xTa_yAl_zN_{1.5}O_\gamma$  samples (nominal ratios in quotation marks) synthesized at 800 °C. Error bars are one standard deviation calculated from ten measurements.

Table 2.1 gives the nitrogen and oxygen content of the samples (all heated at 800 °C), measured using a LECO ONH836 N/O/H thermal analyzer. For  $TiN_{1.5}O_\gamma$ , the ratio of N to O was 3.4:1. A low level of H (H:O of about 8%) was also detected. The hydrogen content may arise from a small amount of adsorbed water, or –OH termination on the surface from air exposure of the product. The nitrogen-to-oxygen ratio was comparable to those seen in titanium nitride samples prepared using similar synthetic methods (N:O = 3.4:1 to 2.6:1 in Dong et al.,<sup>45</sup> for example). The composition of  $TiN_{1.5}O_\gamma$  sample can be calculated from these data, assuming a rock salt structure, as  $Ti_{0.82}\square_{0.18}N_{0.67}O_{0.33}$  ( $\square$  indicates vacancies). From these data, the average oxidation state of Ti was determined to be  $Ti^{+3.38}$  (consideration of the low H content does not significantly alter the average oxidation state). In all cases, number of mol of cations was less than number of mol of anions. This also indicates that there must be cation vacancies (since the only crystalline phase has the rock salt structure and anion interstitials are

highly unlikely due to the large size of the anion). In short, these (oxy)nitride samples are much more complicated than generally recognized.

x:y:z in $Ti_xTa_yAl_zN_{1-\delta}O_\gamma$	mol N	mol O	mol H	mol $\square_{\text{cation}}$	Avg. ox. state of Ti, if all Ta = +3	Avg. ox. state of Ti, if all Ta = +5
1:0:0	0.772	0.228	0.020	0.18	3.38	3.38
0.7:0.15:0.15	0.672	0.328	0.027	0.19	3.41	2.99
0.33:0.33:0.33	0.402	0.598	0.036	0.37	5.37	3.37
0.7:0.3:0	0.777	0.223	0.034	0.24	3.91	3.05
0.7:0:0.3	0.573	0.427	0.038	0.20	3.33	3.33

**Table 2.1.** N/O/H amounts and corresponding proposed chemical formulas of the  $Ti_xTa_yAl_zN_{1-\delta}O_\gamma$  samples synthesized at 800 °C. Mol of every ions is normalized so sum of anions add up to 1.

The samples with low amounts of aluminum ( $z \leq 0.3$ ) had a nitrogen-to-oxygen ratio of approximately 3:1 and metal-to-anion ratio of about 0.6 to 0.8:1. Again, this indicates that, at 800 °C, the ammonolysis process leaves some oxygen behind. Therefore the oxidation states of some of the metal cations are likely to be different from +3, the expected value in a pure rock-salt (defect-free) metal nitride. If one assumes that all tantalum cations have an oxidation state of +3, the average oxidation state of titanium was found to be approximately 3.4-3.9, and if Ta ions are assumed to be +5, the average oxidation state of Ti is nearly exactly +3. The average Ta oxidation state likely lies somewhere in between, but it is very likely that a non-negligible proportion of Ta is +5, which agrees with the ammonolysis result of pure tantalum oxide ( $Ta_3N_5$ , see Figure 2.1). The samples that contain 30% aluminum had significantly higher oxygen content, which is not surprising given that aluminum nitride cannot be formed from pure aluminum oxide using the synthetic method employed in this work, even at higher temperatures.

## 2.4.2 Conductivity Measurements

x:y:z in $Ti_xTa_yAl_zN_{1-\delta}O_\gamma$	Conductivity (S/cm) at 200 PSI
1:0:0	$9.7*10^{-2}$
0.7:0.15:0.15	$6.0*10^{-2}$
0.33:0.33:0.33	$2.1*10^{-3}$
0.7:0.3:0	$2.0*10^{-2}$
0.7:0:0.3	$3.7*10^{-2}$
Vulcan C XC72	$1.7*10^0$

**Table 2.2.** Powder conductivity of  $Ti_xTa_yAl_zN_{1-\delta}O_\gamma$  samples synthesized at 800 °C measured using home-built powder conductivity measurement device.

A home-made four-point probe was used to estimate the conductivity of compressed powders at 200 PSI (Table 2.2). The conductivity values were somewhat lower than previously reported values for titanium nitride powders ( $0.2 - 0.4 \text{ S/cm}^{55}$ ), likely due to inter-particle resistance from poor packing of the grains inside the apparatus. Conductivities controlled by the packing of powders have been reported in previous work.<sup>59</sup> Whisker-like TiN particles showed conductivity on the order of  $10^5 \text{ S/cm}$ , similar to the conductivity of bulk TiN ( $1.3*10^4 \text{ S/cm}^{22}$ ), but our packed powder samples showed four orders of magnitude lower conductivity at room temperature. We therefore expect that a significant fraction of the resistance in our samples come from the contact resistance between the powder grains. Since tight particle-to-particle packing is not a necessity in fuel cells (as long as particles can make contact with the gas diffusion layer), this is not likely to be a problem in an operating fuel cell. Such behavior is not surprising because very hard materials will not deform at low pressure, resulting in poor packing and contact between particles. This contrasts with carbon black (Vulcan XC-72R), which is soft and deformable. Our electrochemical data (Figures 2.9 and 2.22, discussed later *vide infra*) suggest that inter-particle and electrode-particle contacts are sufficiently high for fuel cell applications.

Addition of tantalum and/or aluminum to TiN decreased its conductivity. Both Ta<sub>3</sub>N<sub>5</sub> and AlN are wide band-gap semiconductors (2.1 eV and 6.2eV, respectively<sup>60,61</sup>), and since both Ta and Al are more oxophilic, most of the oxygens are likely coordinated to Ta and/or Al, and oxides of both are insulators. The samples with 70% Ti (by nominal composition), however, still have comparable conductivity to the samples without any Ta and/or Al.

#### 2.4.3 Surface Area

x:y:z in Ti <sub>x</sub> Ta <sub>y</sub> Al <sub>z</sub> N <sub>1.5</sub> O <sub>γ</sub>	SA (m <sup>2</sup> /g)	Sample std. dev. (m <sup>2</sup> /g)
1:0:0	33.6	10.0
0.7:0.15:0.15	51.27	4.33
0.33:0.33:0.33	56.10	5.26
Vulcan XC72	232.1	N/A

**Table 2.3.** Surface area and standard deviation of the Ti<sub>x</sub>Ta<sub>y</sub>Al<sub>z</sub>N<sub>1.5</sub>O<sub>γ</sub> synthesized at 800 °C.

The surface areas of the samples were determined by applying the Brunauer-Emmett-Teller method to the nitrogen adsorption measurements (Table 2.3). All samples had surface areas around 50 m<sup>2</sup>/g which is comparable to, or higher than, other nitride nanoparticles previously reported.<sup>19,45,53,62</sup> The surface area per gram was lower than that of carbon black due largely to the difference in density of the materials (density of titanium nitride: 5.4 g/cm<sup>3</sup>; graphite: 2.7g/cm<sup>3</sup>). The microcopy images (Figure 2.5) and the electrochemical behavior (Figures 2.9 and 2.22) suggest that the porosity is sufficiently high for the purpose of fuel cell applications.

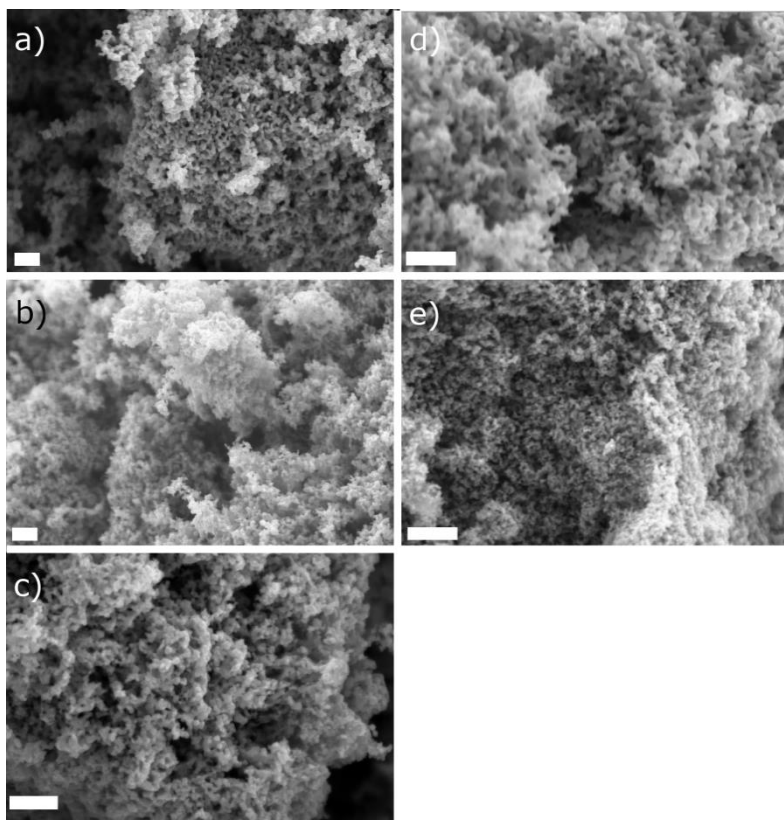


**Figure 2.5.** SEM images of  $\text{Ti}_x\text{Ta}_y\text{Al}_z\text{N}_{1-\delta}\text{O}_\gamma$  synthesized at 800 °C where  $x:y:z =$  (a) 1:0:0, (b) 0.7:0.15:0.15, (c) 0.33:0.33:0.33, (d) 0.7:0.3:0 and (e) 0.7:0:0.3. Scale bars are 200 nm.

#### 2.4.4 Additional Discussion on Effects of Zn

Figure 2.6 shows the PXRD patterns of  $\text{Ti}_{0.33}\text{Ta}_{0.33}\text{Al}_{0.33}\text{O}_x$ , with various amount of zinc (ratio is shown as  $\text{Zn}/(\text{Ti}+\text{Ta}+\text{Al})$ ). Beyond 200% Zn to rest of the metals, the onset of formation of ZnO peaks can be seen, and at 600% ZnO peaks are very clearly present. This is not a surprising result, as the most Zn-rich phase of zinc titanate is  $\text{Zn}_2\text{TiO}_4$  (“2”). The author chose to include excess zinc (“6”) in all samples that were further tested, in order to maximize porosity.

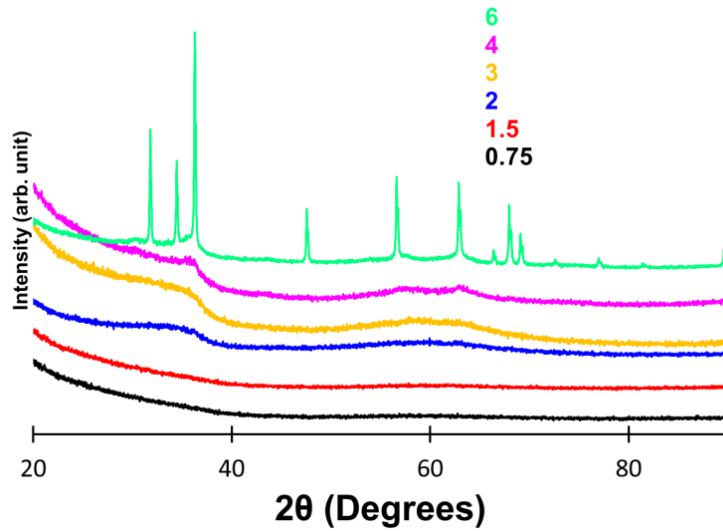


**Figure 2.6.** pXRD patterns of  $\text{Ti}_{0.33}\text{Ta}_{0.33}\text{Al}_{0.33}\text{O}_x$ , with various amount of zinc oxide.

Numbers are molar ratios of Zn: (Ti+Ta+Al).

Figure 2.7 shows SEM image of  $\text{Ti}_x\text{Ta}_y\text{Al}_z\text{N}_{1.6}\text{O}_7$ , with and without zinc in the precursor. Particle sizes are significantly bigger than the domain size calculated using XRD ( $\sim 20$  nm), indicating significant sintering and agglomeration of crystallites, but the samples still maintain porosity, and therefore high surface area. Visually, samples that were made by solid-solid separation of zinc cations appear to have significantly more macroporosity than ones without zinc. However, nitrogen absorption data suggests that all samples have similarly high surface areas, within error bar (Figure 2.8).

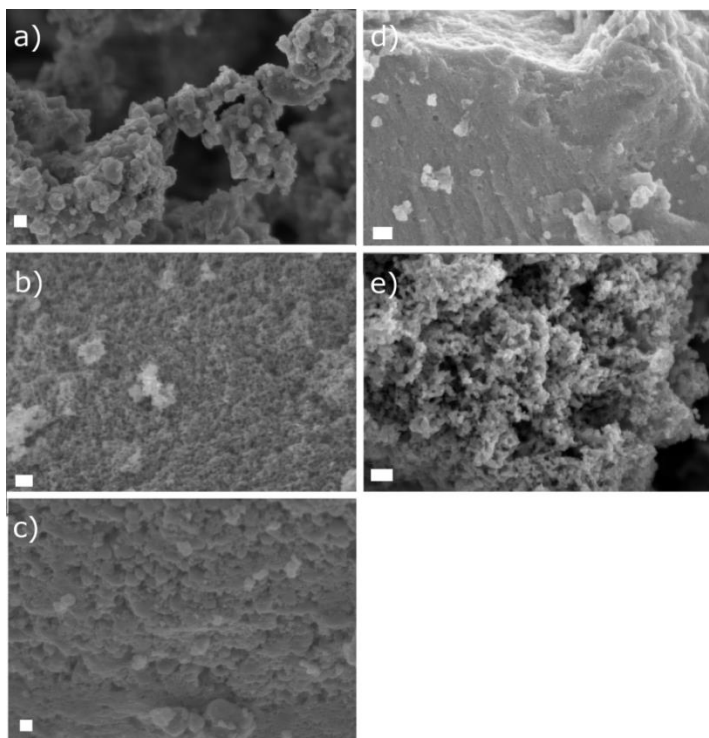


**Figure 2.7.** SEM images of  $\text{Ti}_{0.33}\text{Ta}_{0.33}\text{Al}_{0.33}\text{N}_{1.6}\text{O}_\gamma$ , with varying amount of zinc ions in oxide precursor: a) no Zn b) Zn: (Ti+Ta+Al) = 1:1, c) 2:1, d) 4:1 and e) 6:1. Scale bars are

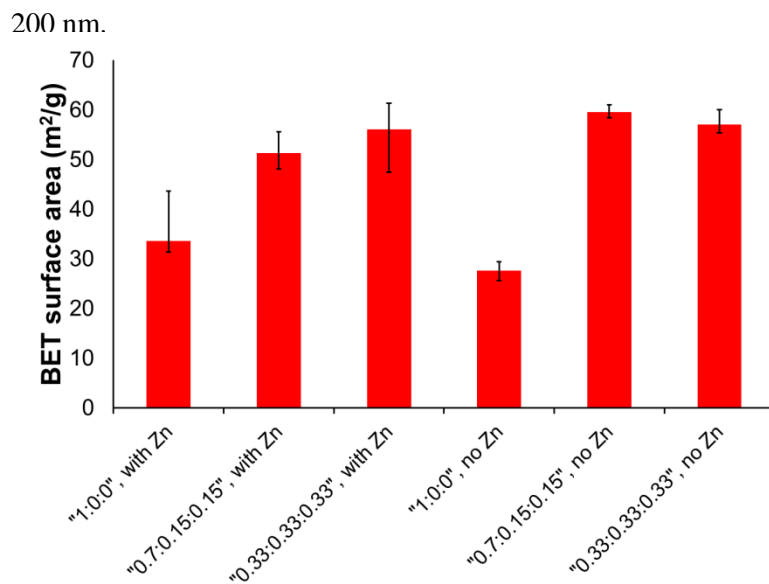


**Figure 2.8.** BET surface area of samples made with Zn precursors (“with Zn”) and without Zn. “with Zn” data are replication of Table 2.3. Error bars are sample standard deviation.

## 2.4.5 Electrochemical Behavior

### 2.4.5.1 Acidic Media

Cyclic voltammograms (CV) in 0.1 M H<sub>2</sub>SO<sub>4</sub> can be used to understand passivation and/or corrosion behavior of materials under fuel cell-like conditions. We have chosen to modify the accelerated durability test recommended by the Department of Energy/United States Council for Automobile Research<sup>63</sup> by cycling over a wider potential range (0.05 to 1.1 V vs. RHE) as we believe that cycling over such a potential range better simulates both fuel starvation and the highly oxidizing conditions at the cathode. Changes in CVs over time can be used as a proxy to assess the stability of samples under operating conditions. In Figure 2.9, it can be clearly seen that the addition of Ta significantly increased the stability of the TiN-based compounds. While TiN<sub>1-δ</sub>O<sub>γ</sub> and Ti<sub>0.7</sub>Al<sub>0.3</sub>N<sub>1-δ</sub>O<sub>γ</sub> show substantial changes in their CVs, likely due to surface oxidation of the particles to insulating oxides, the samples containing Ta showed a far smaller decrease in current. While somewhat speculative on our part, we believe that the secondary elements form a thin, stable oxide layer on the surface of the nitrides, somewhat analogous to a thin layer of chromium oxide on stainless steel.

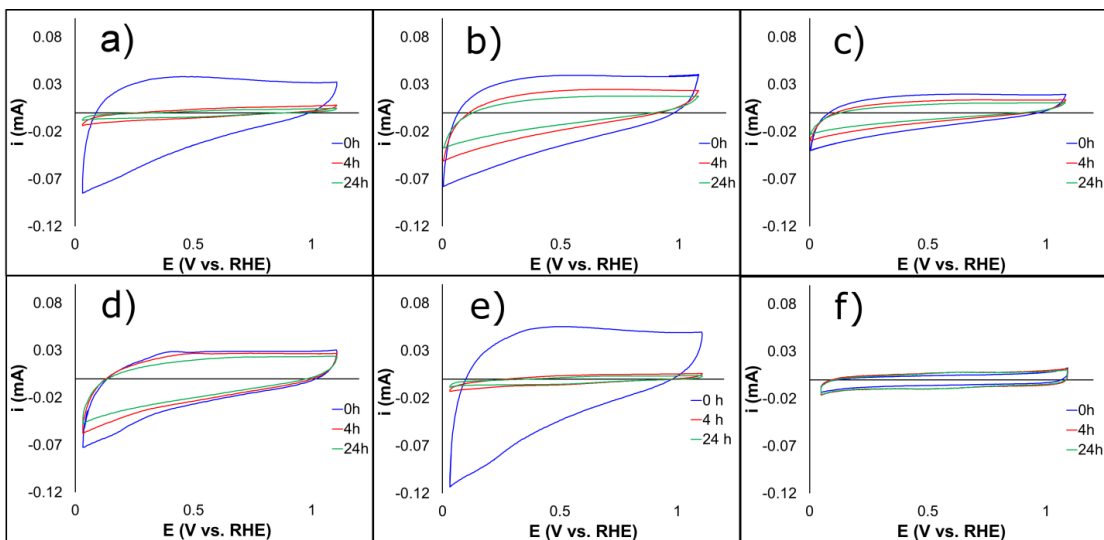


**Figure 2.9.** Cyclic voltammograms of  $\text{Ti}_x\text{Ta}_y\text{Al}_z\text{N}_{1-\delta}\text{O}_\gamma$  synthesized at 800 °C where  $x:y:z =$  (a) 1:0:0, (b) 0.7:0.15:0.15, (c) 0.33:0.33:0.33, (d) 0.7:0.3:0 and (e) 0.7:0:0.3 in 0.1M  $\text{H}_2\text{SO}_4$ , scanned continuously for 24 h at 50 mV/s. Shown CVs are taken at 0 h (blue), 4 h (red) and 24 h (green) after the start of the experiment. (f) is Vulcan XC-72 as a comparison.

#### 2.4.5.2 Alkaline Media

Cyclic voltammetry was also performed in 0.1M NaOH. Unlike the case in sulfuric acid, addition of secondary elements makes the nitrides more prone to change in cyclic voltammograms (Figure 2.10), indicating passivation and/or corrosion. This is a curious result, as none of the constituents should be less stable under alkaline conditions. It may be an ink recipe optimization issue, as Nafion is a proton conductor and not therefore not optimal as a hydroxide conductor, and that may be reflected as a generally lower current, and in the case of  $\text{Ti}_{0.33}\text{Ta}_{0.33}\text{Al}_{0.33}\text{N}_{1-\delta}\text{O}_\gamma$ , a significant slant indicating resistance in the system. However, omission of Nafion seems to have made adhesion worse (see Figure 2.11), in that the CVs actually showed even more change. I ascribe that to particles falling off due to the fact that there is nothing acting as a binder. Further development of the ink preparation and formulation are necessary.

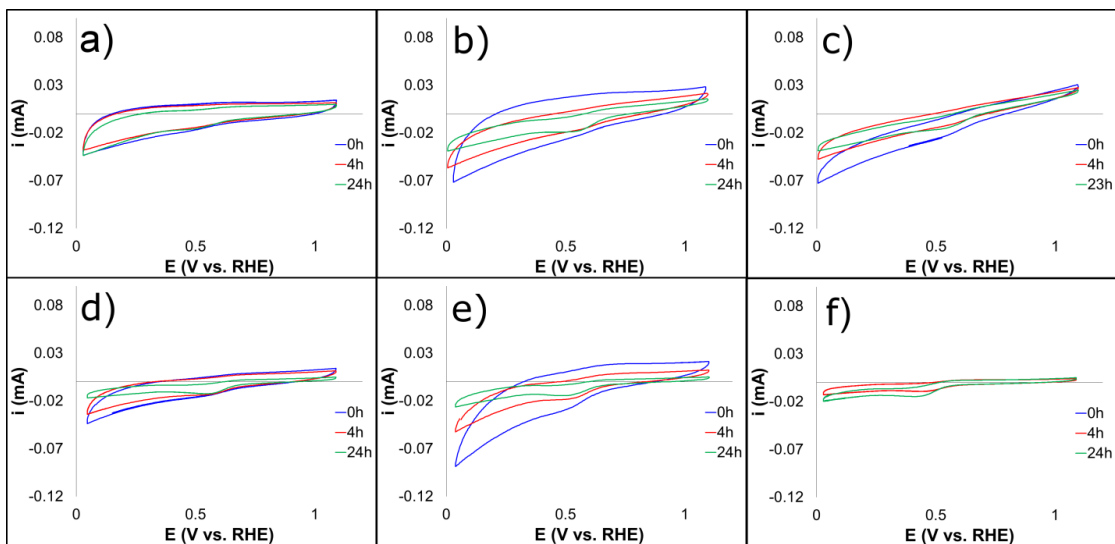


**Figure 2.10.** Cyclic voltammograms of  $Ti_xTa_yAl_zN_{1-\delta}O_\gamma$  where  $x:y:z =$  (a) 1:0:0, (b) 0.7:0.15:0.15, (c) 0.33:0.33:0.33, (d) 0.7:0.3:0 and (e) 0.7:0:0.3 in 0.1M NaOH, scanned continuously for 24 h at 50 mV/s. Shown CVs are taken at 0 h (blue), 4 h (red) and 24 h (green) after start of the experiment. (f) is the glassy carbon substrate.

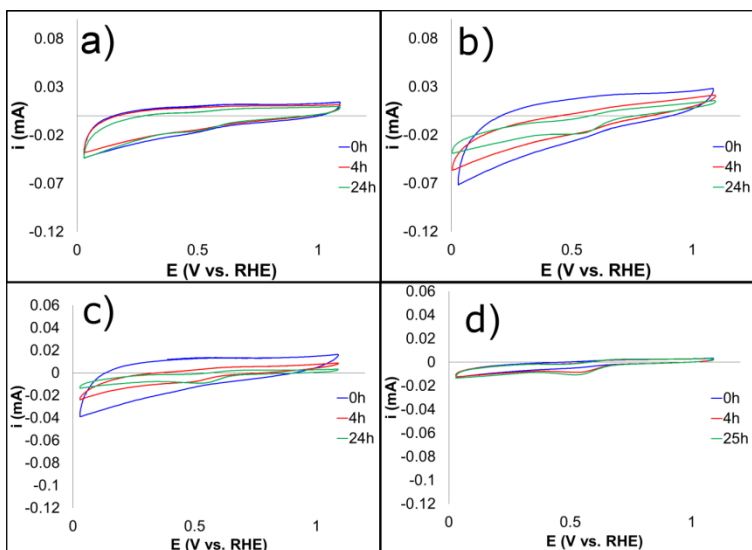


**Figure 2.11** Cyclic voltammograms of  $Ti_xTa_yAl_zN_{1-\delta}O_\gamma$  where  $x:y:z =$  (a) 1:0:0, (b) 0.7:0.15:0.15, (c) 1:0:0, ink made without Nafion (binder) and (d) 0.7:0.15:0.15, ink made without Nafion in 0.1M NaOH, scanned continuously for 24 h at 50 mV/s. Shown CVs are taken at 0 h (blue), 4 h (red) and 24 h (green) after start of the experiment.

## 2.4.6 Chemical Stability

### 2.4.6.1 Acidic Media

Long-term chemical stability tests were performed by submerging small amounts (approximately 10 mg) of nitride samples in 0.1M H<sub>2</sub>SO<sub>4</sub> which was kept at 60 °C in an oil bath for 3 weeks. Figure 2.12 (inset) shows a photograph of the particles after 21 days, in which oxidation of some samples is clearly evident from the white color of the samples. pXRD patterns (Figure 2.12) confirmed this visual evidence, as patterns of all white or gray samples did not have any peaks corresponding to the rock salt TiN structure, but instead showed the presence of TiO<sub>2</sub> (rutile) phase. The differences in overall intensities are ascribed to from variations in quantities of samples recovered. EDX data and SEM images (Figures 2.13 and 2.14) further confirm the results. All samples, except Ti<sub>0.7</sub>Ta<sub>0.3</sub>N<sub>1.6</sub>O<sub>γ</sub>, showed significant change in morphology after testing. In all of the samples, the amount of aluminum in the retrieved product was shown to have dropped considerably, likely due to dissolution as suggested by the Pourbaix diagram of aluminum<sup>64</sup>. The ratio of Ti:Ta also changed in all samples except Ti<sub>0.7</sub>Ta<sub>0.3</sub>N<sub>1.6</sub>O<sub>γ</sub> (within the error bar, however), possibly indicating a partial loss of titanium into the solution in some cases. The corroded TiN<sub>1.6</sub>O<sub>γ</sub> and Ti<sub>0.7</sub>Al<sub>0.3</sub>N<sub>1.6</sub>O<sub>γ</sub> exhibited identical needle-like morphologies and had some sulfur content (by EDX), perhaps indicating the formation of titanium oxysulfate (due to the presence of sulfate anions). The EDX software detected Si in two samples, but this effect likely arises from interference with the Ta signal (Si K<sub>α</sub> = 1.74 keV, Ta M<sub>α</sub> = 1.71 keV<sup>58</sup>). The small Ta signal in Ti<sub>0.7</sub>Al<sub>0.3</sub>N<sub>1.6</sub>O<sub>γ</sub> is very likely a contamination from other samples or Si from the glass vial used in the stability test.

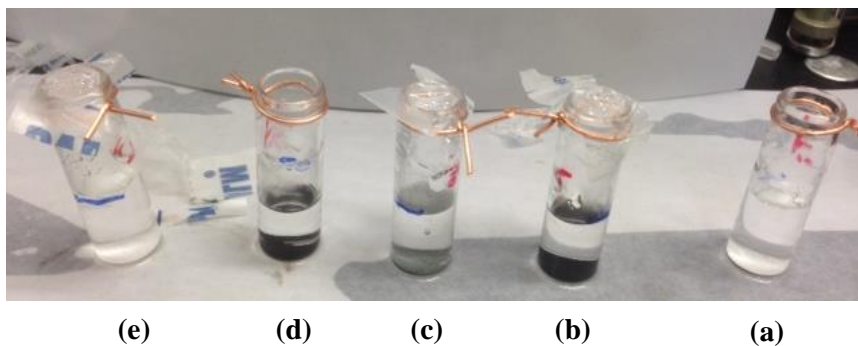
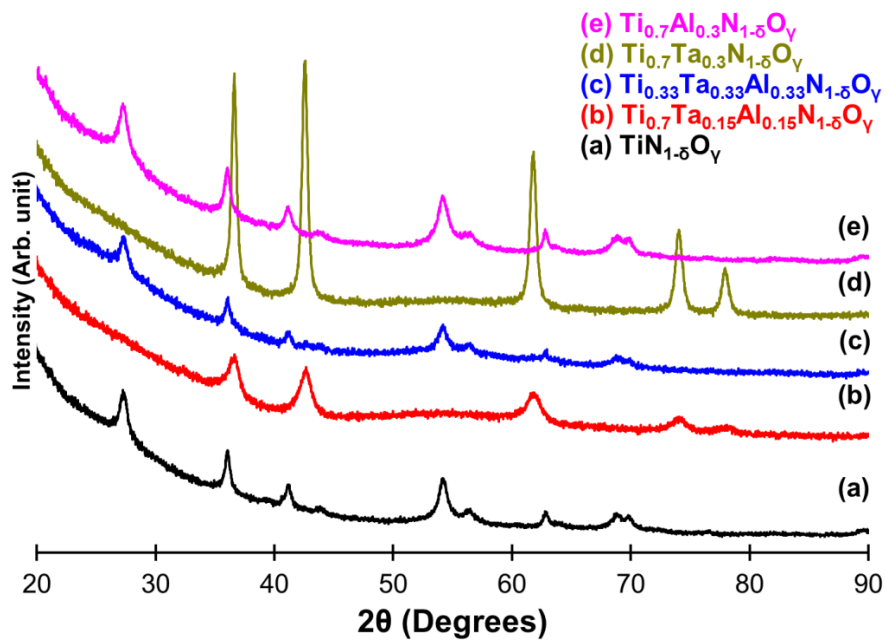


**Figure 2.12.** pXRD patterns and photographs (bottom) of  $\text{Ti}_x\text{Ta}_y\text{Al}_z\text{N}_{1-\delta}\text{O}_\gamma$  samples synthesized at 800 °C after 21 days of stability testing in 0.1M  $\text{H}_2\text{SO}_4$  at 60°C. In the photograph, the particles in vials (a) and (e) are white.

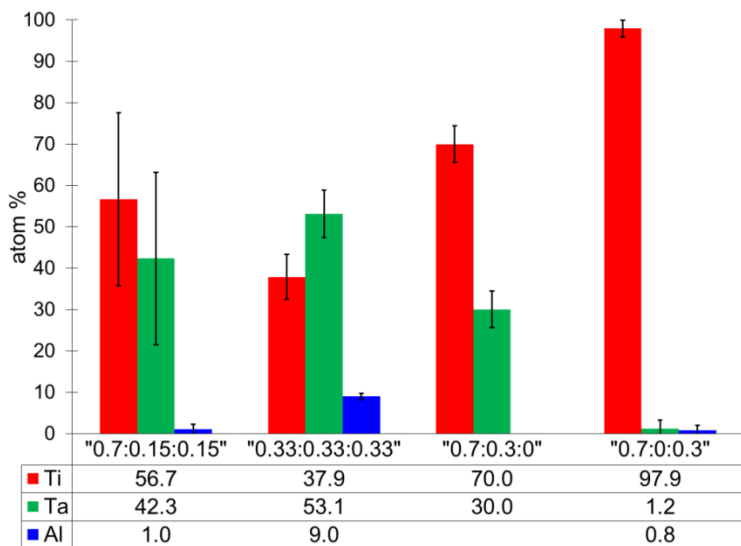


**Figure 2.13.** EDX results of  $Ti_xTa_yAl_zN_{1.6}O_\gamma$  samples (nominal ratio in quotation marks; synthesized at 800 °C) after 21 days of stability testing in 0.1M  $H_2SO_4$  at 60°C. Error bars are one standard deviation calculated from ten measurements.

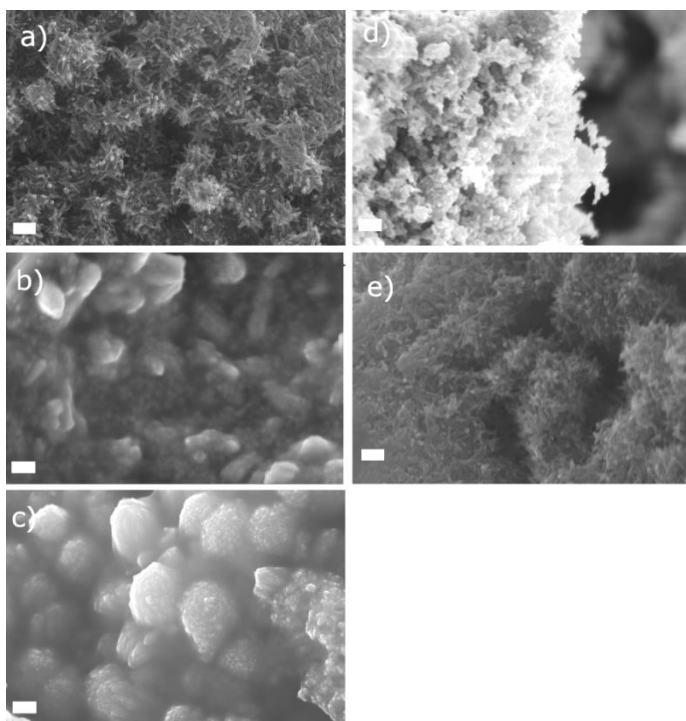


**Figure 2.14.** SEM images of  $Ti_xTa_yAl_zN_{1.6}O_\gamma$  synthesized at 800 °C where  $x:y:z =$  (a) 1:0:0, (b) 0.7:0.15:0.15, (c) 0.33:0.33:0.33, (d) 0.7:0.3:0 and (e) 0.7:0:0.3 after 21 days of stability test in 0.1M  $H_2SO_4$  at 60°C. Scale bars are 200 nm.

#### 2.4.6.2 Alkaline Media

Chemical stability tests were also performed in 0.1M NaOH, kept at 60 °C in an oil bath for 3 weeks. Figure 2.15 (top) shows a photograph of all particles after 21 days. The nitrides showed better stability under alkaline conditions than they did under acidic condition. Only  $\text{Ti}_{0.7}\text{Al}_{0.33}\text{N}_{1.6}\text{O}_\gamma$  turned completely white. XRD (Figure 2.15, bottom; the difference in intensities are largely due to amount of sample recovered after the stability test) shows a broad oxidation peak at around  $45^\circ$ , indicating formation of the anatase  $\text{TiO}_2$  phase. The same peak can be seen for  $\text{TiN}_{1.6}\text{O}_\gamma$  as well, but curiously enough, no other peaks corresponding to  $\text{TiO}_2$  were observed. SEM images (Figure 2.16) show surface degradation of  $\text{TiN}_{1.6}\text{O}_\gamma$  as well as  $\text{Ti}_{0.7}\text{Al}_{0.3}\text{N}_{1.6}\text{O}_\gamma$ , while other samples, especially  $\text{Ti}_{0.7}\text{Ta}_{0.15}\text{Al}_{0.15}\text{N}_{1.6}\text{O}_\gamma$ , keep their porous morphologies even after 21 days. However, in all but one sample ( $\text{Ti}_{0.7}\text{Ta}_{0.3}\text{N}_{1.6}\text{O}_\gamma$ ), no significant change in ratios of Ti:Ta:Al was observed (Figure 2.17). This indicates that the presence of tantalum stabilized aluminum ions in the lattice, instead of dissolving into the acidic solution as it is suggested on the Pourbaix Diagram of aluminum.<sup>64</sup>

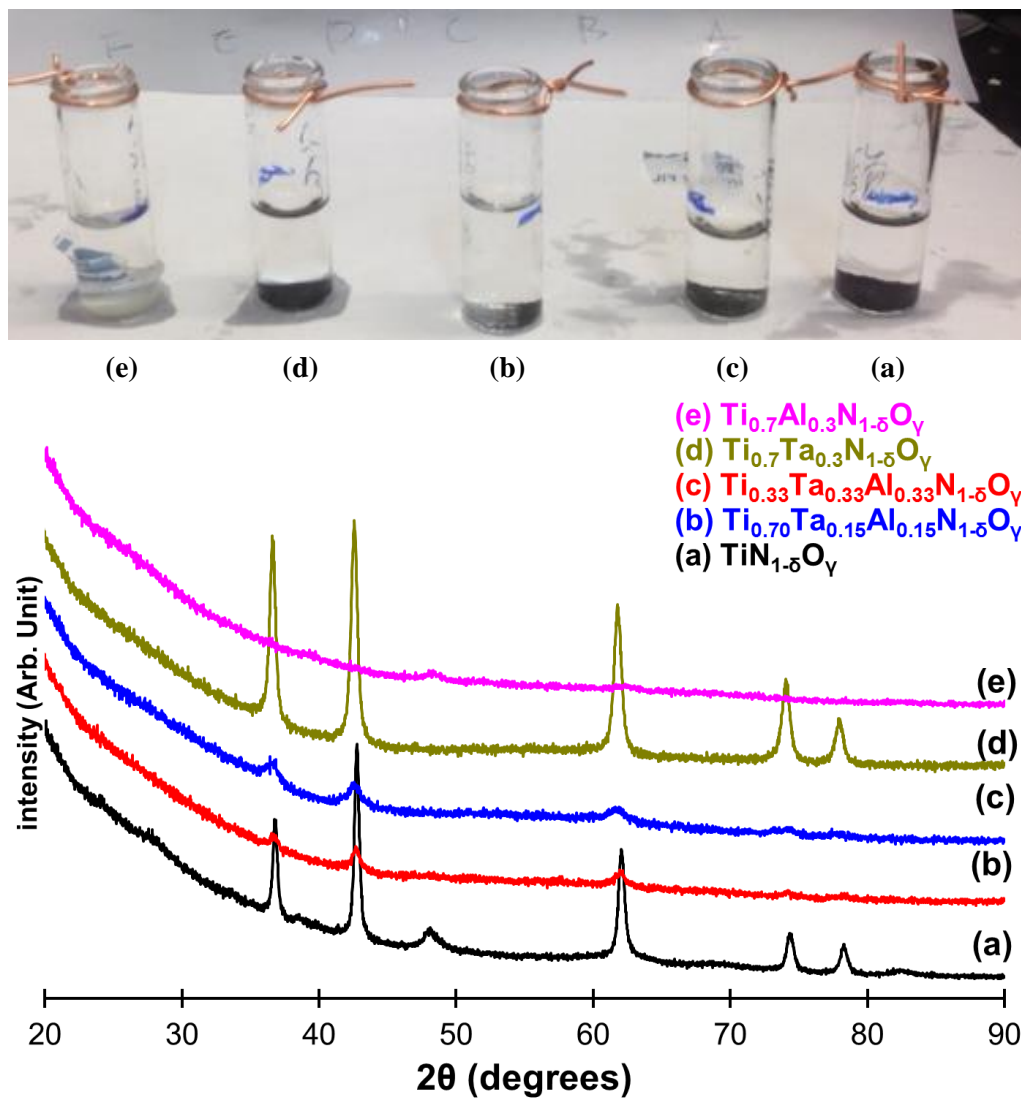


**Figure 2.15.** pXRD patterns and photographs (inset) of  $\text{Ti}_x\text{Ta}_y\text{Al}_z\text{N}_{1.5}\text{O}_\gamma$  samples after 21 days of stability test in 0.1M NaOH at 60 °C.

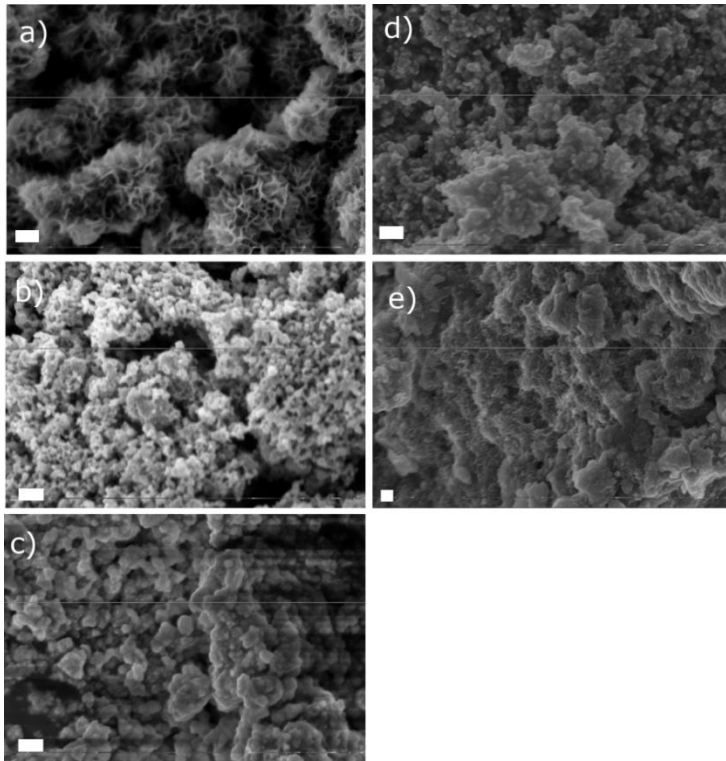


**Figure 2.16.** SEM images of  $Ti_xTa_yAl_zN_{1.6}O_\gamma$  synthesized at 800 °C where  $x:y:z =$  (a) 1:0:0, (b) 0.7:0.15:0.15, (c) 0.33:0.33:0.33, (d) 0.7:0.3:0 and (e) 0.7:0:0.3 after 21 days of stability test in 0.1M NaOH at 60°C. Scale bars are 200 nm.

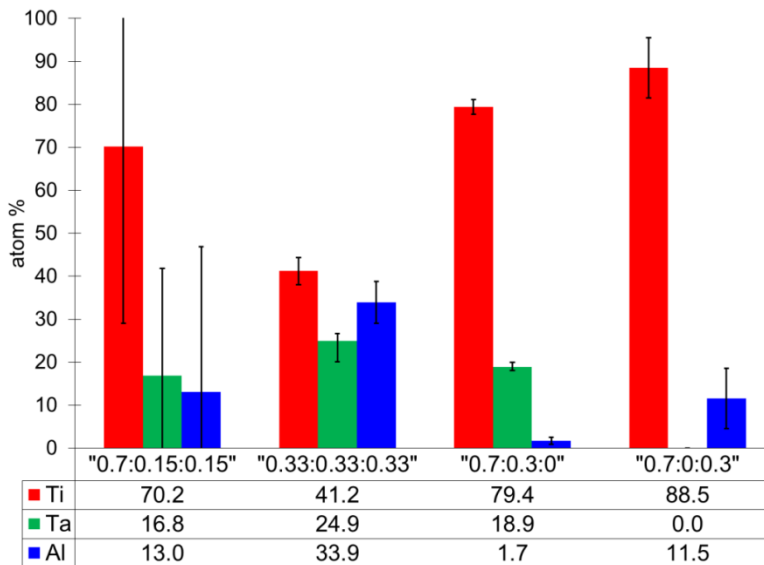


**Figure 2.17.** EDX results of  $Ti_xTa_yAl_zN_{1.6}O_\gamma$  samples (nominal ratio in quotation marks; synthesized at 800 °C) after 21 days of stability testing in 0.1M NaOH at 60°C. Error bars are one standard deviation, calculated from ten measurements.

#### 2.4.7 Pt Deposition and Electrochemistry Using Pt/ $Ti_xTa_yAl_zN_{1-\delta}O_\gamma$

Figure 2.18 shows the pXRD patterns of Pt deposited on representative  $Ti_xTa_yAl_zN_{1-\delta}O_\gamma$  samples. They show clear fcc Pt peaks and rock-salt TiN structure peaks, with Pt domain sizes of approx. 5 nm from both the refinement and the Scherrer equation, using the full width at half max (FWHM) of the Pt (200) peak (Scherrer constant = 0.94). Figure 2.19 shows the SEM images of nitride samples with deposited Pt nanoparticles, and Figure 2.20 shows bright-field TEM images of those samples. The particles appear uniform in both size and distribution, indicating that the deposition method was successful. In some of the TEM images, however, it appears that Pt particles did not disperse uniformly on some of the nitride particles. Optimization of Pt deposition and dispersion would be appropriate for further studies. Because of poor image contrast of some of the nitride particles (not very thin, higher Z than carbon), automated particle size analysis was not possible. As a consequence, there is a manual sampling error in the Pt particle size analyses, but the average and standard distribution of the particle sizes are consistent with the XRD domain size (Table 2.4).

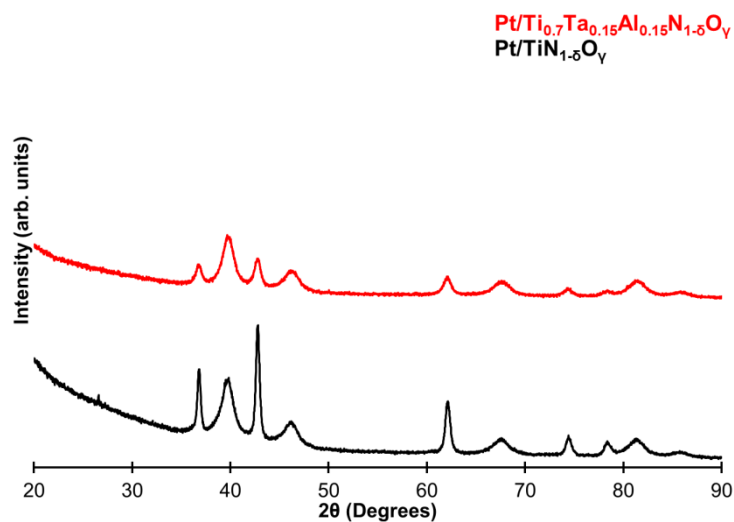


**Figure 2.18.** pXRD patterns of Pt/ $Ti_xTa_yAl_zN_{1-\delta}O_\gamma$ .

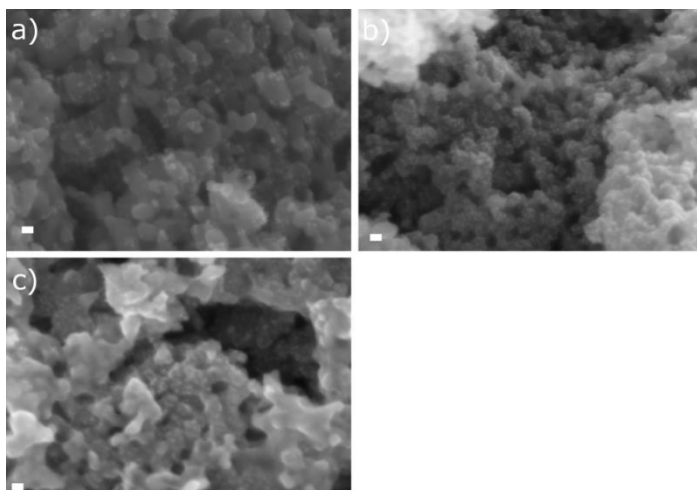
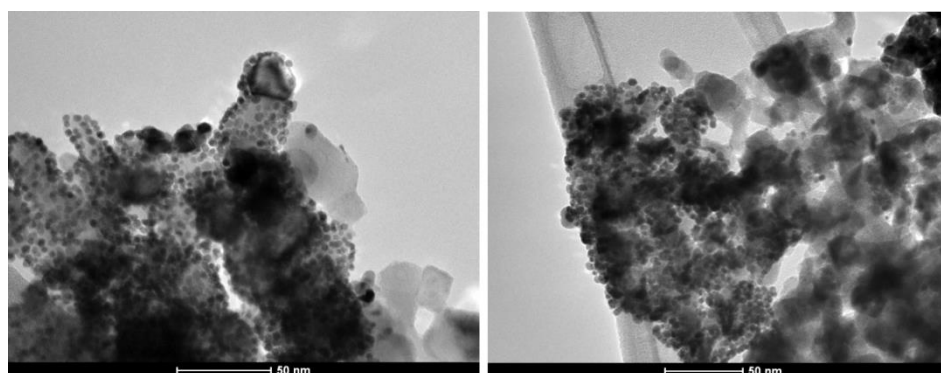


**Figure 2.19.** SEM images of Pt/Ti<sub>x</sub>Ta<sub>y</sub>Al<sub>z</sub>N<sub>1-δ</sub>O<sub>γ</sub> synthesized at 800 °C where x:y:z = (a) 1:0:0, (b) 0.7:0.15:0.15, (c) 0.7:0.3:0. Scale bars are 20 nm.



x:y:z in Ti <sub>x</sub> Ta <sub>y</sub> Al <sub>z</sub> N <sub>1-δ</sub> O <sub>γ</sub>	Average (nm)	Sample standard dev. (nm)
1:0:0	7.72	0.228
0.7:0.15:0.15	6.72	0.328

**Table 2.4.** Particle size analysis (average and standard distribution) of Pt particles on Ti<sub>x</sub>Ta<sub>y</sub>Al<sub>z</sub>N<sub>1-δ</sub>O<sub>γ</sub> from analyses of at least 100 particles.

The oxygen reduction reaction (ORR) was studied by depositing 20 wt. % Pt on the nitride supports. We chose this as a model reaction to test the behavior at high potentials applied to the cathode, since this condition is one of the main causes for corrosion of carbon. It is therefore important to show that an alternative material does not hinder the ORR activity. We emphasize that absolutely no carbon black was added in the ink-making process, as the corrosion of carbon supports (discussed in the Introduction section) is a significant motivation for this work. Figure 2.21 shows stationary CVs in nitrogen-saturated 0.1M H<sub>2</sub>SO<sub>4</sub> and Figure 2.22 shows the RDE voltammograms of ORR in oxygen-saturated 0.1M H<sub>2</sub>SO<sub>4</sub>. For comparison, 20 wt. % Pt was deposited using the identical method on Vulcan XC 72, and tested under identical conditions. The CVs of Pt/nitrides (in the absence of rotation) show typical features of platinum CVs (hydrogen adsorption and desorption, Pt oxide formation and desorption), especially after repeated scans, indicating that Pt nanoparticles are sufficiently dispersed on the nitride supports and that there is good electrical contact between the Pt nanoparticles and the substrate/support. Over at least 24 hours, nitride/Pt samples and Pt/C showed negligible difference in ORR behavior (onset potential and E<sub>1/2</sub> within 20 mV, and at most 7 % decrease in limiting current). In fact, the ORR onset potential improved very slightly (5-10 mV) using nitrides instead of carbon as catalyst support. CVs (Figure 2.9) show no clear oxidative peak, so we anticipate that the long-term stability to be at least as good as carbon.

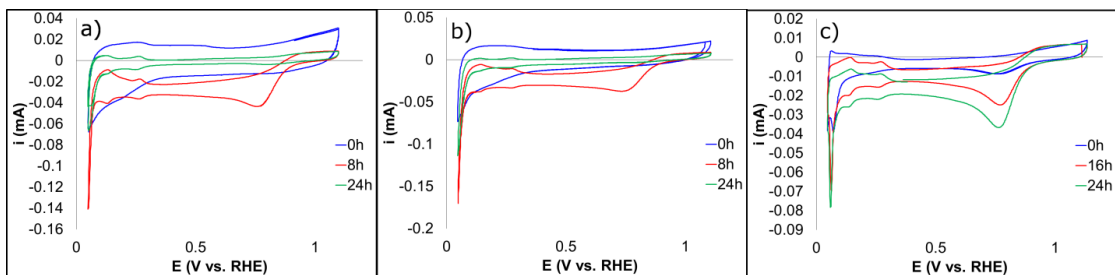


**Figure 2.21.** Stationary CVs of Pt/nitride samples of  $\text{Ti}_x\text{Ta}_y\text{Al}_z\text{N}_{1-\delta}\text{O}_\gamma$  where  $x:y:z =$  (a) 1:0:0, (b) 0.7:0.15:0.15, (c) Pt/C in 0.1M  $\text{H}_2\text{SO}_4$ , scanned continuously for 24 h at 20 mV/s. Shown CVs are taken at 0 h (blue), 8 h (red) and 24 h (green) after start of the experiment.

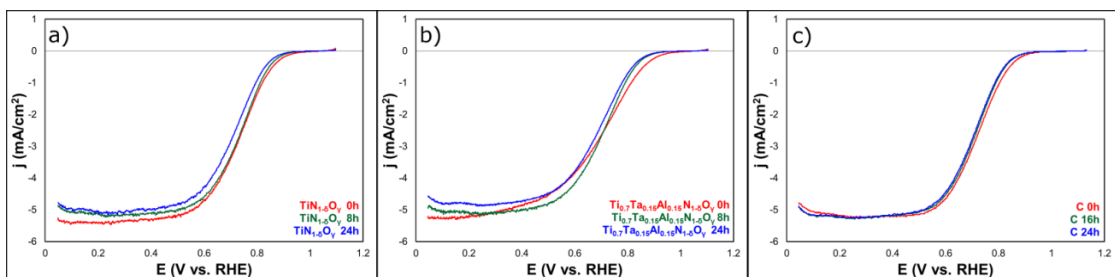


**Figure 2.22.** RDE voltammograms (1600 rpm) of representative samples of (a) Pt /  $\text{TiN}_{1-\delta}\text{O}_\gamma$  (20 wt. %) and (b) Pt /  $\text{Ti}_{0.7}\text{Ta}_{0.15}\text{Al}_{0.15}\text{N}_{1-\delta}\text{O}_\gamma$  (20 wt. %) synthesized at 800 °C in  $\text{O}_2$ -saturated 0.1M  $\text{H}_2\text{SO}_4$ , taken at the start of the experiment, 8 hours after the start, and 24 hours after the start of the experiment. (c) is Pt/C for comparison.

## 2.5 Conclusions

We have synthesized quinary  $\text{Ti}_x\text{Ta}_y\text{Al}_z\text{N}_{1-\delta}\text{O}_\gamma$  of various compositions by coprecipitation followed by ammonolysis in flowing ammonia. The synthetic method using metal nitrate salts and/or alkoxides is a versatile approach that can be applied to other oxide or nitride materials. We have shown that  $\text{Ti}_x\text{Ta}_y\text{Al}_z\text{N}_{1-\delta}\text{O}_\gamma$  samples crystallize in the TiN (rock-salt) structure with cationic vacancies introduced by addition of Ta and Al as well as presence of oxygen. These materials also have high surface areas, and are sufficiently conductive to act as support materials for fuel cell catalysts. Addition of Ta and Al, especially Ta, improves the

stability of titanium nitride under electrochemical conditions. Pt nanoparticles, immobilized on the nitride support, exhibited well-behaved ORR kinetics, indicating that there are no deleterious effects to the use of these nitrides as fuel cell catalyst supports.

## **2.6 Future Directions**

Optimization of the Pt deposition system, as well as ink formulation and processing procedures, would be highly desirable. Work discussed in 2.4.7 is definitely not well-optimized (unlike ink-making procedure for Pt/C, which is widespread in the literature).

## **2.7 Acknowledgments**

This work is based upon work supported as part of the Energy Materials Center at Cornell (EMC<sup>2</sup>), an Energy Frontier Research Center funded by the U.S. Department of Energy, Office of Science, and Office of Basic Energy Sciences under Award Number DE-SC0001086. This work was also supported by Cornell University from September 2014 through June 2016.

The authors would like to thank Mick Thomas for his assistance with the SEM measurements, LECO Corporation (St. Joseph, MI) for the N/O/H measurements, and Prof. Franck Tessier (University of Rennes 1) for assistance with the N/O analysis measurements. This work made use of the Cornell Center for Materials Research Shared Facilities which are supported through the NSF MRSEC program (DMR-1120296).

## REFERENCES

- (1) Aricò, A. S.; Bruce, P.; Scrosati, B.; Tarascon, J.-M.; Schalkwijk, W. van Nanostructured materials for advanced energy conversion and storage devices. *Nat. Mater.* **2005**, *4*, 366–377.
- (2) Shao-Horn, Y.; Sheng, W. C.; Chen, S.; Ferreira, P. J.; Holby, E. F.; Morgan, D. Instability of Supported Platinum Nanoparticles in Low-Temperature Fuel Cells. *Top. Catal.* **2007**, *46*, 285–305.
- (3) Ioroi, T.; Akita, T.; Asahi, M.; Yamazaki, S.; Siroma, Z.; Fujiwara, N.; Yasuda, K. Platinum–titanium alloy catalysts on a Magnéli-phase titanium oxide support for improved durability in Polymer Electrolyte Fuel Cells. *J. Power Sources* **2013**, *223*, 183–189.
- (4) Cameron, D. S. Fuel Cells Science and Technology 2008. *Platin. Met. Rev.* **2009**, *53*, 147–154.

- (5) Liu, Z. Y.; Zhang, J. L.; Yu, P. T.; Zhang, J. X.; Makharia, R.; More, K. L.; Stach, E. A. Transmission Electron Microscopy Observation of Corrosion Behaviors of Platinized Carbon Blacks under Thermal and Electrochemical Conditions. *J. Electrochem. Soc.* **2010**, *157*, B906–B913.
- (6) Joo, S. H.; Choi, S. J.; Oh, I.; Kwak, J.; Liu, Z.; Terasaki, O.; Ryoo, R. Ordered nanoporous arrays of carbon supporting high dispersions of platinum nanoparticles. *Nature* **2001**, *412*, 169–172.
- (7) Wan, C.; Leonard, B. M. Iron-Doped Molybdenum Carbide Catalyst with High Activity and Stability for the Hydrogen Evolution Reaction. *Chem. Mater.* **2015**, *27*, 4281–4288.
- (8) Kimmel, Y. C.; Xu, X.; Yu, W.; Yang, X.; Chen, J. G. Trends in Electrochemical Stability of Transition Metal Carbides and Their Potential Use As Supports for Low-Cost Electrocatalysts. *ACS Catal.* **2014**, *4*, 1558–1562.
- (9) Cao, B.; Veith, G. M.; Neuefeind, J. C.; Adzic, R. R.; Khalifah, P. G. Mixed Close-Packed Cobalt Molybdenum Nitrides as Non-noble Metal Electrocatalysts for the Hydrogen Evolution Reaction. *J. Am. Chem. Soc.* **2013**, *135*, 19186–19192.
- (10) Wang, L.; Northwood, D. O.; Nie, X.; Housden, J.; Spain, E.; Leyland, A.; Matthews, A. Corrosion properties and contact resistance of TiN, TiAlN and CrN coatings in simulated proton exchange membrane fuel cell environments. *J. Power Sources* **2010**, *195*, 3814–3821.
- (11) Cui, Z.; Yang, M.; DiSalvo, F. J. Mesoporous Ti<sub>0.5</sub>Cr<sub>0.5</sub>N Supported PdAg Nanoalloy as Highly Active and Stable Catalysts for the Electro-oxidation of Formic Acid and Methanol. *ACS Nano* **2014**, *8*, 6106–6113.
- (12) Subban, C. V.; Zhou, Q.; Hu, A.; Moylan, T. E.; Wagner, F. T.; DiSalvo, F. J. Sol–Gel Synthesis, Electrochemical Characterization, and Stability Testing of Ti<sub>0.7</sub>W<sub>0.3</sub>O<sub>2</sub> Nanoparticles for Catalyst Support Applications in Proton-Exchange Membrane Fuel Cells. *J Am Chem Soc* **2010**, *132*, 17531–17536.
- (13) Wang, D.; Subban, C. V.; Wang, H.; Rus, E.; DiSalvo, F. J.; Abruña, H. D. Highly Stable and CO-Tolerant Pt/Ti<sub>0.7</sub>W<sub>0.3</sub>O<sub>2</sub> Electrocatalyst for Proton-Exchange Membrane Fuel Cells. *J Am Chem Soc* **2010**, *132*, 10218–10220.
- (14) Li, Y.; Meng, W.-J.; Swathirajan, S.; Harris, S. J.; Doll, G. L. Corrosion resistant PEM fuel cell **2001**.
- (15) Xu, K.; Chen, P.; Li, X.; Tong, Y.; Ding, H.; Wu, X.; Chu, W.; Peng, Z.; Wu, C.; Xie, Y. Metallic Nickel Nitride Nanosheets Realizing Enhanced Electrochemical Water Oxidation. *J. Am. Chem. Soc.* **2015**.
- (16) Park, H.-C.; Lee, K.-H.; Lee, Y.-W.; Kim, S.-J.; Kim, D.-M.; Kim, M.-C.; Park, K.-W. Mesoporous molybdenum nitride nanobelts as an anode with improved electrochemical properties in lithium ion batteries. *J. Power Sources* **2014**, *269*, 534–541.
- (17) Zhang, K.; Zhang, L.; Chen, X.; He, X.; Wang, X.; Dong, S.; Han, P.; Zhang, C.; Wang, S.; Gu, L.; Cui, G. Mesoporous Cobalt Molybdenum Nitride: A Highly Active Bifunctional Electrocatalyst and Its Application in Lithium–O<sub>2</sub> Batteries. *J. Phys. Chem. C* **2013**, *117*, 858–865.
- (18) Ma, L.; Ting, L. R. L.; Molinari, V.; Giordano, C.; Yeo, B. S. Efficient hydrogen evolution reaction catalyzed by molybdenum carbide and molybdenum nitride nanocatalysts synthesized via the urea glass route. *J. Mater. Chem. A* **2015**.
- (19) Cui, Z.; Burns, R. G.; DiSalvo, F. J. Mesoporous Ti<sub>0.5</sub>Nb<sub>0.5</sub>N Ternary Nitride as a Novel Noncarbon Support for Oxygen Reduction Reaction in Acid and Alkaline Electrolytes. *Chem. Mater.* **2013**, *25*, 3782–2784.

- (20) Ding, X.; Yin, S.; An, K.; Luo, L.; Shi, N.; Qiang, Y.; Pasupathi, S.; Pollet, B. G.; Shen, P. K. FeN stabilized FeN@Pt core-shell nanostructures for oxygen reduction reaction. *J. Mater. Chem. A* **2015**.
- (21) Yang, M.; Cui, Z.; DiSalvo, F. J. Mesoporous chromium nitride as a high performance non-carbon support for the oxygen reduction reaction. *Phys. Chem. Chem. Phys.* **2013**, *15*, 7041–7044.
- (22) Petrykina, R. Y.; Shvedova, L. K. Hot pressing of transition metal nitrides and their properties. *Sov. Powder Metall. Met. Ceram.* **1972**, *11*, 276–279.
- (23) Li, Y.; Meng, W.-J.; Swathirajan, S.; Harris, S. J.; Doll, G. L. Lightweight power sources having proton exchange membrane as separator and aluminum or titanium-core contactors with protective coatings and discontinuous titanium nitride topcoats **1997**.
- (24) Lide, D. R. *CRC Handbook of Chemistry and Physics*; 86th Edition.; Taylor & Francis Group, 2005.
- (25) Saha, N. C.; Tompkins, H. G. Titanium nitride oxidation chemistry: An x-ray photoelectron spectroscopy study. *J. Appl. Phys.* **1992**, *72*, 3072–3079.
- (26) Avasarala, B.; Murray, T.; Li, W.; Haldar, P. Titanium nitride nanoparticles based electrocatalysts for proton exchange membrane fuel cells. *J. Mater. Chem.* **2009**, *19*, 1803–1805.
- (27) François, J. C.; Massiani, Y.; Gravier, P.; Grimblot, J.; Gengembre, L. Characterization and optical properties of thin films formed on TiN coatings during electrochemical treatments. *Thin Solid Films* **1993**, *223*, 223–229.
- (28) Nam, N. D.; Vaka, M.; Tran Hung, N. Corrosion behavior of TiN, TiAlN, TiAlSiN-coated 316L stainless steel in simulated proton exchange membrane fuel cell environment. *J. Power Sources* **2014**, *268*, 240–245.
- (29) Wittmer, M. TiN and TaN as diffusion barriers in metallizations to silicon semiconductor devices. *Appl. Phys. Lett.* **1980**, *36*, 456–458.
- (30) Münz, W.-D. Titanium aluminum nitride films: A new alternative to TiN coatings. *J. Vac. Sci. Technol. A* **1986**, *4*, 2717–2725.
- (31) Ait-Djafer, A. Z.; Saoula, N.; Aknouche, H.; Guedouar, B.; Madaoui, N. Deposition and characterization of titanium aluminum nitride coatings prepared by RF magnetron sputtering. *Appl. Surf. Sci.* **2015**, *350*, 6–9.
- (32) Rachbauer, R.; Holec, D.; Mayrhofer, P. H. Increased thermal stability of Ti–Al–N thin films by Ta alloying. *Surf. Coat. Technol.* **2012**, *211*, 98–103.
- (33) Zhu, L.; Hu, M.; Ni, W.; Liu, Y. High temperature oxidation behavior of Ti<sub>0.5</sub>Al<sub>0.5</sub>N coating and Ti<sub>0.5</sub>Al<sub>0.4</sub>Si<sub>0.1</sub>N coating. *Vacuum* **2012**, *86*, 1795–1799.
- (34) Liu, X.; Ma, G. J.; Sun, G.; Duan, Y. P.; Liu, S. H. The influence of Ti doping on the mechanical properties of TaN film. *Surf. Coat. Technol.* **2012**, *212*, 128–133.
- (35) Koller, C. M.; Hollerweger, R.; Sabitzer, C.; Rachbauer, R.; Kolozsvári, S.; Paulitsch, J.; Mayrhofer, P. H. Thermal stability and oxidation resistance of arc evaporated TiAlN, TaAlN, TiAlTaN, and TiAlN/TaAlN coatings. *Surf. Coat. Technol.* **2014**, *259*, Part C, 599–607.
- (36) Patel, N.; Wang, S.; Inspektor, A.; Salvador, P. A. Secondary hardness enhancement in large period TiN/TaN superlattices. *Surf. Coat. Technol.* **2014**, *254*, 21–27.
- (37) Pfeiler, M.; Fontalvo, G. A.; Wagner, J.; Kutschej, K.; Penoy, M.; Michotte, C.; Mitterer, C.; Kathrein, M. Arc Evaporation of Ti–Al–Ta–N Coatings: The Effect of Bias Voltage and Ta on High-temperature Tribological Properties. *Tribol. Lett.* **2008**, *30*, 91–97.
- (38) Pfeiler, M.; Scheu, C.; Hutter, H.; Schnöller, J.; Michotte, C.; Mitterer, C.; Kathrein, M. On the effect of Ta on improved oxidation resistance of Ti–Al–Ta–N coatings. *J. Vac. Sci. Technol. A* **2009**, *27*, 554–560.

- (39) Kathrein, M.; Michotte, C.; Penoy, M.; Polcik, P.; Mitterer, C. Multifunctional multi-component PVD coatings for cutting tools. *Surf. Coat. Technol.* **2005**, *200*, 1867–1871.
- (40) O’Dea, J. R.; Holtz, M. E.; Legard, A. E.; Young, S. D.; Burns, R. G.; Van Wassen, A. R.; Muller, D. A.; Abruña, H. D.; DiSalvo, F. J.; van Dover, R. B.; Marohn, J. A. Conductivity and Microstructure of Combinatorially Sputter-Deposited Ta-Ti-Al Nitride Thin Films. *Chem. Mater.* **2015**.
- (41) Van Wassen, A. R.; Legard, A. E.; O’Dea, J. R.; Young, S. D.; DiSalvo, F. J.; Marohn, J. A.; van Dover, R. B.; Abruña, H. D. Electrochemical Characterization of Ta-Ti-Al Nitride Thin Films. *Chem. Mater.* *Submitted*.
- (42) Kim, I.; Kumta, P. N. Hydrazide sol–gel process: A novel approach, for synthesizing nanostructured titanium nitride. *Mater. Sci. Eng. B* **2003**, *98*, 123–134.
- (43) Kaskel, S.; Schlichte, K.; Chaplais, G.; Khanna, M. Synthesis and characterisation of titanium nitride based nanoparticles. *J. Mater. Chem.* **2003**, *13*, 1496–1499.
- (44) Faulhaber, S.; Loeffler, L.; Hu, J.; Kroke, E.; Riedel, R.; Lange, F. F. Synthesis of nanocrystalline aluminum–gallium nitride ( $\text{Al}_x\text{Ga}_{1-x}\text{N}$ ;  $x = 0.1$  to  $0.5$ ) with oxide precursors via ammonolysis. *J. Mater. Res.* **2003**, *18*, 2350–2358.
- (45) Dong, S.; Chen, X.; Gu, L.; Zhou, X.; Xu, H.; Wang, H.; Liu, Z.; Han, P.; Yao, J.; Wang, L.; Cui, G.; Chen, L. Facile Preparation of Mesoporous Titanium Nitride Microspheres for Electrochemical Energy Storage. *ACS Appl. Mater. Interfaces* **2011**, *3*, 93–98.
- (46) Schwenger, B.; Loeffler, L.; Seshadri, R.; Keller, S.; Lange, F. F.; DenBaars, S. P.; Mishra, U. K. Preparation of indium nitride micro- and nanostructures by ammonolysis of indium oxide. *J. Mater. Chem.* **2004**, *14*, 637–641.
- (47) Claridge, J. B.; York, A. P. E.; Brungs, A. J.; Green, M. L. H. Study of the Temperature-Programmed Reaction Synthesis of Early Transition Metal Carbide and Nitride Catalyst Materials from Oxide Precursors. *Chem. Mater.* **2000**, *12*, 132–142.
- (48) Yang, M.; MacLeod, M. J.; Tessier, F.; DiSalvo, F. J. Mesoporous Metal Nitride Materials Prepared from Bulk Oxides. *J. Am. Ceram. Soc.* **2012**, *95*, 3084–3089.
- (49) Yang, M.; Ralston, W. T.; Tessier, F.; Allen, A. J.; DiSalvo, F. J. Mesoporous VN prepared by solid–solid phase separation. *J. Solid State Chem.* **2013**, *197*, 398–401.
- (50) Wheeler, R. C.; Frost, G. B. A Comparative Study of the Dehydration Kinetics of Several Hydrated Salts. *Can. J. Chem.* **1955**, *33*, 546–561.
- (51) Yang, M.; Cui, Z.; DiSalvo, F. J. Mesoporous titanium nitride supported Pt nanoparticles as high performance catalysts for methanol electrooxidation. *Phys. Chem. Chem. Phys.* **2012**, *15*, 1088–1092.
- (52) Zhou, Z.; Wang, S.; Zhou, W.; Wang, G.; Jiang, L.; Li, W.; Song, S.; Liu, J.; Sun, G.; Xin, Q. Novel synthesis of highly active Pt/C cathode electrocatalyst for direct methanol fuel cell. *Chem. Commun.* **2003**, 394–395.
- (53) Subban, C. V.; Smith, I. C.; DiSalvo, F. J. Interconversion of Inverse Opals of Electrically Conducting Doped Titanium Oxides and Nitrides. *Small* **2012**, *8*, 2824–2832.
- (54) Drygaś, M.; Czosnek, C.; Paine, R. T.; Janik, J. F. Two-Stage Aerosol Synthesis of Titanium Nitride TiN and Titanium Oxynitride TiO<sub>x</sub>N<sub>y</sub> Nanopowders of Spherical Particle Morphology. *Chem. Mater.* **2006**, *18*, 3122–3129.
- (55) Lee, J.-M.; Han, S.-B.; Song, Y.-J.; Kim, J.-Y.; Roh, B.; Hwang, I.; Choi, W.; Park, K.-W. Methanol electrooxidation of Pt catalyst on titanium nitride nanostructured support. *Appl. Catal. Gen.* **2010**, *375*, 149–155.
- (56) Shannon, R. D.; Prewitt, C. T. Effective ionic radii in oxides and fluorides. *Acta Crystallogr. B* **1969**, *25*, 925–946.

- (57) Shannon, R. D. Revised effective ionic radii and systematic studies of interatomic distances in halides and chalcogenides. *Acta Crystallogr. Sect. A* **1976**, *A32*, 751–767.
- (58) Bearden, J. A. X-Ray Wavelengths. *Rev. Mod. Phys.* **1967**, *39*, 78–124.
- (59) Hojo, J.; Iwamoto, O.; Maruyama, Y.; Kato, A. Defect structure, thermal and electrical properties of Ti nitride and V nitride powders. *J. Common Met.* **1977**, *53*, 265–276.
- (60) Ma, S. S. K.; Hisatomi, T.; Maeda, K.; Moriya, Y.; Domen, K. Enhanced Water Oxidation on Ta<sub>3</sub>N<sub>5</sub> Photocatalysts by Modification with Alkaline Metal Salts. *J. Am. Chem. Soc.* **2012**, *134*, 19993–19996.
- (61) Lee, H. M.; Kim, D. K. High-strength AlN ceramics by low-temperature sintering with CaZrO<sub>3</sub>–Y<sub>2</sub>O<sub>3</sub> co-additives. *J. Eur. Ceram. Soc.* **2014**, *34*, 3627–3633.
- (62) Bang, J. H.; Suslick, K. S. Dual Templating Synthesis of Mesoporous Titanium Nitride Microspheres. *Adv. Mater.* **2009**, *21*, 3186–3190.
- (63) U.S. DRIVE Partnership Fuel Cell Technical Team Cell Component Accelerated Stress Test and Polarization Curve Protocols for Polymer Electrolyte Membrane Fuel Cells **2010**.
- (64) Pourbaix, M. *Atlas of Electrochemical equilibria in Aqueous Solutions*; 2nd Edition.; National Association of Corrosion Engineers, 1974.

## CHAPTER 3

### METHODS: ROTATING DISK ELECTRODE VOLTAMMETRY OF THIN FILMS OF NOVEL OXIDE MATERIALS

Ryo H. Wakabayashi<sup>^</sup>, Hanjong Paik<sup>#</sup>, Marc J. Murphy<sup>#</sup>, R. Bruce van Dover<sup>#</sup>, Darrell  
Schlom<sup>#</sup>, Héctor D. Abruña<sup>^</sup>

<sup>^</sup>Department of Chemistry, Cornell University, Ithaca, New York 14853-1301

<sup>#</sup>Department of Material Science and Engineering, Cornell University, Ithaca, New  
York 14853-1301

#### **3.1 Abstract**

A custom-built apparatus for performing rotating disk electrode voltammetry (RDE) using vapor-deposited thin film samples as rotating electrodes is described. This method allows for quantitative electrochemical characterization using thin film samples, including those deposited on insulating substrates, and it allows for very facile exchange of samples. Cyclic voltammetry and RDE voltammetry of iron ferricyanide was explored to examine if the system causes unusual deviations from an ideal hydrodynamic voltammetric behavior. This was also used to examine the ORR activity of a platinum thin film as a model system for a higher-current reaction relevant to fuel-cell research. Both studies indicated that the set-up does not cause any deviations anticipated from RDE behavior, indicating that this is a viable method for performing rotating disk electrode voltammetry of vapor-deposited thin films, with emphasis on those relevant to fuel cell research.

#### **3.2 Introduction**

Fuel cells, with a potential for higher energy efficiency, are a promising alternative technology to internal combustion engines; however, there are many issues that need to be addressed in order to make the technology more viable and affordable, including the cost of catalysts. In today's polymer electrolyte membrane fuel cells (PEMFC), platinum and/or

platinum-based catalysts are used as the catalyst in both the cathode and the anode, which accounts for a significant portion of the cost of fuel cell stacks<sup>1</sup>. A potential alternative in this context may be an alkaline electrolyte system. One of the biggest barriers for alkaline fuel cells has been the development of a good anion-exchange membrane<sup>2</sup>, but in recent years several reports of viable (anionic) hydroxide-conducting membranes<sup>3,4,5,6</sup> that can be used as an alkaline exchange membrane have been reported. This makes the discovery of less expensive alternatives to platinum more important, especially given that the oxygen reduction reaction (ORR) on platinum still requires at least 300 mV of overpotentials to generate a sufficiently high current density. A major potential benefit of an alkaline fuel cell system is that many non-noble metals, and even non-metals,<sup>7,8,9</sup> are viable candidates as catalysts. In particular, oxides are a class of compounds that may be of great use because many of them are durable (they are already at least partially oxidized) and can be electrically conductive. Manganese and cobalt oxides<sup>10,11</sup>, ruthenium oxide<sup>12</sup>, perovskites<sup>13,14</sup> and some pyrochlore ruthenates<sup>15,16</sup> have been reported as potentially useful ORR catalysts in the past, but a systematic study would surely advance the field.

Vapor deposition methods, such as sputtering, are useful tools to deposit thin layers of highly controlled, clean surfaces, making them useful for many applications, including but not limited to semiconductors and coatings. In particular, molecular beam epitaxy (MBE) is a deposition method that can produce defect-free single crystals with well-defined surfaces. These properties make MBE a very useful and attractive technique to fabricate semiconductor devices<sup>17,18</sup>, superconductors<sup>19</sup>, ferromagnets<sup>20</sup>, and other technologically relevant materials. These properties, in principle, are also useful for investigating the electrocatalytic properties of many crystalline compounds, as electrocatalysis is highly sensitive to surface structure and composition.

A main challenge, however, lies in electrochemical characterization of thin film samples prepared by vapor deposition methods, such as MBE. There have been reports of electrochemical experiments using elaborate custom-made setups<sup>21</sup>, or several simple cyclic voltammetry experiments using conductive substrates<sup>22,23,24</sup> or custom-made cells<sup>25,26,27,28</sup>. These are complicated systems and generally not applicable to a significant portion of thin film samples made using vapor deposition methods, in no small part because many of the most commonly used substrates (silicon, sapphire, etc.) are poor electrical conductors. As such, a facile yet versatile and reproducible way of making a good electrical connection from a deposited sample to the rest of the circuit would be highly beneficial.

In addition, the ORR is not easy to characterize by cyclic voltammetry, because the concentration profile of oxygen in stagnant solutions can be very ill-defined. It also has a two-electron pathway (producing hydrogen peroxide) and a four-electron pathway (producing water), and the two can take place concurrently, further complicating matters. We have previously published a methodology to characterize fuel oxidation reactions on combinatorially sputtered thin films using a scanning-probe differential electrochemical mass spectrometer (DEMS) that can detect and quantify volatile products<sup>29</sup>, and other research groups have done similar experiments since<sup>30</sup>, but the products of the ORR, hydrogen peroxide and/or water (deprotonated in alkaline solution), are not detectable using DEMS.

Rotating disk electrode voltammetry (RDE) is a well-established hydrodynamic voltammetry method that can address the issues by having well-defined and controlled mass transport. Its use enables the deconvolution of mass transport effects from kinetic effects, a difficult task to do with (regular) cyclic voltammetry. By applying the Levich and the Koutecky-Levich equations, parameters such as the number of electrons transferred, kinetics of electron transfer, and mechanism of electrochemical reactions can be extracted. There have

been a few published RDE voltammetry studies on thin film electrodes<sup>31,32,33</sup>, but those studies were performed using custom-made substrates that limit the applicable methods of deposition.

Herein, we describe a facile method to turn thin film oxide/substrates into rotating disk electrodes that behaves just like a commercial RDE electrode. The setup allows for facile and reproducible assembly and disassembly without damaging the film electrodes. We employed sputtered gold and platinum films as model cases to demonstrate that the method is viable.

### 3.3 Methods/Description of the Instrument

#### 3.3.1 Instrumentation

In order to have a better-characterized electrode as a standard, we used a custom-built magnetron sputtering system at the Cornell Center for Materials Research. We deposited an approximately 50 nm of gold on top of an approximately 15 nm thick titanium adhesion layer on a microscope glass slide (VWR) that was cut into 10 mm x 10 mm pieces, all films were front-contacted by applying a thin layer of a conductive silver paste (Ted Pella) and/or a conductive carbon paint (SPI supplies) from the edge of the film to the back of the substrate.

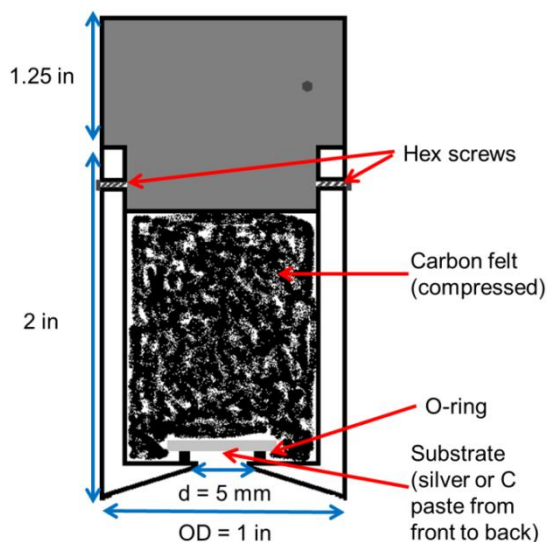


**Figure 3.1.** Schematic of the custom-made rotating disc electrode system.

Figure 3.1 is a simplified diagram of the electrode system. A 1 in diameter Teflon rod was machined to fit a 10 mm x 10 mm electrode. In the center, a 5 mm diameter hole was drilled to expose the sample to the electrode. A recess was made to place an O-ring (0.25 in), in order to prevent liquid leakage into the sample holder. After placing the back-contacted sample inside, the Teflon holder was packed with carbon felt (Alfa Aesar) and capped with a custom-made, stainless-steel current collector (that could be connected to a Pine rotator) by screwing the stainless steel piece to the Teflon piece using small hex screws. This process was carried using a vice to ensure that the carbon felt was well-packed in order to ensure good electrical conductivity.

A custom-made three-compartment cell (Figure 3.2) was used for the RDE electrochemical experiments. The main chamber is 2 inches wide, and has an inner glass basket to prevent cavitation (whirlpool). The three compartments were connected at the bottom with glass frits, and at the top with simple glass tubing (to equalize the pressure in the three compartments). A graphite rod (Sigma Aldrich) was used as the counter electrode and a home-made saturated silver/silver chloride electrode (Ag/AgCl) was used as the reference electrode. No platinum (or any noble metals) was used in the cell to ensure that there was no contamination from trace Pt from pervious experiments<sup>30</sup> (after testing the sputtered Pt and Au films, the cell was soaked in aqua regia for several hours to remove any residual noble metals).



**Figure 3.2.** Photographs of the custom-made 3-compartment electrochemical cell and the custom-made rotating disk electrode. Ruler unit is in inches.

### 3.3.2 EIS

Electrochemical impedance spectroscopy (EIS) was performed using a Solartron 1280B potentiostat, 0.1 M KCl (Macron) or NaOH (Malinckrodt AR) was used as the electrolyte, a graphite rod was used as the counter electrode, and a home-made saturated Ag/AgCl electrode was used as the reference electrode (when necessary). No DC voltage was applied and 5 mV of AC voltage was applied, with a frequency range between 20,000 Hz to 1 Hz.

### 3.3.3 CV and RDE

Cyclic voltammetry (CV) and rotating disk electrode voltammetry (RDE) were performed in 0.1M KCl or NaOH at room temperature. The CV was performed at a scan rate

of 20 mV/s (unless otherwise noted), using a Bioanalytical Systems CV-27.  $K_3[Fe(CN)_6]$  (Sigma, ACS reagent) was used as received. The oxygen reduction reaction was studied at room temperature using rotating disk electrode (RDE) voltammetry at a scan rate of 20 mV/s. The solution was saturated with  $O_2$  (Airgas, UHP) by initially bubbling the solution for 15 minutes and 7 minutes after measurements at each rotation rate, in order to keep the solution remains saturated with oxygen for each recorded scan. During the measurement, the bubbling was stopped to prevent noise in the current induced by bubbles.

Some data were averaged using the Savitzky-Goley method (9 points) to remove periodic noise.

### 3.3.4 Deposition Methods

#### 3.3.4.1 Au

Au thin film was deposited using a CCMR sputtering chamber. The details are discussed in 3.3.1.

#### 3.3.4.2 MBE (deposition done and section written partly by Dr. Hanjong Paik)

Complex oxide films were grown using Veeco GEN 10 dual-oxide MBE chamber. While more detailed experimental procedures can be found in the published literature by the Schlom group, a brief explanation by Dr. Hanjong Paik of the Schlom group is as follows.

Commercially available (111) yttrium-stabilized zirconia (YSZ) was used as substrate for all but one sample. A non-commercial  $Sm_2Ti_2O_7$  (111) substrate was used as the substrate for one sample to achieve a truly epitaxial growth. Prior to growth, the YSZ substrates were heated at 1300 °C for 3 h in air to obtain an atomically flat surface.  $Sm_2Ti_2O_7$  (111) substrate was mechanically polished using diamond paste to obtain an atomically flat surface. For the metals on the A-site (Bi or Pb), an over-pressure supply flux ( $1.0 \times 10^{14}$  atoms/cm<sup>2</sup>·sec) was used during growth, which was approximately 10 to 15 times greater than the the flux for the B-site (Ru or Ir) ( $0.3 \times 10^{13}$  atoms/cm<sup>2</sup>·sec). All components were co-supplied simultaneously

during the growth. Distilled ozone ( $1.0 \times 10^{-6}$  Torr) was used as the oxidant. The growth temperature was maintained at 500-600 °C by optical pyrometer.

To determine the optimal single-phase growth window, *in-situ* reflection high-energy electron diffraction (RHEED) was used. Thin film crystalline quality was checked by four-circle x-ray diffraction with two bounce Ge (220) monochromator (Rigaku, Smartlab), and high-resolution rocking curve was measured by adding two bounce Ge (220) crystal analyzer on the receiving side (triple axis geometry). Film thickness (i.e. growth rate) was limited by the Sn-flux supply, which was consistent with the QCM measurement with in  $\pm 10$  % error. The spacing of XRD thickness fringes (Kiessig fringes) of main 222 Bragg peak confirmed the film thickness. Rutherford backscattering spectroscopy (RBS) confirmed the film stoichiometry within  $\pm 3$  % measurement error. Cross-sectional high-angle dark field (HAADF) scanning transmission electron microscopy (STEM) revealed the interface structure (FEI Technai F-20 TEM/STEM in STEM mode with a beam voltage of 200 keV). The surface morphology was characterized by atomic force microscopy (AFM). For XRD, RBS, STEM, and AFM data, refer to future published literature by Paik and Schlom.

#### 3.3.4.3 *Co-sputtering* (deposition done and section written partly by Marc Murphy)

Films were also grown by the van Dover group. The details are shown in other publications by the van Dover group. The following is a brief description of the deposition procedure, courtesy of Marc Murphy of the van Dover group.

Binary composition spread thin film was deposited through off-axis reactive RF co-sputtering of any combination of Pb, Bi, Ir, and Pt, onto a 76.2 mm diameter silicon wafer. Prior to sputtering, the silicon wafer was heated to 1000 °C to form a SiO<sub>2</sub> buffer layer. The chamber was initially evacuated to a base pressure of  $\sim 2 \times 10^{-6}$  Torr, and a steady flow of 15 sccm Ar and 10 sccm O<sub>2</sub> gas was subsequently introduced up to a partial pressure of 30 mTorr. The appropriate power was applied the targets to ensure an approximate 1:1 mole

ratio at the center of the film, based on calibration depositions. Following a 10-15 minute pre-sputter step, the thin films with a composition spread was deposited, with a thickness ranging from 150-400 nm across the film. Upon deposition, the film was annealed at 600 °C in an air furnace for 1 hour.

One sample was annealed using a laser anneal apparatus. The details of the annealing process can be found in this reference.<sup>34</sup> Very briefly, a continuous wave laser was swept across the sample, which heats the sample at over 100 °C/s, and typical dwell times are in the order of 0.2 – 5 ms.

For the  $\text{Mn}_x\text{Ru}_y\text{O}_z$  film, the procedures were slightly different. Multiple binary manganese ruthenium oxide (Mn-Ru-O) composition spread thin films were deposited onto 76.2 (3") mm diameter silicon (100) wafers through off-axis reactive RF co-sputtering. Before placing a substrate in the sputtering chamber, the silicon wafers was heated in air at 1000 °C for 40 hours to grow a thin  $\text{SiO}_2$  buffer layer. In order to improve the conductivity of the film for electrochemical characterization, some of the films were coated with a conductive 60 nm Ru metal through DC sputtering in 10 mTorr Ar, prior to the co-sputter step. A steady flow of 40 sccm Ar and 10 sccm  $\text{O}_2$  gas (20%  $\text{O}_2$ ) was introduced until an  $\text{O}_2$  partial pressure of 30 mTorr was reached. The applied power to the Mn and Ru targets were set to 90 to 50 W, respectively, so as to ensure an approximate 1:1 mole ratio at the center of the film. Following a 10-15 minute pre-sputter step in order to ensure steady co-sputtering, Mn and Ru were then sputtered onto the substrate for 20 minutes, resulting in a Mn-Ru-O composition spread with a thickness ranging from 150-400 nm across the film. The films were annealed in-situ at ~350 °C using a substrate holder with a built-in resistive heater. The samples were cleaved to 10 mm square pieces for testing using the custom-built RDE system described in this chapter.

### ***3.4 Operations/Results and Discussions***

#### ***3.4.1 EIS***

Our electrode setup has a somewhat unconventional method for making electrical connection from the electrode to the current collector. To investigate the validity of this method, reduction (and oxidation) of  $\text{K}_3[\text{Fe}(\text{CN})_6]$  (0.81 mM) in 0.1 M KCl, a well-studied electrochemical reaction, was investigated on a sputtered gold (approx. 50 nm thick) electrode, and the results were compared to a bulk Au electrode ( $d = 5$  mm).

Figure 3.3 shows the Nyquist plots of the thin film and bulk Au electrodes in 0.1 M KCl (with no other redox-active components). Total linear resistance (first x-intercept, i.e. impedance at which there is no capacitive contribution) is approximately 190 ohms for the thin film, whereas it is approximately 90 ohms for the bulk gold electrode. EIS was performed with the reference electrode being placed directly adjacent to the working electrode in order to see if the rather long distance between the compartment introduced a junction potential, but it did not (see Figure 3.4). It is clear that the distance between the reference and the working electrode in this set-up did not introduce a significant ohmic drop.

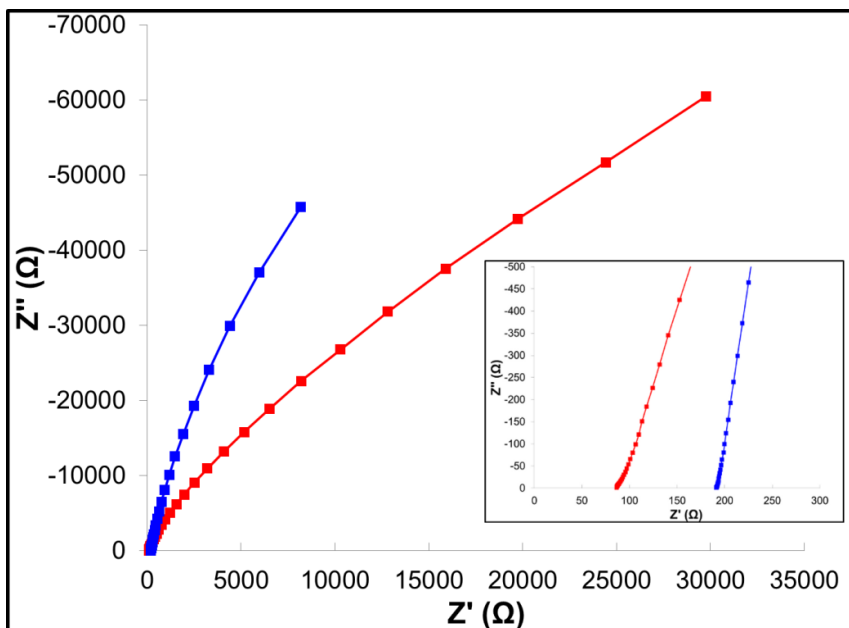


**Figure 3.3.** Nyquist plots of Au film (blue) and bulk Au (red) in 0.1M KCl, at OCP, 5 mV AC, 20,000 Hz – 1 Hz ( $Z'$  and  $Z''$  increase as the frequency decreases)

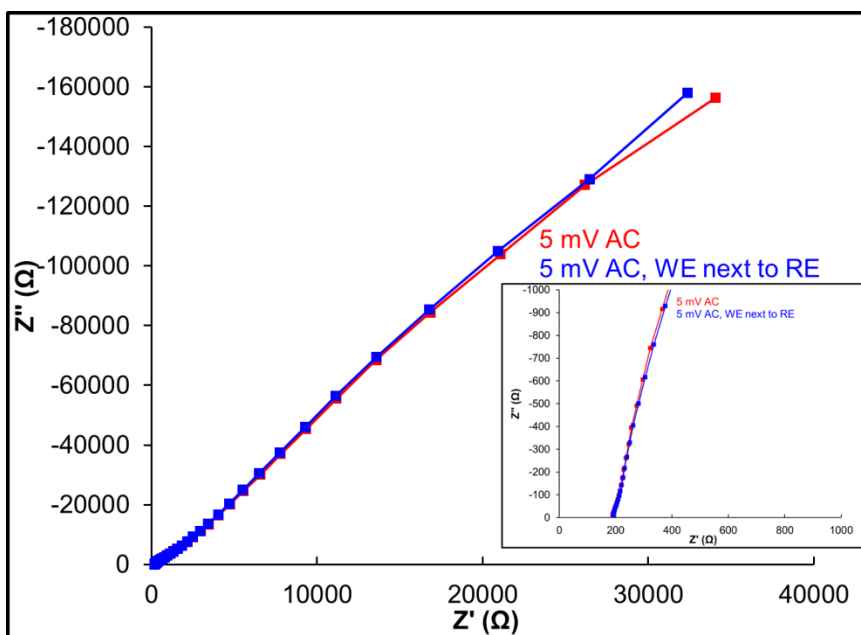


**Figure 3.4.** Nyquist plots of Au film with RE in its own compartment (red) and with the reference electrode moved directly adjacent to the working electrode (blue) in 0.1M KCl, at OCP, 5 mV AC, 20,000 Hz – 1 Hz ( $Z'$  and  $Z''$  increase as the frequency decreases)

### 3.4.2 CV and RDE of $K_3[Fe(CN)_6]$

The cyclic voltammetry 0.1M KCl does not show an evidence of a significant  $iR$ -drop (Figure 3.5); in fact, the surface gold oxidation and reduction peaks are more visible on the CV of the thin film electrode (Figure 3.5(b)). Noisy parts of the CV of thin film Au around 0 V vs. Ag/AgCl in the negative-going sweep (Figure 3.5(b)) is likely due to the local pH change induced by the surface oxide reduction, since the electrolyte is not buffered. It is not a major concern for the rest of the experiment, as the potential range used for redox of  $K_3[Fe(CN)_6]$  lacks the surface redox processes (Red CVs of Figure 3.5). The difference in series resistance, however, is somewhat noticeable in cyclic voltammogram (CV) of  $K_3[Fe(CN)_6]$  in 0.1 M KCl (Figure 3.6) on sputtered gold, performed with various scan rates. The peak-to-peak separation between the oxidation and the reduction of ferricyanide increases with increasing scan rate when the thin film Au was used as the electrode, indicating some resistance issues. On the other hand, there is only a minimal increase in the peak-to-peak separation as a function of the scan rate on the CV of the same reaction using the bulk gold electrode. Still, carrying out experiments at relatively slow scan rates (as it would be ideal for RDE voltammetry) would eliminate any concerns.

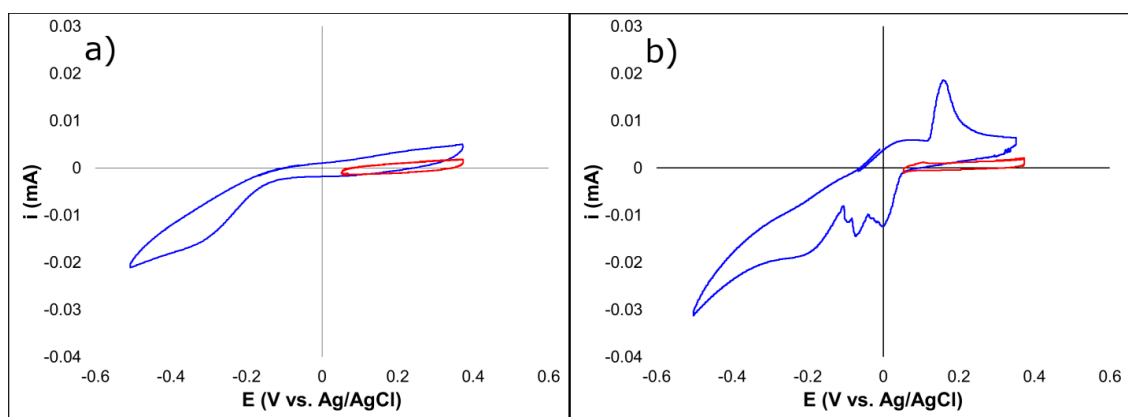


**Figure 3.5.** Cyclic voltammograms of bulk (a) and film (b) Au in 0.1M KCl. Scan rate 20 mV/s. Red: potential range used for CV of  $K_3[Fe(CN)_6]$ .

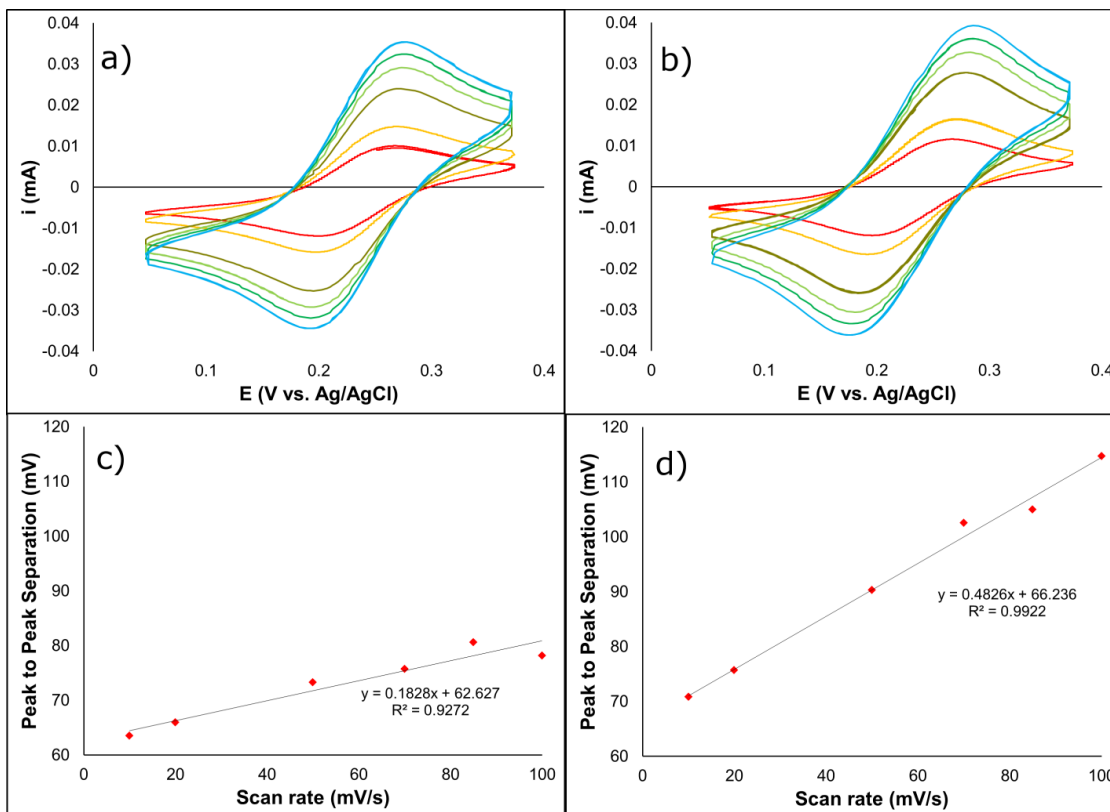


**Figure 3.6.** Cyclic voltammogram of 0.81 mM  $K_3[Fe(CN)_6]$  in 0.1 M KCl on bulk (a) Au and sputtered gold (approx. 50 nm thick; b), and peak-to-peak separations of the oxidation and reduction peaks (c is for bulk Au, d is for thin film Au). Scan rates are 10 (red), 20 (orange), 50 (mustard), 70 (light green), 85 (green) and 100 (light blue) mV/s.

An ideal rotating disk electrode has a flat surface, so as to establish laminar flow. As evident in Figure 3.1, the holder described in this paper has two irregularities; the electrode is recessed by the thickness of the O-ring (approx. 2 mm), and the Teflon surface slants downward towards the electrode. To investigate the effect of such irregularities, the reduction of  $K_3[Fe(CN)_6]$  (0.81 mM) in 0.1 M KCl was investigated using the standard RDE technique at a scan rate of 20 mV/s. Figure 3.7 shows the results of the experiment. The kinetic regions (including the onset potential) of the two RDE voltammograms look nearly identical, aside from the systematic offset in current introduced by the slight difference in the double layer

current. Applying the Levich equation  $i_L = 0.620nFAD^{2/3}\omega^{1/2}\nu^{-1/6}C_0$  (F = Faraday constant, A = area of the electrode, number of electron transferred n = , and kinematic viscosity  $\nu = 9.913 \times 10^{-3} \text{ cm}^2/\text{s}$  for 0.1 M KCl<sup>35</sup>) at 0.06 V vs. Ag/AgCl (Figure 3.7(d)), the diffusion coefficient (D) was determined to be  $7.6 \times 10^{-6} \pm 0.7 \text{ cm}^2/\text{s}$  , which is very close to the value given in the literature ( $7.6 \times 10^{-6} \text{ cm}^2/\text{s}$ <sup>36</sup>). As a comparison, the identical experiment was performed in the same solution using a bulk Au electrode (Figure 3.7(a)). Using the same assumptions, the diffusion coefficient was determined to be  $7.5 \times 10^{-6} \text{ cm}^2/\text{s}$ . An interesting quirk of The Levich plot of thin film RDE is that the intercept of the best-fit line is below zero, when in theory it should be zero (or often times positive). Taken for its face value, it would mean that at the limit of no rotation, the limiting current of a reduction reaction would show a positive current, which is clearly unphysical. While it is difficult to ascribe the cause for such a phenomenon, the slope is still linear with a very high coefficient of determination ( $r^2$ ), which is sufficient for extracting parameters like the diffusion coefficient or the number of electrons. Therefore, we do not believe this to be a significant problem.

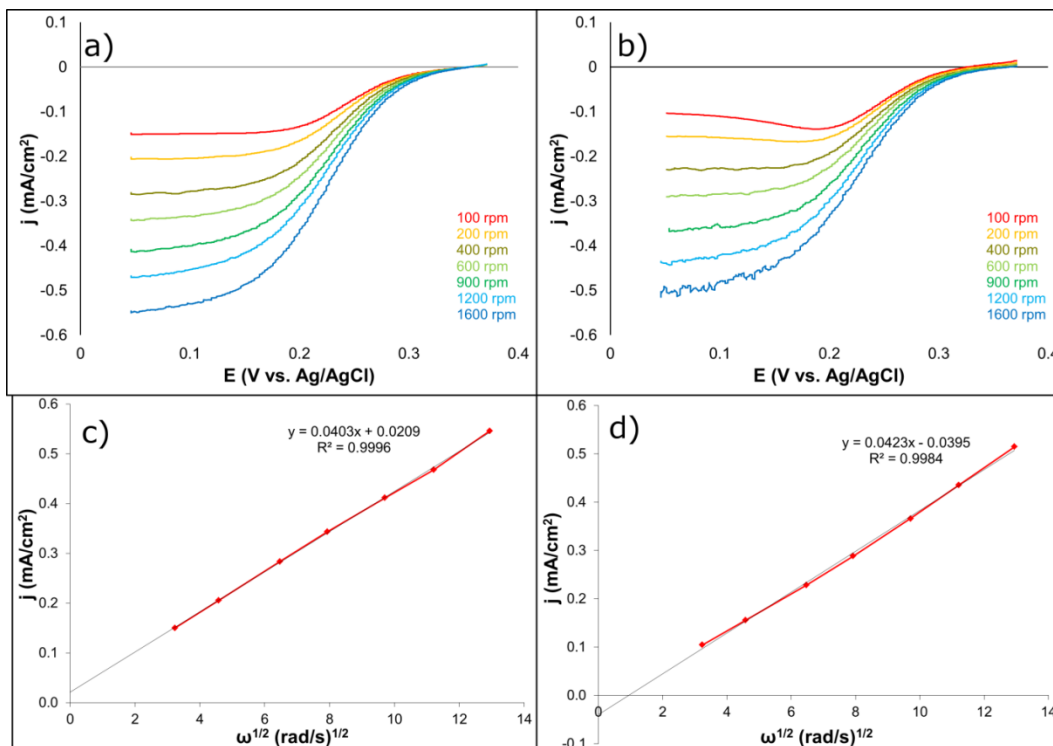


**Figure 3.7.** Rotating disk electrode voltammetry of 0.81 mM  $K_3[Fe(CN)_6]$  in 0.1 M KCl on bulk Au (a) and Au film (b). (c) Levich plots at 0.06 V vs. Ag/AgCl of bulk Au and Au

### 3.4.3 ORR on Pt thin film

One of the greatest benefits of RDE voltammetry is the ability to quantify electrochemical redox processes. RDE voltammetry of the ORR was carried out in 0.1 M NaOH using a sputtered Pt electrode (see Figure 3.8(a)). The voltammetric profiles are in line with reported ORR voltammograms of Pt. The Levich plot (Figure 3.8 (b)), made using current densities at -0.6 V vs. Ag/AgCl yields an excellent best-fit line ( $r^2 = 0.9999$ ) and  $n = 3.87$  electrons from the Levich equation (assuming diffusion coefficient of  $O_2$  in water of  $D = 1.93 \cdot 10^{-5} \text{ cm}^2/\text{s}$ ,  $C_0 = 1.26 \cdot 10^{-3} \text{ M } O_2$  at saturation, and kinematic viscosity  $\nu = 1.07 \cdot 10^{-2} \text{ cm}^2/\text{s}$ , all based on values reported in the literature<sup>37</sup>). Though the mass-transport region of Figure 3.7(a) is not strictly flat, it shows negligible to no difference on the Levich plot (Figure 3.7(b)). General current and voltammetric profiles are in line with reported values as

well<sup>38,39,40,41,42,43</sup>. This is a further proof that the dimensions and configurations of the holder/electrode are sufficiently optimized for testing thin-film electrodes in electrochemical cells for reactions such as the ORR.

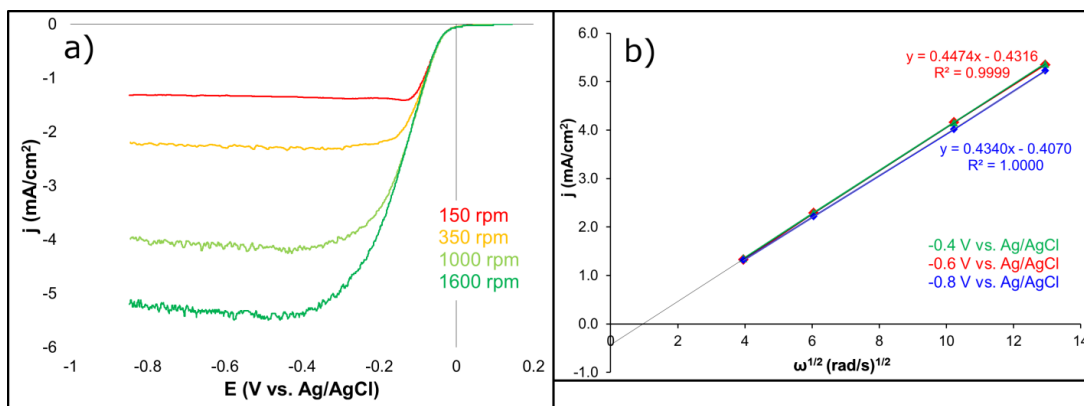


**Figure 3.8** (a) RDE voltammogram of sputtered Pt in oxygen-saturated 0.1M NaOH, measured using a home-made electrode setup. (b) Levich plot, generated from current densities at -0.4 V (green), -0.6 V (red) and -0.8 V (blue) vs. Ag/AgCl, with equations for the linear regression lines for the data from -0.6V and -0.8 V.

#### 3.4.4 ORR and OER on MBE Samples (from Paik/Schlom Group)

Figure 3.9 shows the Nyquist plots of oxide thin film electrodes (MBE) in 0.1M NaOH. It is clear that the oxide thin films are more resistive than a standard electrode, with the series resistance (can be approximated from the first x-intercept) being about twice that of the GC electrode in the case of IrO<sub>2</sub>, and two orders of magnitude higher in the case of Pb<sub>2</sub>Ir<sub>2</sub>O<sub>7</sub>.

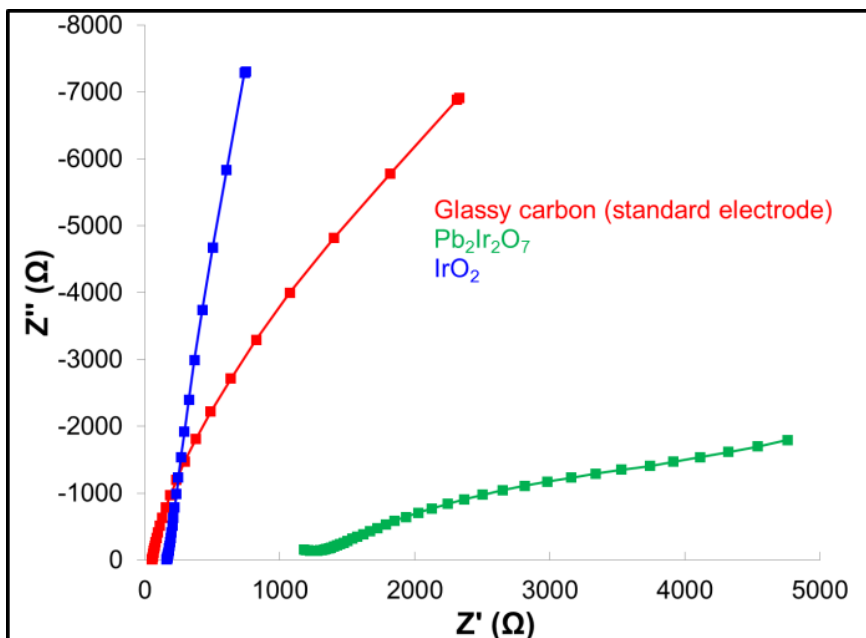


**Figure 3.9** Nyquist plots of selected MBE pyrochlore samples. A glassy carbon electrode is a standard electrode (the RDE electrode setup described in this work is not used). OCP, 10 mV AC, 20,000 Hz – 1 Hz ( $Z'$  and  $Z''$  increase as the frequency decreases)

Figure 3.10(a) is a metacomparison of RDE voltammograms of various pyrochlore oxides grown using the Veeco GEN 10 dual-oxide MBE chamber in  $O_2$ -saturated 0.1M NaOH at 1600 rpm. The shallow slopes of the voltammograms strongly suggest that there is a significant  $iR$  drop in these samples; therefore, the most useful parameter to compare is the onset potential.

We tested a series of  $A_2B_2O_7$  pyrochlore samples. The following discussion for the next two paragraphs will center on  $Bi_2Ru_2O_7$  (111) as the standard and will serve as the basis to discuss the effects of substitution and other changes. Among the  $Bi_2Ru_2O_7$  samples (shades of red in Figure 3.10(a)), there is little to no dependence on thickness (20 nm vs. 10 nm) or crystallographic orientation (111 vs. 001). Similarly, introducing strain by epitaxial growth on  $Sm_2Ti_2O_7$  also seems to have little effect on the electrocatalytic activity. The onset potentials ( $E$  when  $j = 0.1 \text{ mA/cm}^2$ ) are all approximately -0.2 V vs. Ag/AgCl. The sample with the best

onset potential of the series (20 nm) was -0.20 V and the worst (001) was -0.23 V. Substitution on B sites of the pyrochlore structures with iridium and forming  $\text{Bi}_2(\text{Ru}/\text{Ir})_2\text{O}_7$  samples (shades of blue in Figure 3.10(a)) magnifies the iR drop significantly, even with a small amount of Ir. However, the onset potential hardly shifts. Substitution on the A site with Pb to form  $\text{Pb}_2\text{Ru}_2\text{O}_7$ , however, improves the onset potential considerably, to -0.14 V vs. Ag/AgCl (lime green in Figure 3.10(a)). Finally, substitution of both the A site and B site from  $\text{Bi}_2\text{Ru}_2\text{O}_7$  to  $\text{Pb}_2\text{Ir}_2\text{O}_7$  significantly decreases the catalytic activity (and, likely, conductivity), with the onset potential decreasing to -0.30 V vs. Ag/AgCl (green). Perhaps these results are not surprising, as  $\text{IrO}_2$  (mustard) is a very poor ORR catalyst (pink line). In short, Pb appears to be the slightly favorable candidate than Bi for the A site cation, and Ru is a far superior B site cation than Ir.

Figure 3.10(b) shows linear sweep voltammetry of the select samples deposited by MBE, examining the OER in  $\text{O}_2$ -saturated 0.1M NaOH. The  $\text{Bi}_2\text{Ru}_2\text{O}_7$  sample shows an onset potential of 0.58 V vs. Ag/AgCl. Substitution of B site with Ir ( $\text{Bi}_2\text{Ir}_2\text{O}_7$ ) does not significantly alter the catalytic activity for the OER. Interestingly, two samples of  $\text{Bi}_2\text{Ir}_2\text{O}_7$  showed dramatically different activities (blue vs. dotted blue), likely dependent on deposition parameters. Partial substitution of Ir with Ru and forming  $\text{Bi}_2(\text{Ir}/\text{Ru})_2\text{O}_7$  (shades of blue) improved the onset and the kinetics slightly, a sharp contrast to the previous figure. Since bulk  $\text{IrO}_2$  is one of the best OER catalysts known<sup>44</sup>, this result is consistent with those observations.  $\text{IrO}_2$  (mustard), however, showed very poor activity, perhaps because of poor conductivity of the thin film sample, as it was shown in Figure 3.9. Substitution of Bi with Pb ( $\text{Pb}_2\text{Ru}_2\text{O}_7$ ) does not alter the catalytic activity at all. In fact, the second sample (dotted line of the same lime green) has one of the best onset potentials (~0.55 V vs. Ag/AgCl).  $\text{Pb}_2\text{Ir}_2\text{O}_7$  (green), substitution of both the A and the B sites of  $\text{Bi}_2\text{Ru}_2\text{O}_7$ , improves the catalytic activity considerably (onset potential ~0.55 V vs. Ag/AgCl, steeper slope). However, it should be

noted that a significant difference was observed between samples (two different lime green lines).

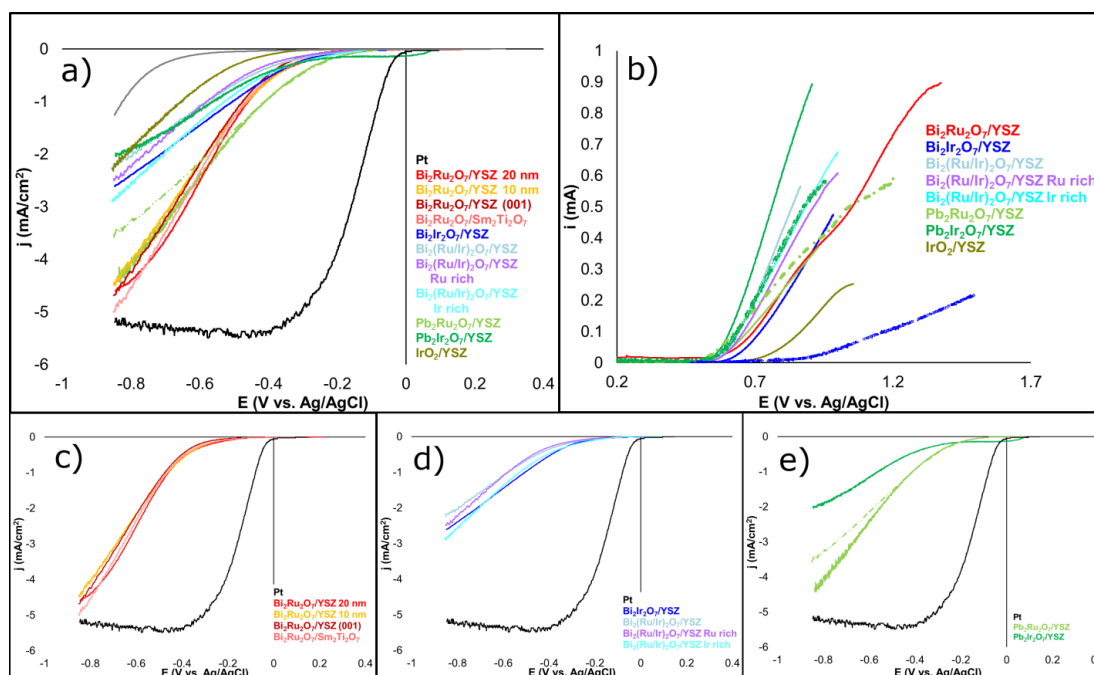


**Figure 3.10.** (a) RDE metacomparison of the oxygen reduction reaction in oxygen-saturated 0.1M NaOH using MBE-grown pyrochlore electrodes. The voltammogram of Pt is copied from Figure 2 (b) Comparison of OER in oxygen-saturated 0.1M NaOH using MBE-grown pyrochlore electrodes. Dotted lines indicate different samples of the same nominal composition. (c) (d) (e) are part (a) divided into three groups of compounds. Colors are matched for same samples on (a) and (b). All samples are (111), unless

### 3.4.5 ORR and OER on Co-sputtered Samples (from Murphy/van Dover Group)

Figure 3.11(a) is a metacomparison plot of RDE voltammetry (1600 rpm) of the ORR using various co-sputtered oxides used as the working electrode in O<sub>2</sub>-saturated 0.1M NaOH. Bi<sub>x</sub>Ir<sub>y</sub>O<sub>7</sub> (two different compositions) and a laser-annealed sample of the same category of the compound that introduced a different crystal structure (for laser annealing process, see ref<sup>34</sup>) (shades of blue) performed poorly, as was seen in pyrochlore thin films made by MBE (Figure 3.10(a)). Three different compositions of Bi<sub>x</sub>Ir<sub>y</sub>O<sub>7</sub> (shades of blue) were tested, and all of them

showed onset potential worse than -0.2 V vs. Ag/AgCl, with very shallow slopes (compared to Pt). Partial substitution of Ir with Pt in  $\text{Bi}_x\text{Ir}_y\text{O}_7$  and forming  $\text{Bi}_x(\text{Ir/Pt})_y\text{O}_7$  (red and brown lines) improved the kinetics (much steeper slope, comparable to Pt), and the sample in brown line shows nearly identical onset potential to Pt (10 mV worse). However, we decided that these samples were not worth further investigation, because they contained Pt and was inferior to Pt itself (black line) with significantly more difficult synthesis and processing than Pt if they were to be made as nanoparticles. One of the  $\text{Bi}_x(\text{Ir/Pt})_y\text{O}_7$  sample and the laser-annealed sample of  $\text{Bi}_x\text{Ir}_y\text{O}_7$  showed unphysically high limiting currents (the limiting current at  $n = 4$  for 1600 rpm should be  $5.26 \text{ mA/cm}^2$ , assuming  $D = 1.93 \times 10^{-5} \text{ cm}^2/\text{s}$ ,  $C_0 = 1.26 \times 10^{-3} \text{ M O}_2$  at saturation, and kinematic viscosity  $\nu = 1.07 \times 10^{-2} \text{ cm}^2/\text{s}$ ), but we attribute that to delamination. The  $\text{Mn}_x\text{Ru}_y\text{O}_z$  sample (orange), however, is extremely interesting sample. Its onset potential (ca. -0.07 V vs. Ag/AgCl) was only about 45 mV worse than Pt, showed a comparable kinetic region to Pt, and reached the same limiting current as Pt, despite not containing any precious metal. We have decided that this sample would be an appropriate candidate to study further, and will be discussed in the following chapter.

Figure 3.11(b) shows linear sweep voltammetry of the select co-sputtered samples in  $\text{O}_2$ -saturated 0.1M NaOH, investigating the OER (colors are matched with Figure 3.11(a)). Most samples showed onset potentials at ca. 0.55 V vs. Ag/AgCl, except for the laser-annealed  $\text{Bi}_x\text{Ir}_y\text{O}_7$ , which did not show any OER activity until 0.6 V vs. Ag/AgCl. All of the samples show better slope than  $\text{IrO}_2$ , however, indicating either better kinetics or less ohmic resistance. Finally, the  $\text{Mn}_x\text{Ru}_y\text{O}_z$  sample (orange) again shows the best onset potential at ca. 0.5 V with kinetics comparable to the other samples. The OER activity will also be discussed further in the following chapter.

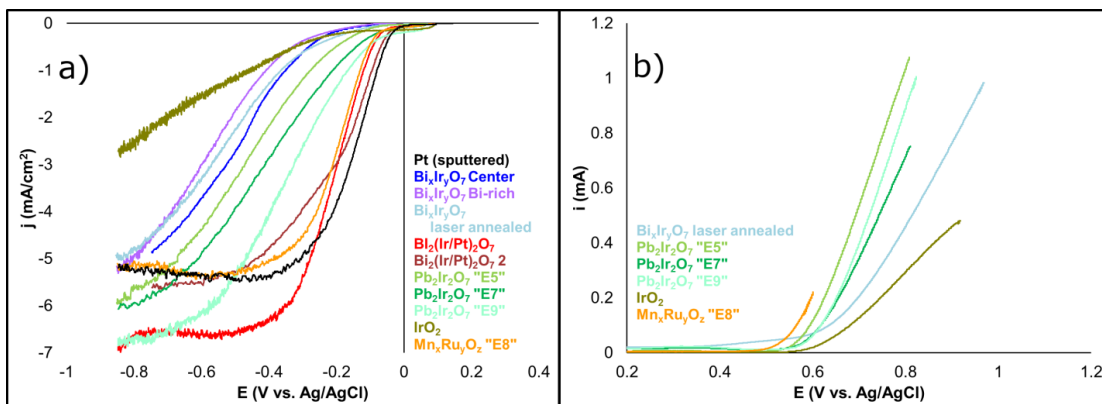


**Figure 3.11.** (a) RDE metacomparison of ORR in O<sub>2</sub>-saturated 0.1 M NaOH using thin film oxide samples deposited by co-sputtering methods. The voltammogram of Pt is copied from Figure 2. (b) Comparison of OER in oxygen-saturated 0.1M NaOH using thin film oxide samples deposited by co-sputtering methods. Colors are matched between (a) and (b).

Figure 3.12 shows RDE voltammograms of the Mn<sub>x</sub>Ru<sub>y</sub>O<sub>z</sub> sample in O<sub>2</sub>-saturated 0.1 M NaOH, scanned at 20 mV/s. At all rotation rates the ORR reached transport limit. Applying the Levich equation at -0.6 V vs. Ag/AgCl yields a nearly perfectly straight line ( $r^2 = 0.9995$ ), confirming that there were no kinetic limitations. The electron count was calculated to be 3.74 (using the same constants listed in the previous paragraph), indicating that the 4-electron reduction pathway, to form hydroxide, was the dominant reaction, instead of the 2-electron process that produces hydrogen peroxide. The direct pathway is the preferred pathway, as it is

the more efficient one.

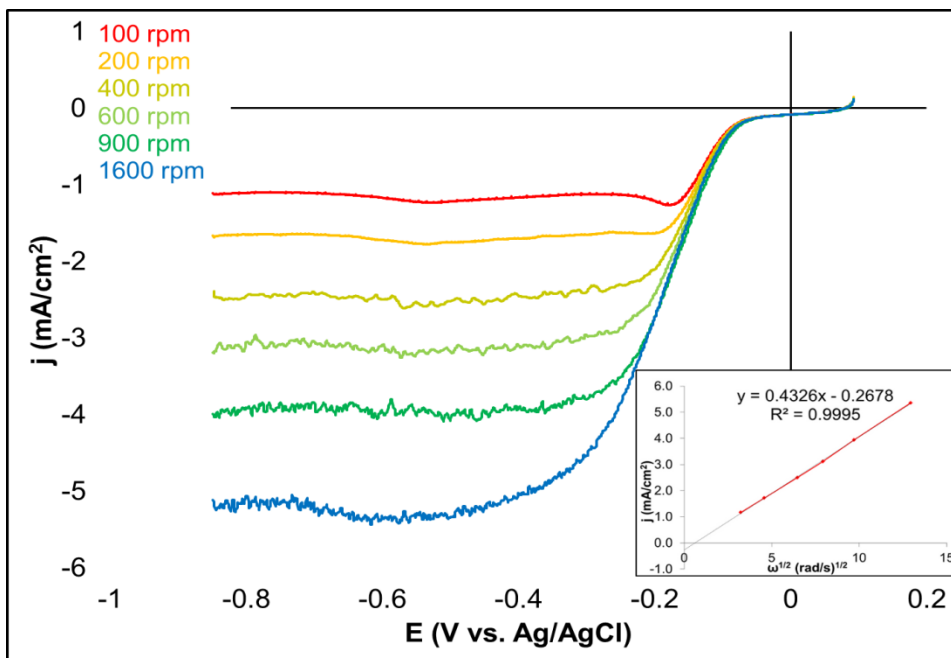


**Figure 3.12.** RDE voltammograms of Mn<sub>x</sub>Ru<sub>y</sub>O<sub>2</sub> "E8" in O<sub>2</sub>-saturated 0.1 M NaOH. Inset: Levich plot from current densities at -0.6 V vs. Ag/AgCl.

### 3.5 Conclusions

A facile method to perform rotating disk electrode voltammetry on thin film electrodes was developed. Using sputter-deposited Au and Pt, it was demonstrated to be a robust method that can be used and configured for thin films. This method would allow for more detailed characterization of reactions such as the oxygen reduction reaction than a simple cyclic voltammetry using deposited thin film electrodes.

We have shown that, while many pyrochlore electrodes made via MBE show somewhat promising electrocatalytic activities in terms of onset potentials, they exhibit significant *iR* drops. Perhaps as a result, the effects of strain caused by epitaxial growth or different crystallographic orientation seem to show negligible difference in the electrocatalytic activity towards the ORR. Pb<sub>2</sub>Ru<sub>2</sub>O<sub>7</sub> is the most promising candidate for further study. In

order to address the iR-drop, perhaps a conductive substrate would mitigate the problem, though such substrates are difficult to obtain, especially for epitaxial growth.

None of the co-sputtered pyrochlore ( $A_2B_2O_7$ ) samples showed promising activities either, but they appeared to be a bit less hampered by ohmic loss. However, these results may mean that pyrochlore structure samples are not a suitable class of materials for the catalysis of the ORR. On the other hand, the  $Mn_xRu_yO_z$  sample showed a very promising result. With this in mind, in the next chapter, synthesis of this compound will be investigated.

### 3.6 Acknowledgments

This work is based upon work supported as part of the Energy Materials Center at Cornell (EMC<sup>2</sup>), an Energy Frontier Research Center funded by the U.S. Department of Energy, Office of Science, and Office of Basic Energy Sciences under Award Number DE-SC0001086. This work was also supported by Cornell University from September 2014 through June 2016. This work made use of the Cornell Center for Materials Research Shared Facilities which are supported through the NSF MRSEC program (DMR-1120296). We would like to thank Robert Bell (Thompson group, Material Science and Engineering, Cornell) for the laser annealing process.

### REFERENCES

- (1) Marcinkoski, J.; Spendelow, J. S.; Wilson, A.; Papageorgopoulos, D. C. DOE Fuel Cell Technologies Office Record 15015: Fuel Cell System Cost - 2015 [https://www.hydrogen.energy.gov/pdfs/15015\\_fuel\\_cell\\_system\\_cost\\_2015.pdf](https://www.hydrogen.energy.gov/pdfs/15015_fuel_cell_system_cost_2015.pdf) (accessed Apr 17, 2016).
- (2) Dombrovskis, J. K.; Palmqvist, A. E. C. Recent Progress in Synthesis, Characterization and Evaluation of Non-Precious Metal Catalysts for the Oxygen Reduction Reaction. *Fuel Cells* **2016**, *16*, 4–22.
- (3) Noonan, K. J. T.; Hugar, K. M.; Kostalik, H. A.; Lobkovsky, E. B.; Abruña, H. D.; Coates, G. W. Phosphonium-Functionalized Polyethylene: A New Class of Base-Stable Alkaline Anion Exchange Membranes. *J. Am. Chem. Soc.* **2012**, *134*, 18161–18164.
- (4) Kostalik, H. A.; Clark, T. J.; Robertson, N. J.; Mutolo, P. F.; Longo, J. M.; Abruña, H. D.; Coates, G. W. Solvent Processable Tetraalkylammonium-Functionalized Polyethylene for Use as an Alkaline Anion Exchange Membrane. *Macromolecules* **2010**, *43*, 7147–7150.
- (5) Couture, G.; Alaaeddine, A.; Boschet, F.; Ameduri, B. Polymeric materials as anion-exchange membranes for alkaline fuel cells. *Prog. Polym. Sci.* **2011**, *36*, 1521–1557.

- (6) Gu, S.; Cai, R.; Luo, T.; Chen, Z.; Sun, M.; Liu, Y.; He, G.; Yan, Y. A Soluble and Highly Conductive Ionomer for High-Performance Hydroxide Exchange Membrane Fuel Cells. *Angew. Chem. Int. Ed.* **2009**, *48*, 6499–6502.
- (7) Ramaswamy, N.; Mukerjee, S. Influence of Inner- and Outer-Sphere Electron Transfer Mechanisms during Electrocatalysis of Oxygen Reduction in Alkaline Media. *J. Phys. Chem. C* **2011**, *115*, 18015–18026.
- (8) Wang, B. Recent development of non-platinum catalysts for oxygen reduction reaction. *J. Power Sources* **2005**, *152*, 1–15.
- (9) Ge, X.; Sumboja, A.; Wu, D.; An, T.; Li, B.; Goh, F. W. T.; Hor, T. S. A.; Zong, Y.; Liu, Z. Oxygen Reduction in Alkaline Media: From Mechanisms to Recent Advances of Catalysts. *ACS Catal.* **2015**, *5*, 4643–4667.
- (10) Queiroz, A. C.; Lima, F. H. B. Electrocatalytic activity and stability of Co and Mn-based oxides for the oxygen reduction reaction in alkaline electrolyte. *J. Electroanal. Chem.* **2013**, *707*, 142–150.
- (11) Du, J.; Chen, C.; Cheng, F.; Chen, J. Rapid Synthesis and Efficient Electrocatalytic Oxygen Reduction/Evolution Reaction of CoMn<sub>2</sub>O<sub>4</sub> Nanodots Supported on Graphene. *Inorg. Chem.* **2015**.
- (12) Abbott, D. F.; Mukerjee, S.; Petrykin, V.; Bastl, Z.; Halck, N. B.; Rossmeisl, J.; Krtil, P. Oxygen reduction on nanocrystalline ruthenium – local structure effects. *RSC Adv.* **2014**, *5*, 1235–1243.
- (13) Poux, T.; Bonnefont, A.; Kéranguéven, G.; Tsirlina, G. A.; Savinova, E. R. Electrocatalytic Oxygen Reduction Reaction on Perovskite Oxides: Series versus Direct Pathway. *ChemPhysChem* **2014**, *15*, 2108–2120.
- (14) Suntivich, J.; Gasteiger, H. A.; Yabuuchi, N.; Nakanishi, H.; Goodenough, J. B.; Shao-Horn, Y. Design principles for oxygen-reduction activity on perovskite oxide catalysts for fuel cells and metal–air batteries. *Nat. Chem.* **2011**, *3*, 546–550.
- (15) Horowitz, H. S.; Longo, J. M.; Horowitz, H. H. Oxygen Electrocatalysis on Some Oxide Pyrochlores. *J. Electrochem. Soc.* **1983**, *130*, 1851–1859.
- (16) Egdell, R. G.; Goodenough, J. B.; Hamnett, A.; Naish, C. C. Electrochemistry of ruthenates. Part 1.—Oxygen reduction on pyrochlore ruthenates. *J. Chem. Soc. Faraday Trans. 1 Phys. Chem. Condens. Phases* **1983**, *79*, 893–912.
- (17) Abernathy, C. R. Compound semiconductor growth by metallorganic molecular beam epitaxy (MOMBE). *Mater. Sci. Eng. R Rep.* **1995**, *14*, 203–253.
- (18) Özgür, Ü.; Alivov, Y. I.; Liu, C.; Teke, A.; Reshchikov, M. A.; Doğan, S.; Avrutin, V.; Cho, S.-J.; Morkoç, H. A comprehensive review of ZnO materials and devices. *J. Appl. Phys.* **2005**, *98*, 041301.
- (19) Li-Li, W.; Xu-Cun, M.; Xi, C.; Qi-Kun, X. Molecular beam epitaxy and superconductivity of stoichiometric FeSe and K<sub>x</sub>Fe<sub>2</sub>-ySe<sub>2</sub> crystalline films. *Chin. Phys. B* **2013**, *22*, 086801.
- (20) Coey, J. M. D.; Venkatesan, M.; Fitzgerald, C. B. Donor impurity band exchange in dilute ferromagnetic oxides. *Nat. Mater.* **2005**, *4*, 173–179.
- (21) Milošev, I.; Strehblow, H.-H.; Navinšek, B. Comparison of TiN, ZrN and CrN hard nitride coatings: Electrochemical and thermal oxidation. *Thin Solid Films* **1997**, *303*, 246–254.
- (22) Miller, E. L.; Rocheleau, R. E. Electrochemical Behavior of Reactively Sputtered Iron-Doped Nickel Oxide. *J. Electrochem. Soc.* **1997**, *144*, 3072–3077.
- (23) Miller, E. L.; Rocheleau, R. E. Electrochemical and Electrochromic Behavior of Reactively Sputtered Nickel Oxide. *J. Electrochem. Soc.* **1997**, *144*, 1995–2003.

- (24) Ait-Djafer, A. Z.; Saoula, N.; Aknouche, H.; Guedouar, B.; Madaoui, N. Deposition and characterization of titanium aluminum nitride coatings prepared by RF magnetron sputtering. *Appl. Surf. Sci.* **2015**, *350*, 6–9.
- (25) Fleischauer, M. D.; Hatchard, T. D.; Rockwell, G. P.; Toppo, J. M.; Trussler, S.; Jericho, S. K.; Jericho, M. H.; Dahn, J. R. Design and Testing of a 64-Channel Combinatorial Electrochemical Cell. *J. Electrochem. Soc.* **2003**, *150*, A1465.
- (26) Hatchard, T. D.; Toppo, J. M.; Fleischauer, M. D.; Dahn, J. R. Electrochemical Performance of SiAlSn Films Prepared by Combinatorial Sputtering. *Electrochem. Solid-State Lett.* **2003**, *6*, A129–A132.
- (27) Guerin, S.; Hayden, B. E.; Lee, C. E.; Mormiche, C.; Owen, J. R.; Russell, A. E.; Theobald, B.; Thompsett, D. Combinatorial Electrochemical Screening of Fuel Cell Electrocatalysts. *J. Comb. Chem.* **2004**, *6*, 149–158.
- (28) Bandarenka, A. S.; Ventosa, E.; Maljusch, A.; Masa, J.; Schuhmann, W. Techniques and methodologies in modern electrocatalysis: evaluation of activity, selectivity and stability of catalytic materials. *Analyst* **2014**, *139*, 1274–1291.
- (29) Rus, E. D.; Wang, H.; Legard, A. E.; Ritzert, N. L.; Dover, R. B. V.; Abruña, H. D. An exchangeable-tip scanning probe instrument for the analysis of combinatorial libraries of electrocatalysts. *Rev. Sci. Instrum.* **2013**, *84*, 024101.
- (30) Cherevko, S.; Keeley, G. P.; Geiger, S.; Zeradjanin, A. R.; Hodnik, N.; Kulyk, N.; Mayrhofer, K. J. J. Dissolution of Platinum in the Operational Range of Fuel Cells. *ChemElectroChem* **2015**, *2*, 1471–1478.
- (31) van der Vliet, D. F.; Wang, C.; Tripkovic, D.; Strmcnik, D.; Zhang, X. F.; Debe, M. K.; Atanasoski, R. T.; Markovic, N. M.; Stamenkovic, V. R. Mesostructured thin films as electrocatalysts with tunable composition and surface morphology. *Nat. Mater.* **2012**, *11*, 1051–1058.
- (32) Deng, C. Z.; Dignam, M. J. Sputtered Cobalt-Carbon-Nitrogen Thin Films as Oxygen Reduction Electrocatalysts I. Physical and Electrochemical Characterization. *J. Electrochem. Soc.* **1998**, *145*, 3507–3512.
- (33) Savadogo, O.; Lee, K.; Oishi, K.; Mitsushima, S.; Kamiya, N.; Ota, K.-I. New palladium alloys catalyst for the oxygen reduction reaction in an acid medium. *Electrochem. Commun.* **2004**, *6*, 105–109.
- (34) Raymunt, A. M.; Bell, R. T.; Thompson, M. O.; Clancy, P. Effect of Laser Annealing on the Structure of Amorphous Porous SiCOH Materials. *J. Phys. Chem. C* **2015**, *119*, 12616–12624.
- (35) Reynolds, M. K.; Paul, D. W. Determination of Diffusion Coefficients through a Polymer Membrane Using a Rotating Disc Electrode. *Meet. Abstr.* **2015**, *MA2015-01*, 2224–2224.
- (36) von Stackelberg, M; Pilgram, M; Toome, W. BESTIMMUNG VON DIFFUSIONSKOEFFIZIENTEN EINIGER IONEN IN WASSRIGER LOSUNG IN GEGENWART VON FREMDELEKTROLYTEN .1. *Eitschrift Für Elektrochem.* **1953**, *57*, 342–350.
- (37) Blizanac, B. B.; Ross, P. N.; Markovic, N. M. Oxygen electroreduction on Ag(1 1 1): The pH effect. *Electrochimica Acta* **2007**, *52*, 2264–2271.
- (38) Jiang, L.; Hsu, A.; Chu, D.; Chen, R. Oxygen Reduction Reaction on Carbon Supported Pt and Pd in Alkaline Solutions. *J. Electrochem. Soc.* **2009**, *156*, B370–B376.
- (39) Stojmenović, M.; Momčilović, M.; Gavrilov, N.; Pašti, I. A.; Mentus, S.; Jokić, B.; Babić, B. Incorporation of Pt, Ru and Pt-Ru nanoparticles into ordered mesoporous carbons for efficient oxygen reduction reaction in alkaline media. *Electrochimica Acta* **2015**, *153*, 130–139.

- (40) An, L.; Zhu, M.; Dai, B.; Yu, F. Hollow palladium–copper bimetallic nanospheres with high oxygen reduction activity. *Electrochimica Acta* **2015**, *176*, 222–229.
- (41) Mayrhofer, K. J. J.; Wiberg, G. K. H.; Arenz, M. Impact of Glass Corrosion on the Electrocatalysis on Pt Electrodes in Alkaline Electrolyte. *J. Electrochem. Soc.* **2008**, *155*, P1–P5.
- (42) Kasatkin, P. E.; Härk, E.; Jäger, R.; Lust, E. Oxygen Reduction Reaction in Alkaline Solution: Influence of Catalyst Loading and Carbon Support Characteristics. *ECS Trans.* **2015**, *64*, 115–123.
- (43) Alexeyeva, N.; Tammeveski, K.; Lopez-Cudero, A.; Solla-Gullón, J.; Feliu, J. M. Electroreduction of oxygen on Pt nanoparticle/carbon nanotube nanocomposites in acid and alkaline solutions. *Electrochimica Acta* **2010**, *55*, 794–803.
- (44) Lee, Y.; Suntivich, J.; May, K. J.; Perry, E. E.; Shao-Horn, Y. Synthesis and Activities of Rutile IrO<sub>2</sub> and RuO<sub>2</sub> Nanoparticles for Oxygen Evolution in Acid and Alkaline Solutions. *J. Phys. Chem. Lett.* **2012**, *3*, 399–404.

## CHAPTER 4

### NEW $\text{Mn}_x\text{Ru}_{1-x}\text{O}_2$ ( $x \leq 0.2$ ), A HIGH PERFORMANCE, LOW COST CATALYST FOR THE OXYGEN REDUCTION AND EVOLUTION REACTIONS

Ryo H. Wakabayashi<sup>#</sup>, Marc J. Murphy<sup>†</sup>, Elliot S. Padget<sup>‡</sup>, David A. Muller<sup>‡</sup>, R. Bruce van  
Dover<sup>†</sup>, Francis J. DiSalvo<sup>#\*</sup>, Héctor D. Abruña<sup>#\*</sup>

<sup>#</sup> Department of Chemistry, Cornell University, Ithaca, New York 14853-1301

<sup>†</sup>Department of Material Science and Engineering, Cornell University, Ithaca, New York  
14853-1301

<sup>‡</sup>School of Applied Engineering and Physics, Cornell University, Ithaca, New York, 14853-  
1301

#### **4.1 Abstract**

We present a new mixed oxide  $\text{Mn}_x\text{Ru}_{1-x}\text{O}_2$  ( $x \leq 0.2$ ), a compound that has not been previously reported.  $\text{Mn}_x\text{Ru}_{1-x}\text{O}_2$  was synthesized using a hydrothermal method, and crystallized in rutile ( $\text{RuO}_2$ ,  $\beta\text{-MnO}_2$ ) structure. This material shows comparable ORR activity to that of Pt and OER activity to that of  $\text{RuO}_2$  in alkaline media, but at a fraction of the cost of Pt. This so-called “bifunctional” catalyst represents an extremely attractive alternative to more expensive cathode catalysts for alkaline fuel cells, or as a cathode catalyst in metal-air batteries.

#### **4.2 Introduction**

Efficient catalysis of the oxygen reduction reaction (ORR) remains elusive to electrochemistry. Even when using a very expensive catalyst such as platinum, the overpotentials required to obtain an operational current density is over  $300 \text{ mV}^{1,2}$ , which represents a voltage loss of 25 % in a hydrogen/oxygen fuel cell (given that  $\text{H}_2 + 2 \text{OH}^- \rightarrow 2 \text{H}_2\text{O} + 2 \text{e}^-$   $E^0 = 0.0 \text{ V}$  vs. RHE and  $\text{O}_2 + 2\text{H}_2\text{O} + 4 \text{e}^- \rightarrow 4 \text{OH}^-$   $E^0 = 1.23 \text{ V}^3$ ). Metal oxides have been studied as possible anode materials since the 1960s<sup>4</sup>, but the usage of oxides in

cathodes in acidic conditions represent a considerably larger challenge, given that many oxides (and non-precious metals in general) passivate, corrode, or dissolve at high potentials in acid. Transitioning to an alkaline fuel cell would mitigate the problem, but as stated in our previous chapter, the development of a good anion exchange membrane has long stood in the way<sup>5</sup>. Now that there are a few reports of what appear to be adequate to excellent anion exchange membranes<sup>6,7,8,9</sup>, we believe that there is a tremendous opportunity to explore non-Pt cathode catalysts in order to lower the cost of the fuel cells, overpotential of the ORR, or, in an ideal scenario, both.

In addition, so-called “bifunctional” catalysts—those that efficiently catalyze both the oxygen reduction reaction (ORR) and the oxygen evolution reaction (OER)—have gained interest as metal-air batteries<sup>10,11</sup> and unitized regenerative fuel cells<sup>12</sup> have become more popular. As if the aforementioned challenges of finding an inexpensive, efficient, and long-lasting catalyst for the ORR were not daunting enough, there are not many catalysts that can do both reactions efficiently and are stable at the high operating potentials of the two reactions. Noble metals like Pt, for example, are expensive but (relatively) good catalysts for the ORR. Pt is, however, not adequate for OER.<sup>13</sup> Oxides represent another category of compounds that can be stable over a wide range of potentials. RuO<sub>2</sub>, for example, is an efficient OER catalyst<sup>14,15</sup>, but is a relatively poor ORR catalyst<sup>13</sup> and therefore a fairly poor “bifunctional” catalyst.

Assuming that catalysis on single-metal oxides is already well-studied, the number of more complex (transition) metal oxides that can be studied are nearly limitless. A simple linear combination of the *3d* metal oxides alone gives us 100 oxides, before accounting for variations in stoichiometric ratios. Clearly, inspiration or hints from past work, or some fundamental, theoretical understanding of catalysis is essential for expedited discovery of new, inexpensive catalysts.

Several classes of oxides have been investigated in recent years, though the requirement for electrical conductivity alone narrows the possible pool of candidates. Among those are spinels<sup>16,17,18,19</sup>, perovskites<sup>20,21,22,23,24,25</sup>, and pyrochlores<sup>26,27,28</sup>. And in the previous chapter we discussed a facile method to electrochemically characterize novel thin film samples using rotating disk electrode voltammetry (RDE) that allows us to quantitatively study a wide range of sputtered thin films. One of the most promising results that came out of the initial screening of complex oxide thin films for their electrocatalytic activity towards the oxygen reduction reaction (ORR) was a sample from a composition spread film of manganese oxide and ruthenium oxide co-sputtered on a ~350 °C substrate. It showed remarkable activity towards both the ORR and the oxygen evolution reaction (OER), an ostensible microscopic reverse of the ORR. Physical characterization (X-ray diffraction, X-ray photoemission spectroscopy) suggested that the active region host a predominantly rutile structure, as do RuO<sub>2</sub> and the β phase of MnO<sub>2</sub>, and contained approximately 12 to 20 % Mn (Ru to balance).

Manganese oxides (of various oxidation states) have been previously reported as catalysts for the ORR in the alkaline media,<sup>29</sup> and mechanistic study has suggested that MnO<sub>x</sub> first reduces oxygen to HO<sub>2</sub><sup>-</sup> (peroxide) and then to water<sup>11</sup>. In addition, it has been reported that the β phase is the most electrocatalytically active form of MnO<sub>2</sub>.<sup>30</sup> The use of manganese oxide (α-Mn<sub>2</sub>O<sub>3</sub>) with potential applications as a “bifunctional” (ORR and OER) catalyst has been reported previously.<sup>13</sup> Some mixed oxides of Mn and other metals have been reported as electrocatalysts as well.<sup>19</sup> For example, it has been reported that doping MnO<sub>2</sub> with Ni and Mg increases the catalytic activity and promotes the 4-electron pathway to water (OH<sup>-</sup> in base) as opposed to the 2-electron pathway to peroxide<sup>31</sup>. Several mixed Co/MnO<sub>x</sub> have also been reported as potential ORR electrocatalysts.<sup>10,16,18,32</sup>

Ruthenium oxide-based materials have also been reported for similar purposes. A mechanistic study on Ru-containing pyrochlore oxides suggested that oxygen first binds on

the hydroxylated surface of the metal oxides<sup>33</sup>. Suppression of the 4-electron pathway by doping with Co or Ni is known<sup>34</sup>. In addition, RuO<sub>2</sub> is known as one of the best OER catalysts in alkaline media<sup>14</sup>, indicating that RuO<sub>2</sub>-based material may also be ideal as “bifunctional” catalysts. There have even been some reports of physical mixtures of MnO<sub>x</sub> and RuO<sub>2</sub> ( $\alpha$ -MnO<sub>2</sub> and RuO<sub>2</sub><sup>35</sup>,  $\gamma$ -MnO<sub>2</sub> and RuO<sub>2</sub><sup>36</sup>). However, to our knowledge, no compound (solid solution or ordered phase) of manganese oxide and ruthenium oxide has ever been reported in the Inorganic Crystal Structure Database or the Phase Equilibria Diagram Online database of the American Ceramic Society/National Institute of Standards and Technology. While this may mean that no solid state chemist was particularly interested in synthesizing a mixture of the two oxides, the more likely interpretation is that there is no stable solid solution or ordered phase that is thermodynamically accessible by standard oxide synthesis at high temperature.

Hints for making this mixed oxide compound may lie in reported syntheses of various polymorphs of MnO<sub>2</sub>, and in particular, the rutile  $\beta$  phase (rutile RuO<sub>2</sub> is the most common form of RuO<sub>2</sub>, and therefore can be synthesized using a wide variety of methods).  $\beta$ -MnO<sub>2</sub> is known to mineralogists as pyrolusite, and is known to occur and form “under highly oxidizing conditions in hydrothermal deposits and rocks”<sup>37</sup>. In fact, most of the reported synthetic procedures of MnO<sub>x</sub> are effectively lab-scale imitations of the formation conditions of pyrolusite. Most of the reported syntheses are hydrothermal methods using a Mn<sup>2+</sup> salt (sulfate, chloride, acetate, etc.) and an oxidizing agent (Na/KMnO<sub>4</sub>, KClO<sub>4</sub>, (NH<sub>4</sub>)<sub>2</sub>S<sub>2</sub>O<sub>8</sub>). For example, Sun et al. and Musil et al. reported on the effects of the manganese counteranion and the oxidizing agent on the crystal structure of the MnO<sub>2</sub> product.<sup>38</sup> Yin et al. reported on the effect of non-Mn cations (K<sup>+</sup> or H<sup>+</sup>) on the structure of the MnO<sub>2</sub> product<sup>40</sup>, and Kuang et al. reported on the effect of the anion on the shape and structure of MnO<sub>2</sub><sup>41</sup>. It is, therefore, sensible to assume that synthetic conditions are extremely critical in obtaining any rutile MnO<sub>2</sub>-containing compound, and that the likeliest method is a hydrothermal method. Taking

these reports into account, synthetic methods to produce a solid solution of rutile  $\text{MnO}_2$  and  $\text{RuO}_2$  have been hereby explored. The synthesized products were examined for electrocatalytic activities for both the ORR and the OER.

### **4.3 Experimental**

#### *4.3.1 Synthesis of the Powder $\text{Mn}_x\text{Ru}_{1-x}\text{O}_2$ ( $x \leq 0.2$ )*

Stoichiometric amounts of  $\text{RuCl}_3 \cdot 3\text{H}_2\text{O}$  (typically 62.7 mg) and  $\text{MnSO}_4$  (typically 8.68 mg) were mixed in approximately 5 mL of water, and stirred for approx. 30m.  $\text{KMnO}_4$  (0.6 mL of 4 mM aqueous solution) was then added (mol ratio  $\text{MnSO}_4 : \text{KMnO}_4 = 3 : 2$ ) and stirred for approx. 10 minutes, by which time a brown solid had precipitated. The suspension was transferred to a Teflon bomb autoclave (20 mL) and was heated at 160 °C for 6 hours. The black precipitate was filtered and washed with copious amounts of water, and was subsequently annealed in air at 450 °C for 6 hours.

As a comparison, the same procedure was performed with each of the reactants to obtain a pure manganese oxide ( $\beta\text{-MnO}_2$ ) or a pure ruthenium oxide ( $\text{RuO}_2$ ).  $\alpha\text{-Mn}_2\text{O}_3$  was synthesized by first dissolving approx. 900 mg of  $\text{Mn}(\text{NO}_3)_2 \cdot 3\text{H}_2\text{O}$  in water, and then precipitating a brown solid by adding  $\text{NH}_4\text{OH}$  (1.5 M) to make the pH = 8. The suspension was filtered and washed with water, dried at 80 °C, then finally heating in air at 550 °C for 12 hours, following a literature procedure.<sup>42</sup>

The products were then mixed with carbon black (Vulcan XC-72R, pre-heated to 400 °C for 12 h in air to oxidize the surface for better dispersion in polar solvents) using a Pulverisette 7 (Frisch) planetary mill. In order to ensure that the catalysts were not contaminated with electrochemically active materials in the planetary mill, carbon black was milled by itself to be electrochemically tested, as well. Physical mixtures of  $\text{MnO}_2$ ,  $\text{Mn}_2\text{O}_3$ , and/or  $\text{RuO}_2$  with carbon black (2:8 Mn:Ru metal ratio, 40 % wt. loading on C) were also made by using a Pulverisette 7.

#### 4.3.2 *Physical Characterization* (EELS performed and written partly written by Elliot Padgett)

X-ray diffraction was performed using a Rigaku Ultima IV using Cu K $_{\alpha}$  ( $\lambda=1.5406$  Å for K $_{\alpha 1}$ , 1.5444 Å for K $_{\alpha 2}$ ). Refinement was done using PDXL (Rigaku) software. Scanning electron microscopy (SEM) images and energy-dispersive X-ray spectroscopy (EDX) were taken using a LEO KECK FESEM. High-resolution scanning transmission electron microscope (STEM) images and electron energy loss spectroscopy (EELS) data were taken using a NION UltraSTEM 1000 microscope.

Scanning transmission electron microscope (STEM) images and electron energy loss spectroscopy (EELS) maps were acquired using a NION UltraSTEM, a fifth-order aberration corrected microscope. It was operated with a 100 kV accelerating voltage and a 30 mrad convergence angle, which provided a beam current of approx. 70 pA in an angstrom-sized probe. EELS maps were acquired with a fast 5 ms dwell time in pixels at 5 angstrom spacing, so as to minimize beam-induced damages. Spectra were subsequently de-noised using principal component analysis (PCA). EELS maps were reconstructed using the first 7 principal components (PCA), which accounted for 98% of the data variance and all visible systematic spatial variation. After noise removal, composition maps were produced from the integrated signal of the oxygen K-edge, the ruthenium M $_3$ -edge, and the manganese L $_3$  edge after background subtraction using a linear combination of power laws fit. Background subtraction and integration was performed using the Cornell Spectrum Imager plugin for ImageJ.<sup>43</sup>

#### 4.3.3 *Electrochemical Characterization*

Glassy carbon (5 mm diameter) electrodes were polished using 1  $\mu$ m diamond polishing paste (Buehler) followed by 0.3 and 0.05  $\mu$ m alumina powder (Extec and Buehler), and were rinsed using Millipore water (18M $\Omega$ /cm Thermo Scientific Barnstead Nanopure). These electrodes were then sonicated in 0.1M NaOH (Malinckrodt AR) for 5 minutes to activate the surface prior to deposition of the sample inks.

The inks for electrochemical characterization were made using Nafion (0.02 wt. % in 200 proof ethanol), or in some cases, a previously published alkaline anion exchange ionomer<sup>6</sup> (0.02 wt. % in 200 proof ethanol). As long as there is no carbon in the formation, the choice of ionomer seems to have little to no effect in the electrochemical performance, perhaps due to the fact that the loading of the ionomers is incredibly low. However, the phosphonium anion exchange ionomer was not a suitable binder for samples with carbon black, however, since carbon aggregated in the presence of the phosphonium ionomer. This may be due to the fact that the ionomer was originally dissolved in n-propanol. 80  $\mu\text{g}/\text{cm}^2$  of the oxide were deposited on a glassy carbon electrode ( $d = 5 \text{ mm}$ ). A home-made Ag/AgCl was used as the reference electrode, and a graphite rod was used as the counter electrode (so as to have no metal contamination).

Cyclic voltammetry (CV) and rotating disk electrode voltammetry (RDE) were performed using Bioanalytical Systems CV-27 potentiostat, at a scan rate of 20 mV/s, except for the oxygen evolution reaction (OER) which was done at 2 mV/s. 0.1 M NaOH (Malinkrodt AR) aqueous solution (made using Nanopure water) was used as the electrolyte in all experiments. For the oxygen reduction reaction, the solution was initially deoxygenated by bubbling  $\text{N}_2$  (Airgas, UHP) to take a CV, and then the solution was saturated with  $\text{O}_2$  (Airgas, UHP) by bubbling for 15 minutes initially and for 7 minutes after every scan to ensure that the solution remained saturated with oxygen for each scan. ORR on Pt/C was performed in a separate electrochemical cell and a Pt wire as counter electrode, in order to avoid metal contaminations in the electrochemical experiments of the oxide samples.

Some data were averaged using the Savitzky-Goley method (9 points) to remove periodic noise.

#### ***4.4 Results and Discussions***

Figure 4.1 shows the powder XRD patterns of  $\text{Mn}_{0.2}\text{Ru}_{0.8}\text{O}_2$  (red),  $\text{RuO}_2$  (blue), and  $\beta\text{-MnO}_2$  (orange), all synthesized using identical methods.  $\text{Mn}_{0.2}\text{Ru}_{0.8}\text{O}_2$  appears (at least above the limit of detection of pXRD) to be a single-phased product. Inspection of the spectra shows that peaks corresponding to lattice planes (hkl) with  $l \neq 0$  show a small shift to higher angles, indicating a decrease in “c”; given that  $\text{RuO}_2$  and  $\text{MnO}_2$  have a similar a axis but a considerably different c axis ( $\text{RuO}_2$ :  $a = 4.50 \text{ \AA}$ ,  $c = 3.11 \text{ \AA}$ ;  $\text{MnO}_2$ :  $a = 4.40 \text{ \AA}$ ,  $c = 2.89 \text{ \AA}$ ). However, the changes in both a and c were not as much as Vegard’s Law would predict (See Figure 4.2). Applying the Scherrer equation to the (101) peak, the crystallite domain size was estimated to be 5 nm. EDX results (Table 4.1) indicate that the ratio of Mn to Ru is 15.0:85.0, which is within the experimental error of the desired 1:4 (resolution of EDX for non-ideal samples such as small particles is limited).

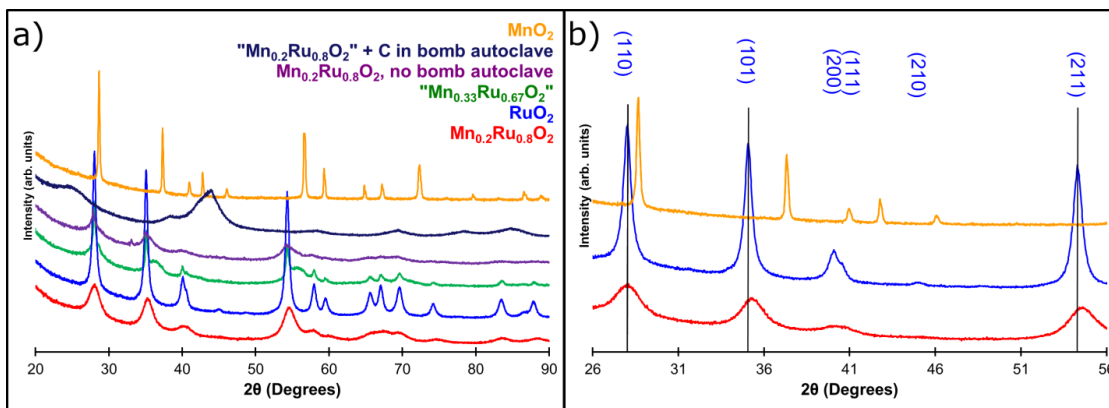


**Figure 4.1.** (a) X-ray diffraction patterns of  $\text{Mn}_{0.2}\text{Ru}_{0.8}\text{O}_2$  (red),  $\text{RuO}_2$  (blue),  $\text{Mn}_{0.33}\text{Ru}_{0.67}\text{O}_2$  (green), of  $\text{Mn}_{0.2}\text{Ru}_{0.8}\text{O}_2$  heated at 160 °C in ambient air (purple),  $\text{Mn}_{0.2}\text{Ru}_{0.8}\text{O}_2$  made with carbon black in the bomb autoclave (navy), and  $\beta\text{-MnO}_2$  (orange). (b): zoom of the first three major peaks of  $\text{Mn}_{0.2}\text{Ru}_{0.8}\text{O}_2$  (red),  $\text{RuO}_2$  (blue), and  $\beta\text{-MnO}_2$  (orange). with labels of lattice planes for  $\text{RuO}_2$  peaks and black lines drawn at peak locations of  $\text{RuO}_2$ . Peaks of  $\text{Mn}_{0.2}\text{Ru}_{0.8}\text{O}_2$  are slightly shifted from  $\text{RuO}_2$ , especially the peaks with lattice planes that do not contain a z component, indicating some lattice constant change.

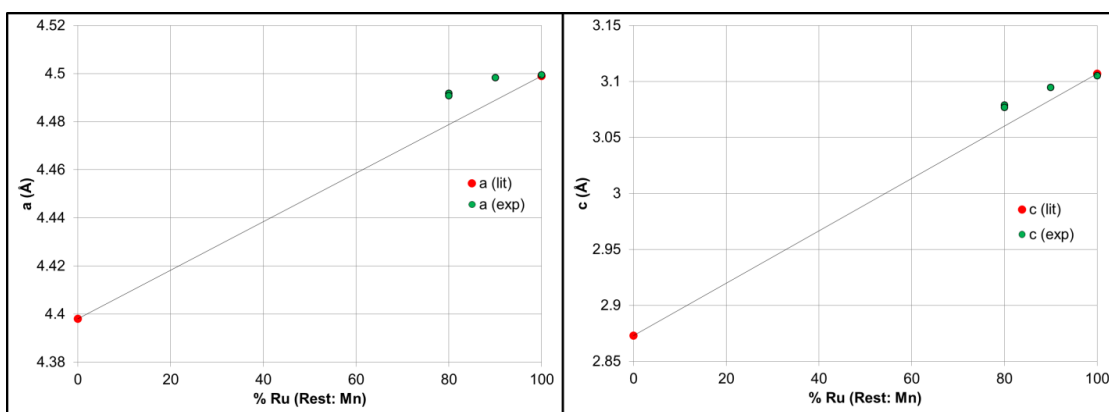


**Figure 4.2.** Lattice constants ( $a$  on left,  $c$  on right) of the rutile structure products as a function of % Ru. Red dots are literature values of  $\beta\text{-MnO}_2$  and  $\text{RuO}_2$ .

The solubility of Mn in RuO<sub>2</sub> seem to be limited, however, as “Mn<sub>0.33</sub>Ru<sub>0.67</sub>O<sub>2</sub>” clearly shows a presence of another phase of MnO<sub>2</sub> ( $\epsilon$  phase) (Figure 4.1 (a), green) in addition to the peaks corresponding to the rutile structure. As was the case for the synthesis of  $\beta$ -MnO<sub>2</sub>, the high-pressure vessel (bomb autoclave) seems to play a critical role in the synthesis. A phase diagram (Phase Diagram for Ceramicists<sup>44</sup>) also predicts that MnO<sub>2</sub> would decompose to Mn<sub>2</sub>O<sub>3</sub> and O<sub>2</sub> at moderately high temperature (~400 °C) at atmospheric oxygen partial pressure (or lower), but as shown in Figure 4.1(a) (orange), the MnO<sub>2</sub> sample annealed at 450 °C was in  $\beta$  phase, and no Mn<sub>2</sub>O<sub>3</sub> peaks are observed in Mn<sub>0.2</sub>Ru<sub>0.8</sub>O<sub>2</sub> or  $\beta$ -MnO<sub>2</sub> samples. Another database (International Programme on Chemical Safety<sup>45</sup>) suggest, however, that the decomposition of MnO<sub>2</sub> happens at 553 °C, which is in line with the result shown here.

Heating the initial suspension in ambient air instead of a bomb autoclave (Figure 4.1 (a), purple) yields a second phase ( $\alpha$ -Mn<sub>2</sub>O<sub>3</sub>). This process sometimes yields XRD patterns without any clear signs of second phase, but the peaks look generally less crystalline and appear less Gaussian (Figure 4.3). This likely indicates that the domain size is far less uniform when a high-pressure heating process is not employed. In addition, from EDX, the distribution of metals appears to be less uniform in the samples heated in air (much bigger standard deviation in Table 4.1), as opposed to the one heated in autoclave. They also contain some K and S impurities, likely from KMnO<sub>4</sub> and MnSO<sub>4</sub>, respectively (see Table 4.1).

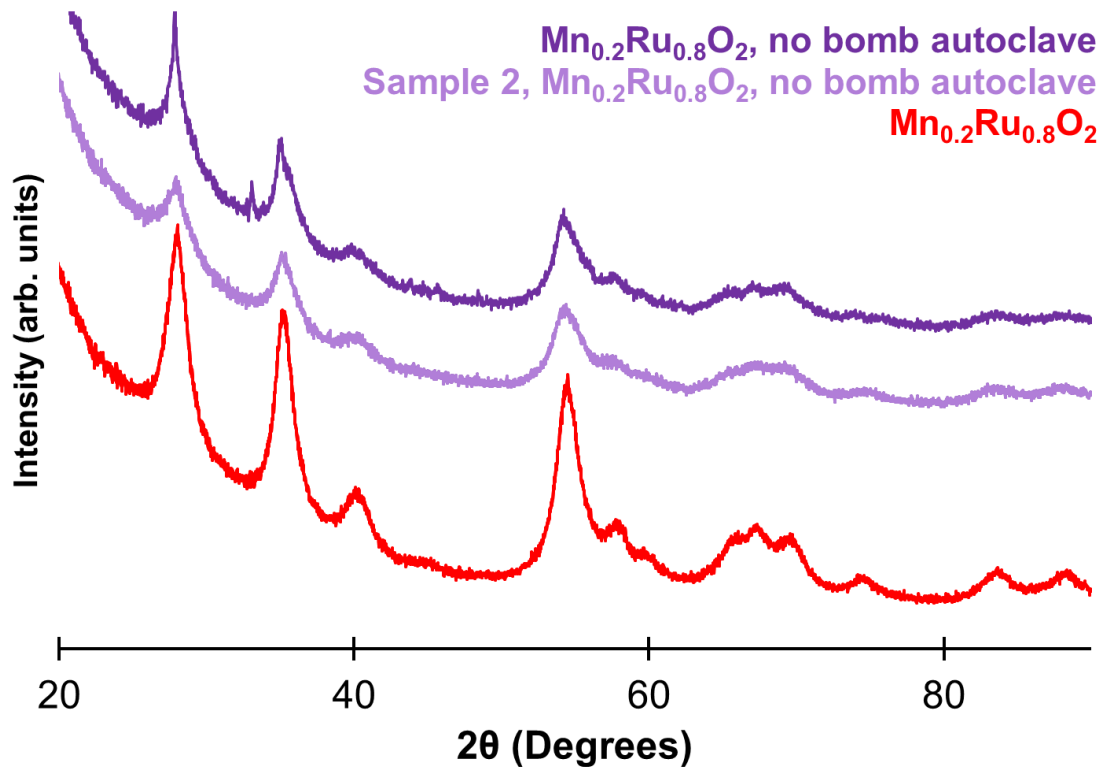


**Figure 4.3.** X-ray diffraction patterns of  $\text{Mn}_{0.2}\text{Ru}_{0.8}\text{O}_2$  (red), another sample of  $\text{Mn}_{0.2}\text{Ru}_{0.8}\text{O}_2$  heated at 160 °C in ambient air (light purple), and  $\text{Mn}_{0.2}\text{Ru}_{0.8}\text{O}_2$  heated at 160 °C in ambient air (darker purple). Darker purple and red traces are replicated from Figure 4.1.

	Mn (%)	Ru (%)	S (%)	K (%)
Using Autoclave (similar to red in Fig 2.3)	15.0 ± 0.7	85.0 ± 0.7	---	---
No Autoclave (light purple in Fig 2.3)	11.2 ± 4.0	82.0 ± 6.3	5.1 ± 1.8	1.7 ± 1.3

**Table 4.1.** EDX results of  $\text{Mn}_{0.2}\text{Ru}_{0.8}\text{O}_2$  made with and without using the bomb autoclave.

Standard deviation calculated from at least 8 measurements.

Figure 4.4 (a, b) shows SEM images of  $\text{Mn}_{0.2}\text{Ru}_{0.8}\text{O}_2$ . They appear to be uniform with a primary particle size of around 200 nm. Given that XRD analysis yields a primary domain size of 5 nm, it is clear that particles consist of agglomerated nanoparticle clusters, which is not surprising given the absence of surfactants or catalyst support (carbon, etc.) in the synthesis. We attempted to pre-mix Vulcan XC72R in the suspension prior to heating in bomb autoclave, but it resulted in reduction of ruthenium to metallic ruthenium (Figure 4.1(a), navy trace). The  $\text{Mn}_{0.2}\text{Ru}_{0.8}\text{O}_2$  particles also have a rough morphology with what appears to be very small particles sprinkled on larger spheres. It is also important to note that the image looks single-phase; pure  $\text{MnO}_2$  made under the identical synthetic condition yields rod-like morphologies (Figure 4.3(d)), which are entirely absent in  $\text{Mn}_{0.2}\text{Ru}_{0.8}\text{O}_2$ . Images of  $\text{RuO}_2$  (Figure 4.4(c)) to the first order, look like  $\text{Mn}_{0.2}\text{Ru}_{0.8}\text{O}_2$  but considerably bigger, which is consistent with the XRD peak widths. Some images of  $\text{Mn}_{0.2}\text{Ru}_{0.8}\text{O}_2$  even show an empty core, though we were unable to determine if such is the case for all or majority of the particles. The sample made in ambient air (Figure 4.4(d) clearly shows multiple morphologies and different appearance (more needle-like features in the spherical components). This further suggests that, even if the XRD does not show clear peaks from impurity phases, heating in ambient air instead of the bomb autoclave yields a multi-phase product.

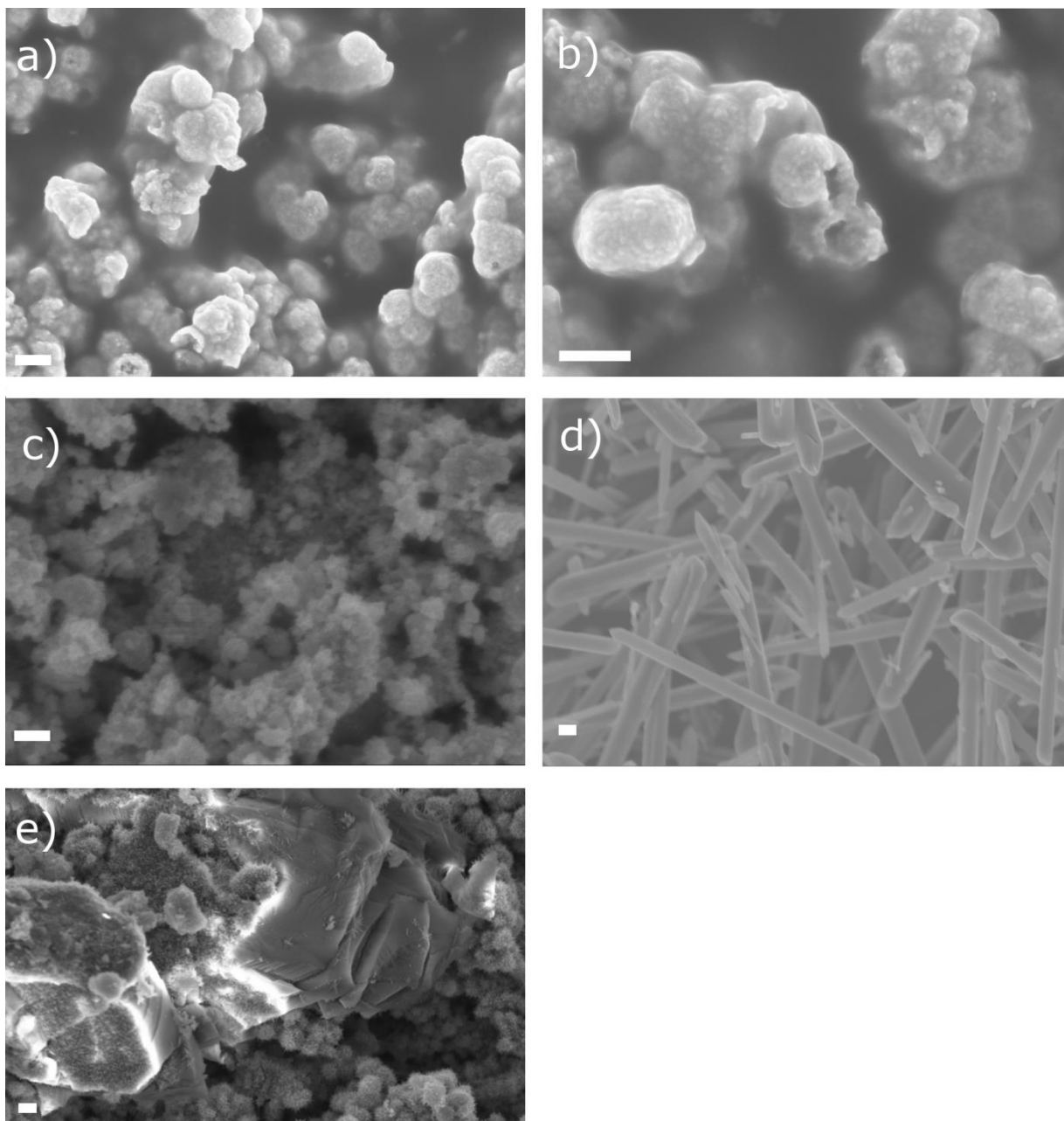


**Figure 4.4.** SEM images of  $\text{Mn}_{0.2}\text{Ru}_{0.8}\text{O}_2$  (a and b),  $\text{RuO}_2$  (c),  $\text{MnO}_2$  (d), and  $\text{Mn}_{0.2}\text{Ru}_{0.8}\text{O}_2$  made without using a bomb autoclave (e). Scale bars are 200 nm.

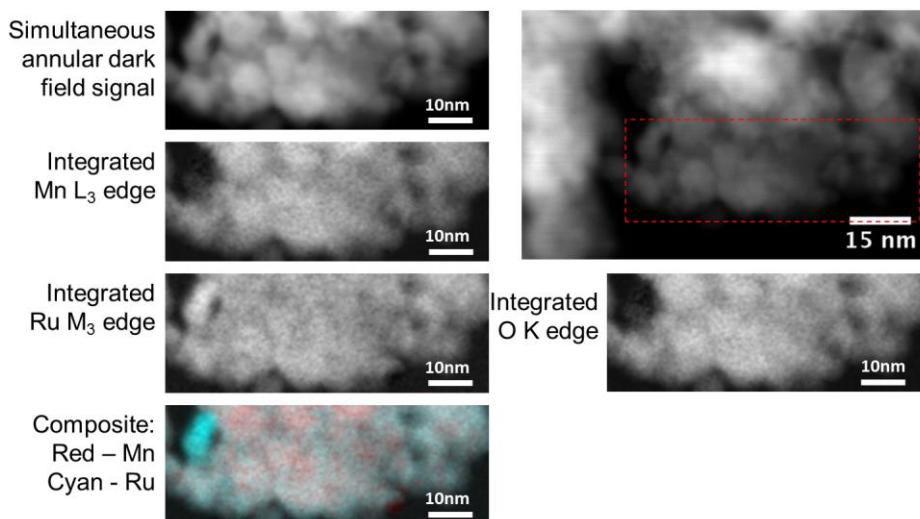


**Figure 4.5.** High-resolution EELS image of  $\text{Mn}_{0.2}\text{Ru}_{0.8}\text{O}_2$ , after removing noise by principal component analysis. Region in red dotted box on the top right was mapped. Mn is red and Ru is cyan in the bottom left (Image by Elliot Padget)

High-resolution EELS (performed by Padget) map largely shows a uniform mixture of Mn and Ru (Figure 4.5). However, it must be noted that phase segregation induced by a high beam current is entirely possible<sup>46,47</sup>. There is a region in the top left corner of the aggregate map that is purely cyan (Ru) and shows no O content, indicating a presence of metallic Ru. It is highly likely that metallic Ru was synthesized, given the oxidizing condition of the synthesis. Therefore, the presence of metallic Ru is likely due to beam damage. We also observed clear phase segregation with higher beam current (approx. 140 pA). Still, Mn and Ru oxides appear to be mixed at atomic scale, indicating a very intimate mixture.

Figure 4.6 shows the RDE voltammograms of  $\text{Mn}_{0.2}\text{Ru}_{0.8}\text{O}_2/\text{C}$   $\text{O}_2$ -saturated 0.1 M NaOH. The slopes of the kinetic region of the RDE voltammograms are as steep as that of the Pt/C sample (see Figure 4.7); half-wave potential ( $E_{1/2}$ ) taken from voltammogram of 1600 rpms are approximately -0.139 V vs. Ag/AgCl for Pt/C and approximately -0.185 V vs. Ag/AgCl for  $\text{Mn}_{0.2}\text{Ru}_{0.8}\text{O}_2$ , meaning that  $\text{Mn}_{0.2}\text{Ru}_{0.8}\text{O}_2$  requires only 46 mV more of an overpotential to reach the same current density in the kinetic region compared to Pt, which is

superior to any of the  $\text{MnO}_x$  or  $\text{RuO}_2$ -based materials discussed in the previous paragraph.<sup>10,11,13,16,18,30,32</sup> This is a remarkable activity, given that  $\text{Mn}_{0.2}\text{Ru}_{0.8}\text{O}_2$  would be nearly 40 times less expensive than platinum per mass (According to [www.infomine.com](http://www.infomine.com) on 3/23/2016, Pt is USD 956.35/OZT, while Ru is USD 42.00/OZT and Mn is USD 1.63/kg, or USD 0.051/OZT, so  $\text{Mn}_{0.2}\text{Ru}_{0.8}\text{O}_2$  is 28.5 times less expensive than Pt per mass of metals, or accounting for the mass of oxygen in the active material is 38.6 times less expensive than Pt per mass).

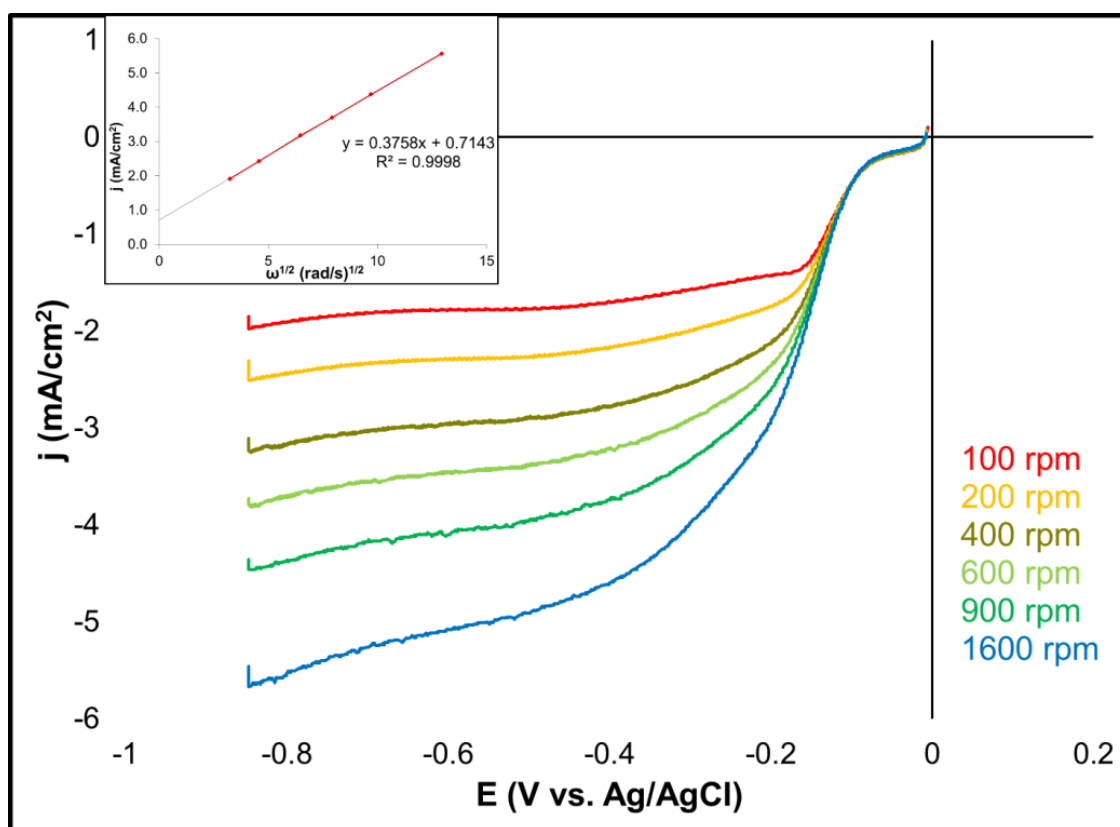


**Figure 4.6.** RDE voltammograms of  $\text{Mn}_{0.2}\text{Ru}_{0.8}\text{O}_2/\text{C}$  in  $\text{O}_2$ -saturated 0.1 M NaOH. Inset: Levich plot from current densities at -0.8 V vs. Ag/AgCl.

Applying the Levich equation at -0.8 V yields a very good linear fit ( $r^2 = 0.9998$ , Figure 4.5 inset), indicating an ideal mass transport limit behavior with no kinetic limitation even at high mass transport, and an electron count number  $n = 3.25$  (diffusion coefficient of

O<sub>2</sub> in water  $D = 1.93 \times 10^{-5} \text{ cm}^2/\text{s}$ ,  $C_0 = 1.26 \times 10^{-3} \text{ M O}_2$  at saturation, and kinematic viscosity  $\nu = 1.07 \times 10^{-2} \text{ cm}^2/\text{s}$ , from Markovic et al.<sup>48</sup>). Given that the ORR on Pt in the alkaline media does not proceed entirely either<sup>49</sup>, we do not expect this to be a significant drawback of this catalyst. The ORR was also performed using pure RuO<sub>2</sub>/C and  $\beta$ -MnO<sub>2</sub>/C, and a metacomparison of the RDE voltammograms (at 1600 rpm) of those samples, as well as Pt/C and thin film sample of Mn<sub>0.2</sub>Ru<sub>0.8</sub>O<sub>2</sub> (Chapter 3) are shown in Figure 4.7. It is evident that Mn<sub>0.2</sub>Ru<sub>0.8</sub>O<sub>2</sub> is a superior ORR catalyst when compared to RuO<sub>2</sub> or  $\beta$ -MnO<sub>2</sub>. The catalytic activity of Mn<sub>0.2</sub>Ru<sub>0.8</sub>O<sub>2</sub> is nearly identical to the thin film of the same composition, indicating that results from a thin film with a compositional spread can be translated into powder form, even if the phase is previously unreported as discussed above.

It is notable, however, that the phase-impure product shows identical activity (purple line of Figure 4.6, corresponding to purple trace in Figure 4.1(a) and 4.3) as the phase-pure sample. This indicates, perhaps, that the requirement for a good catalytic activity is merely the proximity of small domains of manganese oxides near a conductive “backbone” (RuO<sub>2</sub> in this work). The physical mixture of MnO<sub>2</sub> with RuO<sub>2</sub>, and the mixture of Mn<sub>2</sub>O<sub>3</sub> with RuO<sub>2</sub>, both show comparable onset potential but considerably worse kinetics than the chemically mixed (or at least partially mixed, as is the case with the purple line).  $E_{1/2}$  of the single-phase Mn<sub>0.2</sub>Ru<sub>0.8</sub>O<sub>2</sub> is -0.18 V vs. Ag/AgCl, compared to -0.16 V vs. Ag/AgCl for the segregated Mn<sub>0.2</sub>Ru<sub>0.8</sub>O<sub>2</sub>, -0.20 V vs. Ag/AgCl for the MnO<sub>2</sub>/RuO<sub>2</sub> physical mixture, and -0.22 V vs. Ag/AgCl for Mn<sub>2</sub>O<sub>3</sub>/RuO<sub>2</sub> physical mixture. The limit of small domains being well-dispersed on a conductive matrix would be the alloy, which may explain the high activity of the samples presented here compared to other works presented in the literature.<sup>35,36</sup>

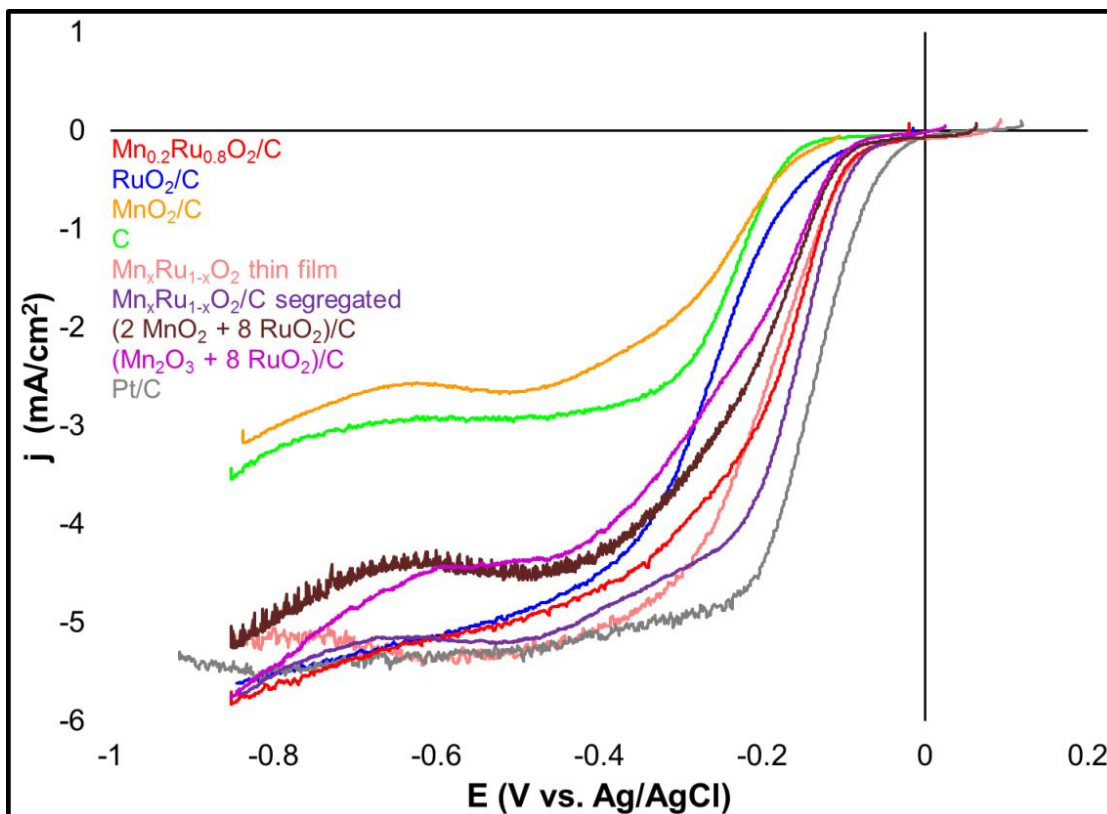


**Figure 4.7.** RDE voltammograms (1600 rpm) of  $\text{Mn}_{0.2}\text{Ru}_{0.8}\text{O}_2/\text{C}$  (red),  $\text{RuO}_2/\text{C}$  (blue), and  $\beta\text{-MnO}_2/\text{C}$  (yellow), carbon black (green),  $\text{Mn}_{0.2}\text{Ru}_{0.8}\text{O}_2$  “E8” thin film (pink, by Murphy in Ch. 3), phase-segregated “ $\text{Mn}_{0.2}\text{Ru}_{0.8}\text{O}_2$ ”/C (purple), physical mixture of  $\text{MnO}_2/\text{RuO}_2/\text{C}$  (2:8 Mn:Ru metal basis, brown), physical mixture of  $\text{Mn}_2\text{O}_3/\text{RuO}_2/\text{C}$  (2:8 Mn:Ru metal basis, magenta), and Pt/C (gray) in  $\text{O}_2$ -saturated 0.1 M NaOH.

From Figure 4.7, it is clear that  $\text{Mn}_{0.2}\text{Ru}_{0.8}\text{O}_2$  is a better catalyst than the sum of its parts (though this statement is somewhat complicated, because it was not possible to make a smooth, well-dispersed  $\text{MnO}_2/\text{C}$  ink with Nafion or the phosphonium ionomer, for an unknown reason). While somewhat speculative on our part, we suspect that manganese and ruthenium oxides interact with each other favorably. Mao et al. reported that the ORR in alkaline media on  $\text{MnO}_2$  electrodes first undergoes a 2-electron reduction to  $\text{HO}_2^-$ , but that  $\text{MnO}_2$  also catalyzes the disproportionation of  $2 \text{HO}_2^-$  to  $\text{O}_2$  (and  $2 \text{OH}^-$ )<sup>11</sup>. It may also be a Mn

redox-mediated process, as described by Cheng et al., where  $\text{MnO}_2$  is first reduced to  $\text{MnOOH}$ , and  $\text{O}_2$  adsorbs either on 2 sites ( $\text{O}_2$  sideways) or single site ( $\text{O}_2$  vertical) to yield a mixture of 2 and 4 electron processes, giving it an average of approximately 3 electrons<sup>30</sup>, which is consistent with what we observe. In addition, Anastasijevic et al. reported that, on Ru (technically  $\text{RuO}_x$ , because Ru surfaces oxidize in alkaline media) the reaction undergoes a 4-electron reduction of  $\text{O}_2$  to  $\text{OH}^-$  at high overpotentials but also undergo a 2-electron reduction to  $\text{HO}_2^-$  at lower overpotentials. Therefore, it is entirely possible that  $\text{HO}_2^-$  produced by Ru (and Mn) sites are disproportionated back to  $\text{O}_2$ , which is then reduced again at higher overpotential. However, there is no strong evidence of such reaction in the rotation rate-normalized voltammograms (Figure 4.8) but instead looks “CE” (onset potential largely the same, but normalized limiting currents different because at lower rotation rates there is more time for the “C” process to happen). This may be because the product is carried away from the electrode much faster than the kinetics of disproportionation. If Mn does indeed catalyze the disproportionation, though, the benefit of this reaction pathway is that  $\text{HO}_2^-$ , a reactive anion that may damage the carbon support and/or the polymer membrane, is consumed right away.

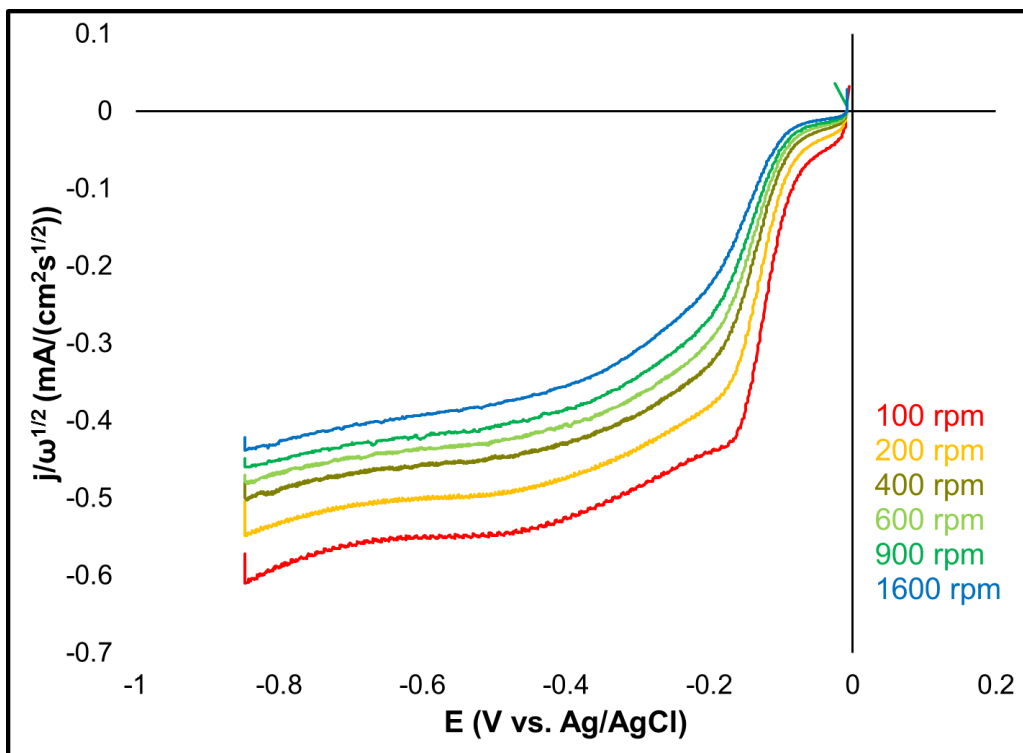


**Figure 4.8.** Rotation-rate normalized RDE voltammograms of  $\text{Mn}_{0.2}\text{Ru}_{0.8}\text{O}_2$  in  $\text{O}_2$ -saturated 0.1 M NaOH.

Figure 4.9(a) shows RDE voltammograms of  $\text{Mn}_{0.2}\text{Ru}_{0.8}\text{O}_2/\text{C}$  (40 wt. %) loaded on the glassy carbon electrode at  $80 \mu\text{g}/\text{cm}^2$ . The ORR measurements were taken again after 24 hours of continuous cyclic voltammetry at  $20 \text{ mV}/\text{s}$  (= approx. 2000 cycles). There is a slight decrease in the slope of the kinetic region, possibly indicating corrosion, passivation and/or particle loss. We suspect that it is some combination of the three. The Pourbaix diagram<sup>3</sup> suggests that Mn can dissolve at high potentials (ca. 1 V vs. RHE) in aqueous solution at  $\text{pH} = 13$ , though we had set the potential limit at 0 V vs. Ag/AgCl (=0.96 V vs. RHE). Particle loss is a strong possibility. Without carbon (Figure 4.9(b)), the RDE voltammograms show even shallower slopes after 24 hours despite higher active material loading ( $100 \mu\text{g}/\text{cm}^2$ ), indicating that the addition of carbon, a high surface area support, was helpful in keeping the active material on the electrode.

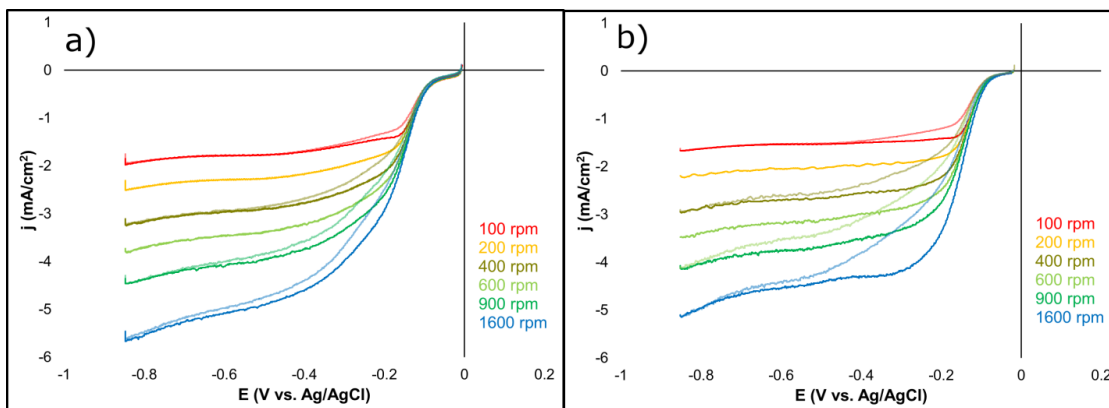


**Figure 4.9.** RDE voltammogram of  $\text{Mn}_{0.2}\text{Ru}_{0.8}\text{O}_2/\text{C}$  (a; partial reproduction of previous figure) and of  $\text{Mn}_{0.2}\text{Ru}_{0.8}\text{O}_2$  without C (b), at 0 h and after 2000 CVs (lighter shade).

The OER, ostensibly a microscopic reverse reaction of the ORR, was also investigated. Figure 4.10 shows linear sweep voltammograms in  $\text{O}_2$ -saturated 0.1 M NaOH.  $\text{RuO}_2$  is one of the best OER catalysts known in the alkaline media<sup>4,14</sup>, but  $\text{Mn}_{0.2}\text{Ru}_{0.8}\text{O}_2/\text{C}$  shows slightly better kinetics than  $\text{RuO}_2$  (Tafel slopes: 111 mV/decade vs. 123 mV/decade—see Figure 4.11). The thin film sample has a more positive onset potential than the powder equivalent, but shows slightly better kinetics (78.7 mV/decade). Lower active surface area may be the reason for a slightly worse onset potential. On the other hand, inferior Tafel slope of the powder  $\text{Mn}_{0.2}\text{Ru}_{0.8}\text{O}_2/\text{C}$  compared to the thin film sample suggests that there may be some ohmic loss in the powder samples. Perhaps loading on the carbon could be optimized further.

The phase-impure sample (purple line) shows identical activity to the single-phase  $\text{Mn}_{0.2}\text{Ru}_{0.8}\text{O}_2$ , again indicating that a single-phase product is not necessary for the high activity. The physically mixed samples of  $\text{MnO}_2/\text{RuO}_2$  and  $\text{Mn}_2\text{O}_3/\text{RuO}_2$  both show inferior activity to the two “chemically mixed” samples and even the pure  $\text{RuO}_2$ . This may indicate that, what is necessary may simply be a near-atomic scale contact of manganese and ruthenium oxides, just like it was shown in the ORR (Figure 4.7). The fact that pure  $\text{RuO}_2$  shows better kinetics than the physically mixed samples may indicate that the OER activity of all of these samples

may be dominated by the  $\text{RuO}_2$  domains, and that physically mixed samples block  $\text{RuO}_2$  sites by covering over them with the manganese oxide particles.

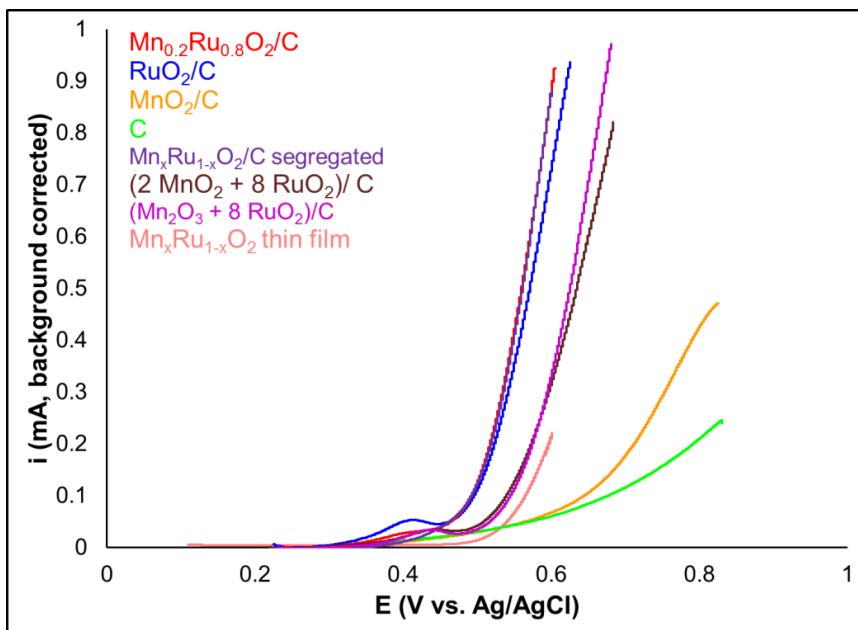


**Figure 4.10.** Linear sweep voltammograms in  $\text{O}_2$ -saturated 0.1 M NaOH, investigating the OER, of  $\text{Mn}_{0.2}\text{Ru}_{0.8}\text{O}_2/\text{C}$  (red),  $\text{RuO}_2$  (blue), and  $\beta\text{-MnO}_2$  (yellow), carbon black (green),  $\text{Mn}_{0.2}\text{Ru}_{0.8}\text{O}_2$  “E8” thin film (magenta), phase-segregated “ $\text{Mn}_{0.2}\text{Ru}_{0.8}\text{O}_2$ ”/C (purple), physical mixture of  $\text{MnO}_2/\text{RuO}_2/\text{C}$  (2:8 Mn:Ru metal basis, brown), and physical mixture of  $\text{Mn}_2\text{O}_3/\text{RuO}_2/\text{C}$  (2:8 Mn:Ru metal basis, magenta) in  $\text{O}_2$ -saturated 0.1 M NaOH.

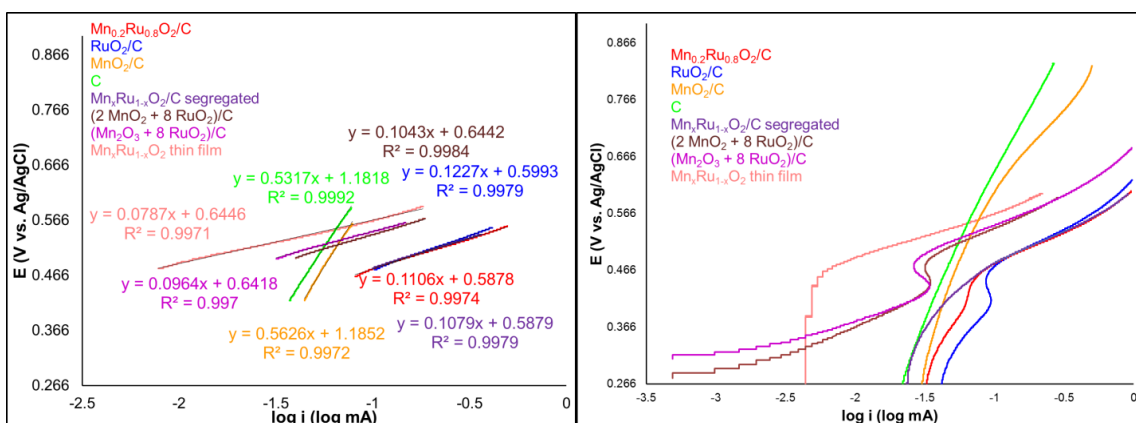


**Figure 4.11.** (a) Linear region used to calculate the Tafel slope, and their values. Purple line is on top of the red line. (b) Tafel plot.

#### **4.5 Conclusions**

A previously unreported solid solutions of rutile  $\beta$ - $\text{MnO}_2$  with rutile  $\text{RuO}_2$  ( $\text{Mn}_x\text{Ru}_{1-x}\text{O}_2$ ), albeit over a limited solubility window, ( $x \leq 0.2$ ), have been synthesized. The products, made using a high-pressure, liquid-phase (hydrothermal) synthesis method, appear single-phase within the resolution of X-ray diffraction. The rutile  $\text{Mn}_{0.2}\text{Ru}_{0.8}\text{O}_2$ , especially when mixed with carbon, showed comparable ORR kinetics to Pt in alkaline media, a remarkable observation for a non-noble metal catalyst that would be over 30 times less expensive than Pt by mass. In addition, it has superior oxygen evolution activity to  $\text{RuO}_2$ , one of the best OER catalysts in alkaline media. It was also shown, however, that strictly for high catalytic activity, phase purity is not essential.  $\text{Mn}_x\text{Ru}_{1-x}\text{O}_2$  reported in this article is a promising candidate as catalyst material for cathodes in alkaline fuel cells, rechargeable metal-air batteries, and other similar systems.

#### **4.6 Future Directions**

It is entirely possible that small domains of  $\text{MnO}_2$  are mainly responsible for the catalysis (of ORR) at low overpotentials, and simply needs to be on a conductive matrix. Or, it could be that the rutile template ( $\text{RuO}_2$ ) is critical for the electrochemical behavior of  $\text{MnO}_2$ . If this hypothesis is correct, then  $\text{CrO}_2$ , a rutile oxide with a “half-metallic” conductivity and similar lattice constant as  $\text{MnO}_2$  ( $\beta$ - $\text{MnO}_2$ :  $a = 4.40 \text{ \AA}$ ,  $c = 2.89 \text{ \AA}$ ;  $\text{CrO}_2$ :  $a = 4.42 \text{ \AA}$ ,  $c = 2.92 \text{ \AA}$ )<sup>50</sup>, may be an interesting, even less expensive replacement for ruthenium.  $\text{CrO}_2$ , like  $\beta$ - $\text{MnO}_2$ , can be prepared in a bomb autoclave, specifically, via a decomposition of  $\text{CrO}_3$ , a strong oxidant.<sup>51</sup> Therefore, perhaps replacing  $\text{KMnO}_4$  and  $\text{RuCl}_3$  with  $\text{CrO}_3$  in the synthesis may be a good starting point.

#### **4.7 Acknowledgments**

This work is based upon work supported as part of the Energy Materials Center at Cornell (EMC<sup>2</sup>), an Energy Frontier Research Center funded by the U.S. Department of

Energy, Office of Science, and Office of Basic Energy Sciences under Award Number DE-SC0001086. This work was also supported by Cornell University from September 2014 through June 2016. This work made use of the Cornell Center for Materials Research Shared Facilities which are supported through the NSF MRSEC program (DMR-1120296). The author would like to thank John Grazul and Mick Thomas for their help with TEM.

## REFERENCES

- (1) Yeager, E. Electrocatalysts for O<sub>2</sub> reduction. *Electrochimica Acta* **1984**, *29*, 1527–1537.
- (2) Ge, X.; Sumboja, A.; Wu, D.; An, T.; Li, B.; Goh, F. W. T.; Hor, T. S. A.; Zong, Y.; Liu, Z. Oxygen Reduction in Alkaline Media: From Mechanisms to Recent Advances of Catalysts. *ACS Catal.* **2015**, *5*, 4643–4667.
- (3) Pourbaix, M. *Atlas of Electrochemical equilibria in Aqueous Solutions*; 2nd Edition.; National Association of Corrosion Engineers, 1974.
- (4) Trasatti, S. Electrocatalysis by oxides — Attempt at a unifying approach. *J. Electroanal. Chem. Interfacial Electrochem.* **1980**, *111*, 125–131.
- (5) Dombrovskis, J. K.; Palmqvist, A. E. C. Recent Progress in Synthesis, Characterization and Evaluation of Non-Precious Metal Catalysts for the Oxygen Reduction Reaction. *Fuel Cells* **2016**, *16*, 4–22.
- (6) Noonan, K. J. T.; Hugar, K. M.; Kostalik, H. A.; Lobkovsky, E. B.; Abruña, H. D.; Coates, G. W. Phosphonium-Functionalized Polyethylene: A New Class of Base-Stable Alkaline Anion Exchange Membranes. *J. Am. Chem. Soc.* **2012**, *134*, 18161–18164.
- (7) Kostalik, H. A.; Clark, T. J.; Robertson, N. J.; Mutolo, P. F.; Longo, J. M.; Abruña, H. D.; Coates, G. W. Solvent Processable Tetraalkylammonium-Functionalized Polyethylene for Use as an Alkaline Anion Exchange Membrane. *Macromolecules* **2010**, *43*, 7147–7150.
- (8) Couture, G.; Alaaeddine, A.; Boschet, F.; Ameduri, B. Polymeric materials as anion-exchange membranes for alkaline fuel cells. *Prog. Polym. Sci.* **2011**, *36*, 1521–1557.
- (9) Gu, S.; Cai, R.; Luo, T.; Chen, Z.; Sun, M.; Liu, Y.; He, G.; Yan, Y. A Soluble and Highly Conductive Ionomer for High-Performance Hydroxide Exchange Membrane Fuel Cells. *Angew. Chem. Int. Ed.* **2009**, *48*, 6499–6502.
- (10) Ge, X.; Liu, Z. L.; Goh, F. W. T.; Zong, Y.; Li, B.; Zhang, J.; Hor, T. S. A. Bifunctional catalysts for oxygen reduction and evolution reactions and rechargeable metal air batteries using the same **2015**.
- (11) Mao, L.; Zhang, D.; Sotomura, T.; Nakatsu, K.; Koshihara, N.; Ohsaka, T. Mechanistic study of the reduction of oxygen in air electrode with manganese oxides as electrocatalysts. *Electrochimica Acta* **2003**, *48*, 1015–1021.
- (12) Chen, G.; Bare, S. R.; Mallouk, T. E. Development of Supported Bifunctional Electrocatalysts for Unitized Regenerative Fuel Cells. *J. Electrochem. Soc.* **2002**, *149*, A1092–A1099.
- (13) Gorlin, Y.; Jaramillo, T. F. A Bifunctional Nonprecious Metal Catalyst for Oxygen Reduction and Water Oxidation. *J. Am. Chem. Soc.* **2010**, *132*, 13612–13614.
- (14) Lee, Y.; Suntivich, J.; May, K. J.; Perry, E. E.; Shao-Horn, Y. Synthesis and Activities of Rutile IrO<sub>2</sub> and RuO<sub>2</sub> Nanoparticles for Oxygen Evolution in Acid and Alkaline Solutions. *J. Phys. Chem. Lett.* **2012**, *3*, 399–404.

- (15) Cherevko, S.; Geiger, S.; Kasian, O.; Kulyk, N.; Grote, J.-P.; Savan, A.; Shrestha, B. R.; Merzlikin, S.; Breitbach, B.; Ludwig, A.; Mayrhofer, K. J. J. Oxygen and hydrogen evolution reactions on Ru, RuO<sub>2</sub>, Ir, and IrO<sub>2</sub> thin film electrodes in acidic and alkaline electrolytes: A comparative study on activity and stability. *Catal. Today* **2015**.
- (16) Liang, Y.; Wang, H.; Zhou, J.; Li, Y.; Wang, J.; Regier, T.; Dai, H. Covalent Hybrid of Spinel Manganese–Cobalt Oxide and Graphene as Advanced Oxygen Reduction Electrocatalysts. *J. Am. Chem. Soc.* **2012**, *134*, 3517–3523.
- (17) Tong, X.; Xia, X.; Guo, C.; Zhang, Y.; Tu, J.; Fan, H. J.; Guo, X.-Y. Efficient Oxygen Reduction Reaction Using Mesoporous Ni-doped Co<sub>3</sub>O<sub>4</sub> Nanowire Array Electrocatalysts. *J. Mater. Chem. A* **2015**.
- (18) Du, J.; Chen, C.; Cheng, F.; Chen, J. Rapid Synthesis and Efficient Electrocatalytic Oxygen Reduction/Evolution Reaction of CoMn<sub>2</sub>O<sub>4</sub> Nanodots Supported on Graphene. *Inorg. Chem.* **2015**.
- (19) Toh, R. J.; Eng, A. Y. S.; Sofer, Z.; Sedmidubsky, D.; Pumera, M. Ternary Transition Metal Oxide Nanoparticles with Spinel Structure for the Oxygen Reduction Reaction. *ChemElectroChem* **2015**, *2*, 982–987.
- (20) Petrie, J. R.; Cooper, V. R.; Freeland, J. W.; Meyer, T. L.; Zhang, Z.; Lutterman, D. A.; Lee, H. N. Enhanced Bifunctional Oxygen Catalysis in Strained LaNiO<sub>3</sub> Perovskites. *J. Am. Chem. Soc.* **2016**.
- (21) Lee, D.-G.; Gwon, O.; Park, H.-S.; Kim, S. H.; Yang, J.; Kwak, S. K.; Kim, G.; Song, H.-K. Conductivity-Dependent Completion of Oxygen Reduction on Oxide Catalysts. *Angew. Chem. Int. Ed.* **2015**, n/a–n/a.
- (22) Jung, J.-I.; Park, S.; Kim, M.-G.; Cho, J. Tunable Internal and Surface Structures of the Bifunctional Oxygen Perovskite Catalysts. *Adv. Energy Mater.* **2015**, *5*, n/a–n/a.
- (23) Takeda, T.; Kanno, R.; Kawamoto, Y.; Takeda, Y.; Yamamoto, O. New Cathode Materials for Solid Oxide Fuel Cells Ruthenium Pyrochlores and Perovskites. *J. Electrochem. Soc.* **2000**, *147*, 1730–1733.
- (24) Jin, C.; Cao, X.; Zhang, L.; Zhang, C.; Yang, R. Preparation and electrochemical properties of urchin-like La<sub>0.8</sub>Sr<sub>0.2</sub>MnO<sub>3</sub> perovskite oxide as a bifunctional catalyst for oxygen reduction and oxygen evolution reaction. *J. Power Sources* **2013**, *241*, 225–230.
- (25) Suntivich, J.; Gasteiger, H. A.; Yabuuchi, N.; Nakanishi, H.; Goodenough, J. B.; Shao-Horn, Y. Design principles for oxygen-reduction activity on perovskite oxide catalysts for fuel cells and metal–air batteries. *Nat. Chem.* **2011**, *3*, 546–550.
- (26) Prakash, J.; Tryk, D. A.; Yeager, E. B. Kinetic Investigations of Oxygen Reduction and Evolution Reactions on Lead Ruthenate Catalysts. *J. Electrochem. Soc.* **1999**, *146*, 4145–4151.
- (27) Parrondo, J.; George, M.; Capuano, C.; Ayers, K. E.; Ramani, V. Pyrochlore electrocatalysts for efficient alkaline water electrolysis. *J. Mater. Chem. A* **2015**, *3*, 10819–10828.
- (28) H. S. HOROWITZ; J. M. LONGO; H. H. HOROWITZ; J. T. LEWANDOWSKI The Synthesis and Electrocatalytic Properties of Nonstoichiometric Ruthenate Pyrochlores. In *Solid State Chemistry in Catalysis*; ACS Symposium Series; American Chemical Society, 1985; Vol. 279, pp. 143–163.
- (29) Queiroz, A. C.; Lima, F. H. B. Electrocatalytic activity and stability of Co and Mn-based oxides for the oxygen reduction reaction in alkaline electrolyte. *J. Electroanal. Chem.* **2013**, *707*, 142–150.
- (30) Cheng, F.; Su, Y.; Liang, J.; Tao, Z.; Chen, J. MnO<sub>2</sub>-Based Nanostructures as Catalysts for Electrochemical Oxygen Reduction in Alkaline Media. *Chem. Mater.* **2010**, *22*, 898–905.

- (31) Roche, I.; Chaînet, E.; Chatenet, M.; Vondrák, J. Carbon-Supported Manganese Oxide Nanoparticles as Electrocatalysts for the Oxygen Reduction Reaction (ORR) in Alkaline Medium: Physical Characterizations and ORR Mechanism. *J. Phys. Chem. C* **2007**, *111*, 1434–1443.
- (32) Huang, W.; Zhong, H.; Li, D.; Tang, P.; Feng, Y. Reduced Graphene Oxide Supported CoO/MnO<sub>2</sub> Electrocatalysts from Layered Double Hydroxides for Oxygen Reduction Reaction. *Electrochimica Acta* **2015**, *173*, 575–580.
- (33) Egdell, R. G.; Goodenough, J. B.; Hamnett, A.; Naish, C. C. Electrochemistry of ruthenates. Part 1.—Oxygen reduction on pyrochlore ruthenates. *J. Chem. Soc. Faraday Trans. 1 Phys. Chem. Condens. Phases* **1983**, *79*, 893–912.
- (34) Abbott, D. F.; Mukerjee, S.; Petrykin, V.; Bastl, Z.; Halck, N. B.; Rossmesl, J.; Krtil, P. Oxygen reduction on nanocrystalline ruthenia – local structure effects. *RSC Adv.* **2014**, *5*, 1235–1243.
- (35) Jang, H.; Zahoor, A.; Jeon, J. S.; Kim, P.; Lee, Y. S.; Nahm, K. S. Sea Urchin Shaped  $\alpha$ -MnO<sub>2</sub>/RuO<sub>2</sub> Mixed Oxides Nanostructure as Promising Electrocatalyst for Lithium–Oxygen Battery. *J. Electrochem. Soc.* **2015**, *162*, A300–A307.
- (36) Guo, K.; Li, Y.; Yang, J.; Zou, Z.; Xue, X.; Li, X.; Yang, H. Nanosized Mn–Ru binary oxides as effective bifunctional cathode electrocatalysts for rechargeable Li–O<sub>2</sub> batteries. *J. Mater. Chem. A* **2013**, *2*, 1509–1514.
- (37) Anthony, J. W.; Bideaux, R. A.; Bladh, K. W.; Nichols, M.C. Pyrolusite. In *Handbook of Mineralogy*; Mineral Data Publishing: Tucson, AZ.
- (38) Sun, M.; Lan, B.; Yu, L.; Ye, F.; Song, W.; He, J.; Diao, G.; Zheng, Y. Manganese oxides with different crystalline structures: Facile hydrothermal synthesis and catalytic activities. *Mater. Lett.* **2012**, *86*, 18–20.
- (39) Musil, M.; Choi, B.; Tsutsumi, A. Morphology and Electrochemical Properties of  $\alpha$ -,  $\beta$ -,  $\gamma$ -, and  $\delta$ -MnO<sub>2</sub> Synthesized by Redox Method. *J. Electrochem. Soc.* **2015**, *162*, A2058–A2065.
- (40) Yin, B.; Zhang, S.; Jiang, H.; Qu, F.; Wu, X. Phase-controlled synthesis of polymorphic MnO<sub>2</sub> structures for electrochemical energy storage. *J. Mater. Chem. A* **2015**, *3*, 5722–5729.
- (41) Kuang, P.-Y.; Liang, M.-H.; Kong, W.-Y.; Liu, Z.-Q.; Guo, Y.-P.; Wang, H.-J.; Li, N.; Su, Y.-Z.; Chen, S. Anion-assisted one-pot synthesis of 1D magnetic  $\alpha$ - and  $\beta$ -MnO<sub>2</sub> nanostructures for recyclable water treatment application. *New J. Chem.* **2015**, *39*, 2497–2505.
- (42) Park, J.-N.; Shon, J. K.; Jin, M.; Hwang, S. H.; Park, G. O.; Boo, J.-H.; Han, T. H.; Kim, J. M. Highly Ordered Mesoporous  $\alpha$ -Mn<sub>2</sub>O<sub>3</sub> for Catalytic Decomposition of H<sub>2</sub>O<sub>2</sub> at Low Temperatures. *Chem. Lett.* **2010**, *39*, 493–495.
- (43) Cueva, P.; Hovden, R.; Mundy, J. A.; Xin, H. L.; Muller, D. A. Data Processing for Atomic Resolution Electron Energy Loss Spectroscopy. *Microsc. Microanal.* **2012**, *18*, 667–675.
- (44) Levin, E. M.; Robbins, C. R.; McMurdie, H. F. *Phase Diagram for Ceramicists*; The American Ceramic Society, Inc.; Vol. 1.
- (45) ICSC 0175 - MANGANESE DIOXIDE  
<http://www.inchem.org/documents/icsc/icsc/eics0175.htm> (accessed May 25, 2016).
- (46) Bentley, J.; Gilliss, S. R.; Carter, C. B.; Al-Sharab, J. F.; Cosandey, F.; Anderson, I. M.; Kotula, P. J. Nanoscale EELS analysis of oxides: composition mapping, valence determination and beam damage. *J. Phys. Conf. Ser.* **2006**, *26*, 69.
- (47) Koh, A. L.; Bao, K.; Khan, I.; Smith, W. E.; Kothleitner, G.; Nordlander, P.; Maier, S. A.; McComb, D. W. Electron Energy-Loss Spectroscopy (EELS) of Surface Plasmons in

- Single Silver Nanoparticles and Dimers: Influence of Beam Damage and Mapping of Dark Modes. *ACS Nano* **2009**, *3*, 3015–3022.
- (48) Blizanac, B. B.; Ross, P. N.; Markovic, N. M. Oxygen electroreduction on Ag(1 1 1): The pH effect. *Electrochimica Acta* **2007**, *52*, 2264–2271.
- (49) Ramaswamy, N.; Mukerjee, S. Influence of Inner- and Outer-Sphere Electron Transfer Mechanisms during Electrocatalysis of Oxygen Reduction in Alkaline Media. *J. Phys. Chem. C* **2011**, *115*, 18015–18026.
- (50) Ya-Jie, C.; Xiao-Yu, Z.; Tian-Yi, C.; Zhen-Ya, L. Hopping and Non-universal Conductivity in Half-Metallic CrO<sub>2</sub> Composites. *Chin. Phys. Lett.* **2003**, *20*, 721.
- (51) Woo, S. I.; Lee, C. S.; Han, J. D. Effect of additives on the morphology and magnetic properties of chromium oxide(CrO<sub>2</sub>) in the hydrothermal decomposition of chromium trioxide. *Ind. Eng. Chem. Res.* **1992**, *31*, 1407–1414.

## CHAPTER 5

### PERFORMANCE AND MECHANISM OF NIOBIUM (OXY)NITRIDES AS LITHIUM- ION BATTERY ANODE

Ryo H. Wakabayashi, James P. Pastore, Jie Gao, Francis J. DiSalvo\*, and Héctor D. Abruña\*

Department of Chemistry, Cornell University, Ithaca, New York 14853-1301

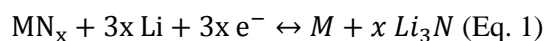
#### **5.1 Introduction**

Since the discovery of lithium-ion batteries in the late 1970s<sup>1</sup> and their commercialization in the early 1990s, they have revolutionized electrical energy storage. While they have enabled technologies such as portable electronics and even electric vehicles, the practical capacity of the anode today (carbon) is about 250 mAh/g. The theoretical capacity is 372 mAh/g, which means that, even if both the cathode and the anode could deliver their theoretical capacities, the overall capacity only increases by 50 %. Such an increase in capacity will not, however, enable electric vehicles with driving ranges comparable to those of internal combustion engine cars. To that end, new chemistries are necessary to advance the field.

One possible solution is to move away from the insertion/intercalation chemistry developed by Whittingham.<sup>1</sup> Popular intercalation cathodes like  $\text{LiCoO}_2$ ,  $\text{LiNi}_{(1-x-y)}\text{Mn}_x\text{Co}_y\text{O}_2$ , and  $\text{LiFePO}_4$ , paired with a graphite anode, have revolutionized the field of electrical energy storage. However, their capacities are limited by the simple fact that intercalation compounds can only incorporate a limited number of lithium ions per formula unit and withstand significant changes in oxidation state without a structural change.<sup>2</sup> For example,  $\text{LiFePO}_4$ , as its stoichiometry suggests, can only react with one Li per formula unit. In contrast, many metals, oxides and other transition-metal based compounds can react reversibly by either alloying or transforming to a different phase. The benefit of such systems lies largely in the fact that they can incorporate multiple lithium atoms per formula unit. One such example is

silicon. Silicon can incorporate 4.4 Li atoms per Si (forming an ordered  $\text{Li}_{22}\text{Si}_5$  phase), giving it a very high theoretical capacity of 4200 mAh/g. However, Si electrodes lose significant capacity on cycling from cracking of particles induced by a significant volume expansion and contraction (~400 %) that accompanies the charge/discharge process.<sup>3,4</sup> In order to address this problem, nanostructuring and particle engineering have been carried out in attempts to address the issue.<sup>4,5,6,7</sup> However, the fact that Si anodes, or any other conversion electrodes, are still not widely commercialized is a clear sign that there is much work to be done before conversion electrodes replace intercalation electrodes.

Many metal nitrides are conductive, and can react with lithium to form lithium nitride, making them interesting candidates as new-generation conversion anodes. The reaction with lithium, assuming full conversion, is proposed (or at least assumed) as follows:



Graphite anodes, for comparison, can only incorporate 1 lithium atom per 6 atoms of C. This illustrates why conversion electrodes typically have a much higher theoretical capacity than insertion electrodes across the board, despite the fact that most of them have higher molar mass than carbon. Specifically, for nitrides, the theoretical capacities (assuming that Eq. 1 goes to full completion) are listed in Table 5.1.

Nitride	MM (g/mol)	Theo. Cap. (mAh/g)
TiN	61.87	1299
VN	64.95	1238
CrN	66.00	1218
MnN	68.94	1166
FeN	69.85	1151
CoN	72.93	1102
ZrN	105.24	764
NbN	106.91	752
Mo <sub>2</sub> N	205.88	391
C (C <sub>6</sub> )	72	372

**Table 5.1.** Calculated theoretical capacities of metal nitrides as lithium-ion battery anodes, and carbon for comparison. Molar mass of C is for “C<sub>6</sub>”.

Despite the attractive theoretical capacities, little is known about nitrides as battery electrodes, in terms of both their performance and reaction mechanisms. A significant portion of the studies on nitride battery electrodes are thin-film batteries<sup>8,9,10,11,12,13</sup> that do not necessarily translate to larger format batteries. Reports on nitride-coated oxide materials exist as well,<sup>3,14</sup> but they do not represent or exemplify the chemistry of nitrides as the nitride coatings are largely there for electrical conductivity. A few powder nitride materials have been studied as well. Powder Zn<sub>3</sub>N<sub>2</sub> was shown to be reversible at approx. 550 mAh/g with the discharge product being a mixture of LiZnN, LiZn and β-Li<sub>3</sub>N, and poor cyclability being attributed to “grinding” of LiZn particles.<sup>15</sup> Also, some pre-lithiated nitrides have been investigated before<sup>16,17</sup>. For example, Li<sub>3-x</sub>Co<sub>x</sub>N (x ≤ 0.5), in particular, was shown to be a reversible insertion electrode, which is a nice property but does not have the benefit of high capacity.<sup>18</sup> Ni<sub>3</sub>N, a so-called interstitial nitride, was studied as an anode material and was reversible at approx. 600 mAh/g, but that performance depended heavily on synthetic

methods.<sup>19</sup> As Table 5.1 suggests, however, there are many more known nitrides that may be of interest as new lithium-ion battery electrode materials.

We therefore decided to explore the battery performance and mechanism of various rock-salt nitrides. First, we investigated the battery performance of various rock-salt transition-metal nitrides synthesized by Dr. Minghui Yang, a former postdoctoral associate in the DiSalvo lab. The results will be discussed briefly. From such initial screening, we came to the conclusion that NbN had the best combination of cyclability and capacity, so we decided to further investigate the effects of processing conditions. Specifically, the effects of ammonolysis temperature of the oxide precursors, and addition of secondary metals such as aluminum, tantalum, and silicon were investigated. Niobium nitride, and specifically Nb<sub>4</sub>N<sub>5</sub>, was previously reported as a supercapacitor electrode.<sup>20</sup> While it showed encouraging results, the performance was largely due to the pseudocapacitive incorporation of protons, and lithium chemistry was not explored.

In addition, to our knowledge, there has only been one mechanistic study reported of rock-salt (M: N = 1: 1) nitrides, which coincidentally was a niobium nitride anode.<sup>21</sup> It reported on the change in crystal structure upon charging and discharging. While they claim (Figure 5 of their manuscript) that metallic Nb is visible after 50 cycles, the peak at approx. 38° (assigned to metallic Nb) can be seen in the “before” XRD where the signal-to-noise ratio is much better than the “after” image. So, we found this to be an inconclusive evidence of any structural change.

With this in mind, and with the help of a collaborator (James Pastore), we decided to explore the mechanism of the charge/discharge process of Nb<sub>1-x</sub>O<sub>y</sub>N<sub>1-y</sub> through the use of *operando* X-ray diffraction (XRD) and *operando* X-ray absorption spectroscopy (XAS). XRD, as mentioned above, provides insight on changes in structure as NbN anodes are charged and discharged. XAS can be divided into two sub-components: X-ray absorption near-edge

structure (XANES) and extended X-ray absorption fine structure (EXAFS). The former provides information about oxidation state and electronic structure of the samples, while the latter provides insight into coordination and (short-range) ordering in the materials of interest.

## 5.2 Experimental

### 5.2.1 Synthesis of $Nb_{1-x}O_xN_{1-y}$

$Nb(OEt)_5$  (Strem, 99%), ethanol (200 proof, KOPTEC), and  $NH_4OH$  (EMD) were used as received. First, a 3-neck round bottom flask was evacuated to 60 mtorr or lower on a Schlenk line. After backfilling the flask with Ar, 20 mL of ethanol were pumped into the flask using a syringe, followed by the addition of  $Nb(OEt)_5$  (approx. 0.6 mL, or 0.002 mol), and stirred for several minutes. Where appropriate,  $Ta(OEt)_5$  (Strem),  $Al(NO_3)_3 \cdot 9H_2O$  (Sigma-Aldrich), and  $Si(OEt)_4$  (Aldrich) were also added with  $Nb(OEt)_5$  except for  $Al(NO_3)_3 \cdot 9H_2O$  which was added into the 3-neck flask before evacuation (total metal  $\sim 0.002$  mol). The solution was then transferred, using the cannula transfer technique, into approximately 30 mL of 1.5 M  $NH_4OH$  under rapid stirring, which resulted in an instantaneous formation of a white gel. The gel was heated to ca. 80 °C to evaporate the solvents and form a dry gel, followed by calcination at 450°C to form the amorphous oxide precursor.

The oxide precursor was then ball-milled using a Fritsch Pulverisette 7 planetary mill with Super P carbon (TIMCAL) to reduce the particle size and thoroughly mix carbon and the oxide. Milling the nitride products, which are very hard, results in contamination of the samples with the mill material, even with tungsten carbide bowls and balls. The mixed oxide was then heated under  $NH_3$  (Airgas, anhydrous) flow (approx. 6 L/h) at various temperatures for 24 hours, yielding fine black powders.

### 5.2.2 Physical Characterization

Powder X-ray diffraction measurements were done using a Rigaku Ultima IV (Cu  $K_{\alpha}$ ,  $\lambda=1.5406$  Å for  $K_{\alpha 1}$ , 1.5444 Å for  $K_{\alpha 2}$ ). Refinements were done using PDXL (Rigaku).

Nitrogen and oxygen contents were measured using a LECO TC-600 thermal N/O analyzer, with Si<sub>3</sub>N<sub>4</sub> as the standard.

### 5.2.3 Coin Cell Testing (performed by Dr. Jie Gao and James Pastore)

The (oxy)nitride samples were made into a slurry using poly(vinylidene fluoride) (PVDF, Aldrich) as a binder (active: C: binder = 70: 20: 10) and n-methyl-2-pyrrolidone (NMP) as the solvent. The resulting slurry was cast on copper (thickness = 25 μm), the current collector, using a doctor blade. To make a coin cell (CR 2032), Li foil (Sigma-Aldrich) was used as the other electrode, with nickel foam as a current collector. 1 M LiPF<sub>6</sub> in ethylene carbonate/diethyl carbonate (EC/DEC; 1:1 v/v ratio, BASF pre-made electrolyte) mixture was used as the electrolyte solution, and Celgard (20 μm thickness) was used as the separator. The assembled cells were tested at 20 mA/g, unless otherwise noted, using an Arbin Instruments BT2000 coin cell tester.

### 5.2.4 Operando X-ray Diffraction and X-ray Absorption Spectroscopy (performed by Pastore)

For *operando* experiments, the coin cells were assembled using the identical materials in a similar manner. However, holes (approx. 3 mm) were drilled into every component except the Celgard separator and the active material, so as to allow a higher flux of X-rays through the cell and minimize background scatter. The holes on the coin cell casings were sealed by gluing (TorrSeal) a Kapton film (5 mil thick).

All *operando* experiments were done at the Cornell High Energy Synchrotron Source (CHESS). A Biologic SP-200 potentiostat was used to control the charge/discharge reactions in all experiments. XRD experiments were done with a beam energy of 27.04 keV. Pilatus K300 was used as the detector. XAS was performed by scanning the energy range of monochromatic X-ray around 19.989 keV, which is the energy of Nb K-edge. Custom-made ion chambers were used as counters. Chamber 0 was located immediately next to the incoming beam. The sample was set between chambers 1 and 2. A Nb foil (reference) was placed

between chambers 2 and 3. A rough schematic of the experimental setup is shown in Figure 5.1.

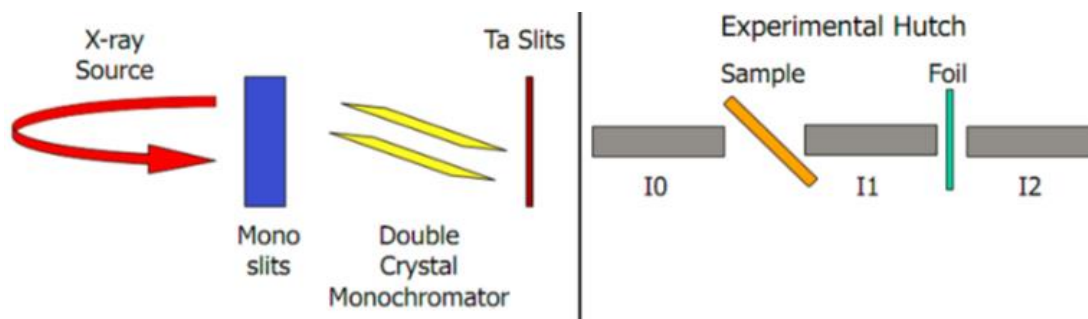
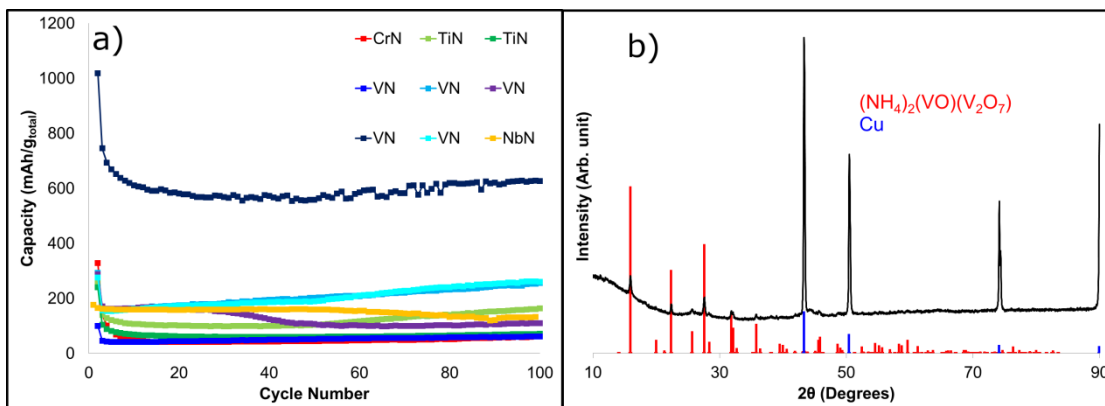


**Figure 5.1.** A simple schematic of the experimental set-up of X-ray Absorption Spectroscopy, taken from DeBeer.<sup>22</sup>

### 5.3 Results and Discussions

1. *5.3.1 Survey of a Few Metal Nitrides* (synthesis by Yang; cell testing performed by Gao and Pastore)

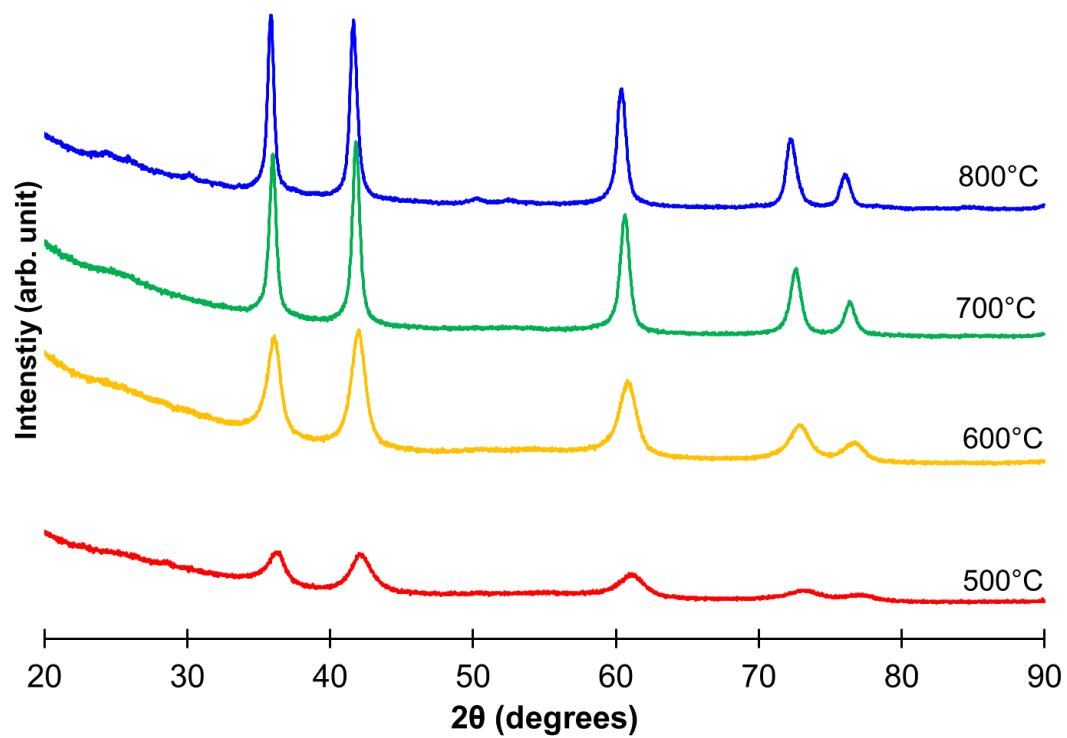
Figure 5.2 shows the discharge capacity results of various nitride samples prepared by Dr. Minghui Yang. His general synthetic methods can be found in his manuscripts.<sup>23,24</sup> Briefly, crystalline phases of  $A_xM_yO_z$  ( $A = K, Cd$  or  $Zn$ ,  $M =$  transition metal for the desired nitride product) was heated under flowing  $NH_3$  at a minimum temperature of  $600\text{ }^\circ C$  to sublime the “A” metal away, yielding highly porous metal nitride products. Some of the vanadium nitrides appear to have good performance, but the highest-capacity sample was later shown to be something other than the rock-salt VN (Figure 5.1(b)), and the performance behavior of VN, in general, was inconsistent. CrN and TiN showed comparably lower capacities than NbN. Therefore, we decided to use NbN as our model system.



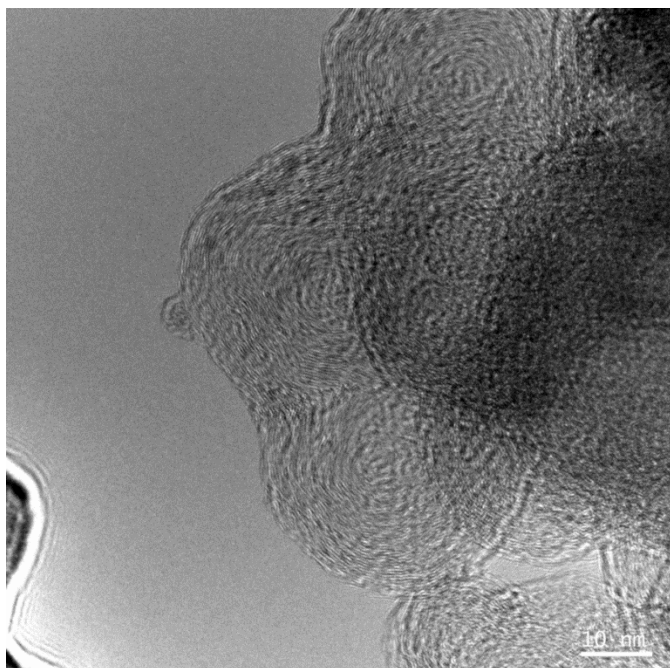
**Figure 5.2.** (a) Discharge capacities of various metal nitride samples prepared by Dr. Minghui Yang (except NbN, which is my own work). (b) pXRD of the highest-capacity VN, cast on Cu. Red and blue lines are database peaks of ammonium metavanadate (red) and copper (blue) respectively.

### 5.3.2 In-depth Look at Niobium (Oxy)nitride (cell testing performed by Gao and Pastore)

Figure 5.3 shows (ex-situ) X-ray diffraction patterns of  $\text{Nb}_{1-x}\text{O}_x\text{N}_{1-\gamma}$ , made at different temperatures. Samples begin to crystallize in a rock-salt (Fm-3m) structure at 500 °C (See Figure 5.3), and at 800 °C, traces of  $\text{Nb}_4\text{N}_5$  (I4/m) can be seen. An interesting observation to note is that, despite the 500 °C and the 600 °C samples having similar FWHM (for the first peak: 500 °C = 1.47° and 600 °C = 1.15°, 6.2 and 7.8 nm domain size assuming the Scherrer constant is 0.944), the peak intensity and therefore the integrated counts are clearly lower. This suggests a lower degree of crystallinity. Figure 5.4 shows a TEM image of the  $\text{Nb}_{1-x}\text{O}_x\text{N}_{1-\gamma}$  (mixed with C) synthesized at 500 °C. Parts of the particles appear crystalline but other parts look less so. While this is to be taken with a grain of salt because factors such as sample orientation affect how visible the lattice fringes are in TEM images, it was still a very curious result.

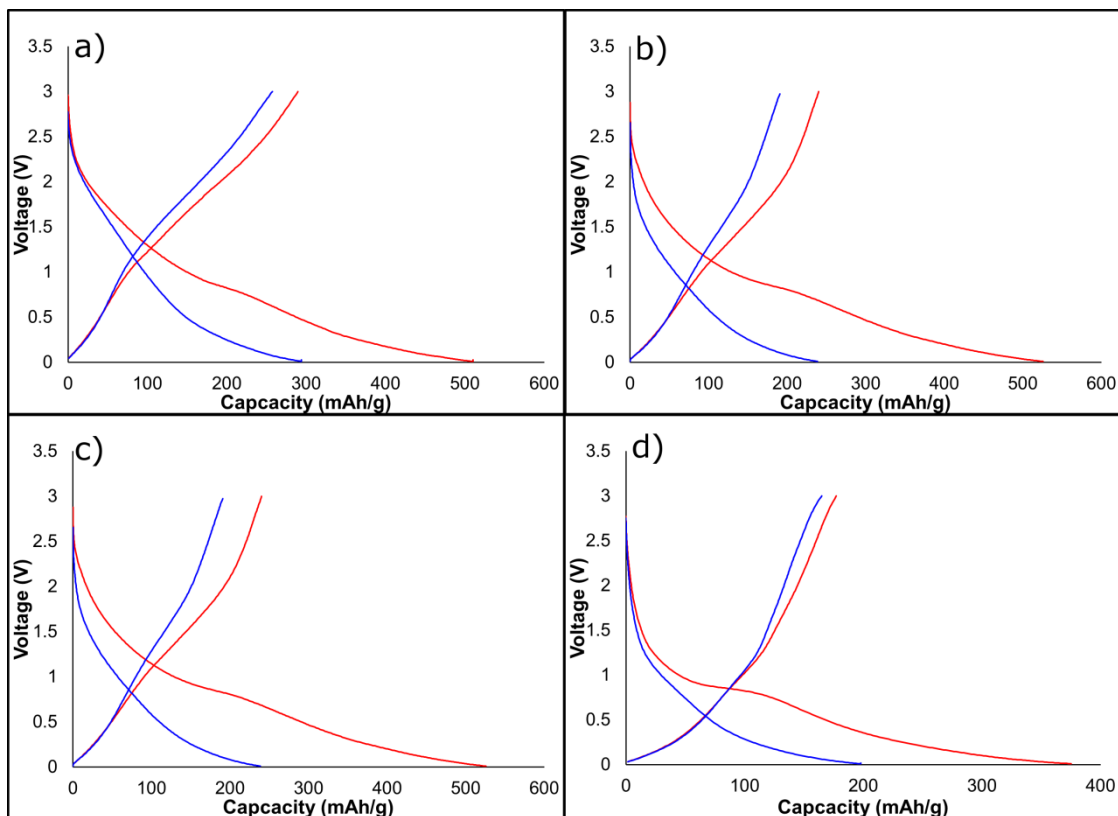


**Figure 5.3.** Powder XRD patterns of Nb<sub>1-x</sub>O<sub>x</sub>N<sub>1-γ</sub>/C, made under flowing NH<sub>3</sub> at different synthesis temperatures.

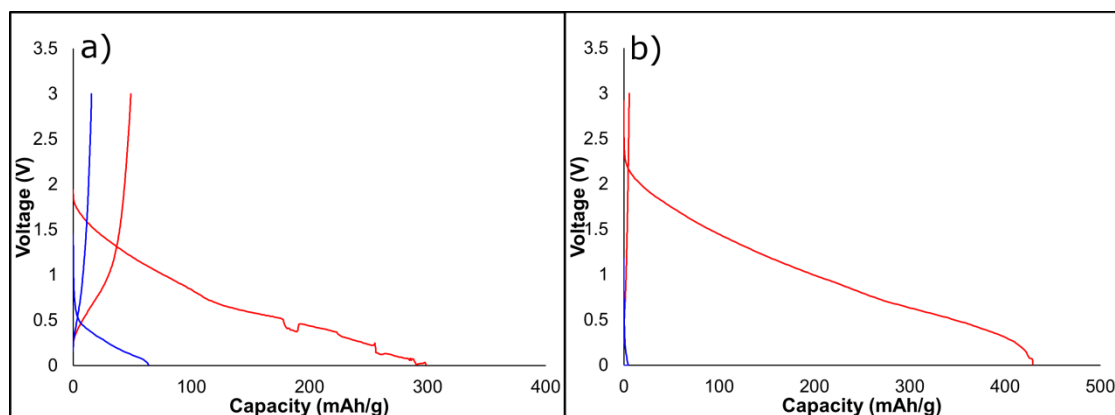


**Figure 5.4.** TEM image of Nb<sub>1-x</sub>O<sub>x</sub>N<sub>1-γ</sub>, synthesized at 500 °C.

Figure 5.5 shows the charge-discharge curves of  $\text{Nb}_{1-x}\text{O}_x\text{N}_{1-\gamma}$  synthesized at 500-800 °C, at 20 mA/h. In all cases, only the first discharge shows plateau-like regions. Lack of a clear plateau indicates that there is no equilibrium between two phases, which is consistent with conversion electrodes. The first re-charge clearly does not return all the capacity of the first discharge, which is typical of conversion electrodes. Such phenomenon is generally attributed to an irreversible phase formation, including but not limited to the development of a surface-electrolyte interface (SEI) layer. However, we believe that nitridation contributes to cyclability. Figure 5.6 shows the charge-discharge curves of niobium oxide (amorphous) samples (2 different coin cells). They both behaved like primary batteries, that is to say, their capacities dropped dramatically after the first discharge. This is likely the result of low conductivity of the oxide.

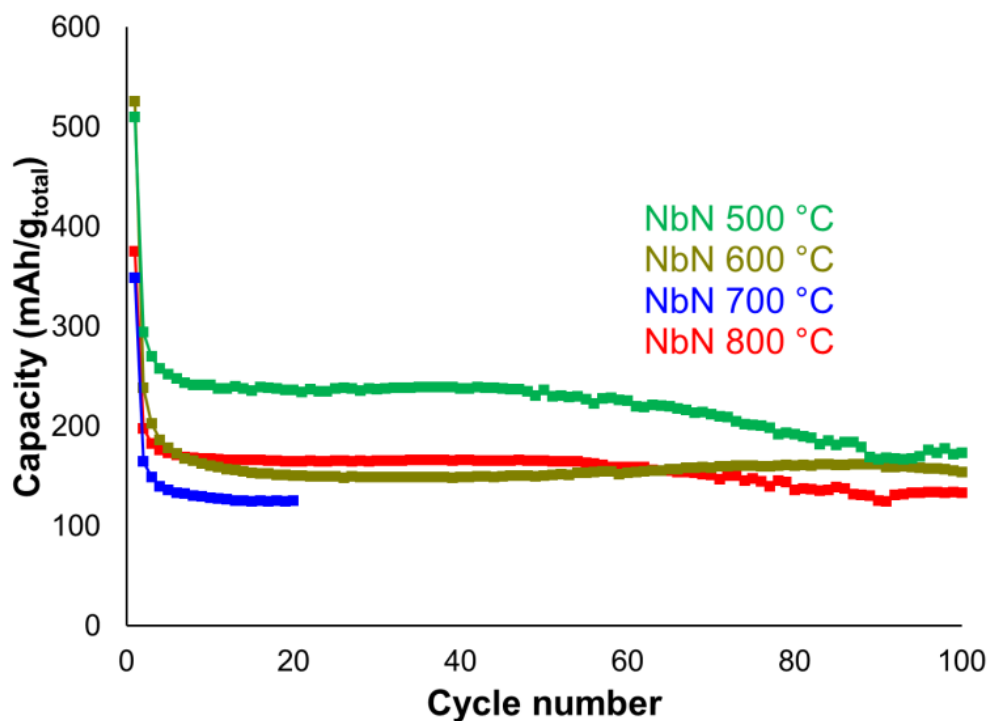


**Figure 5.5** Charge-discharge curves (red: 1<sup>st</sup> cycle; blue: 2<sup>nd</sup> cycle) of  $\text{Nb}_{1-x}\square_x\text{O}_7\text{N}_{1-\gamma}$  synthesized at (a) 500 °C (b) 600 °C (c) 700 °C (d) 800 °C. Cycled at 20 mA/h (approx. C/50)



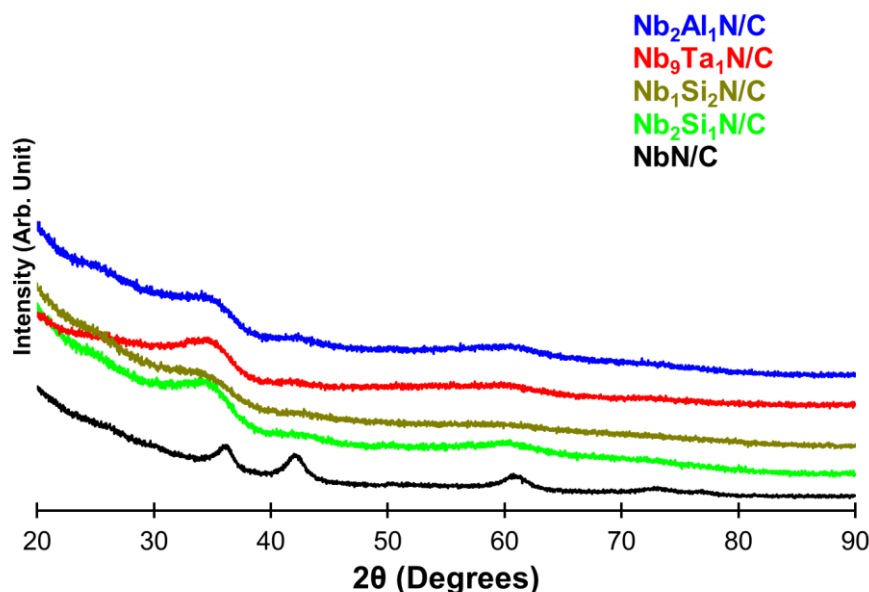
**Figure 5.6.** Charge-discharge curves (red: 1<sup>st</sup> cycle; blue: 2<sup>nd</sup> cycle) of niobium oxide (made at 450 °C). Two different curves are from two different coin cells. Cycled at C/20.

Figure 5.7 shows cycling performance results of  $\text{Nb}_{1-x}\square_x\text{O}_\gamma\text{N}_{1-\gamma}$  synthesized at 500-800 °C, over 100 cycles. The sample annealed at 500 °C performs significantly better than the other samples. As noted above, the sample annealed at 500 °C is the least crystalline sample, so we first decided to investigate the effect of crystallinity (or lack thereof) further. We decided to try this by slowing down the kinetics of crystallization. From our previous experience with synthesizing  $\text{Ti}_x\text{Ta}_y\text{Al}_z\text{N}_{1-\delta}\text{O}_\nu$  samples (previous chapter) we knew that addition of metals like Ta and Al slowed down the kinetics of crystallization of rock-salt nitride structure. So, we attempted to do the same here, as well. Ta and Al were selected as the secondary element for that very reason, and Si was selected because Si is a high-capacity anode material that suffers from cycling issues<sup>3,4,5</sup>, so we wanted to see if incorporating in a nitride/oxide matrix would help alleviate the problem.



**Figure 5.7.** Discharge capacity of  $\text{Nb}_{1-x}\square_x\text{O}_\gamma\text{N}_{1-\gamma}$  over 100 cycles. Cycled at 20 mAh/g (C/50). Blue trace is still cycling as of this writing.

Figure 5.8 shows the XRD patterns of  $\text{Nb}_{1-x-y}\text{M}_y\text{O}_\gamma\text{N}_{1-\gamma}/\text{C}$ , where  $\text{M} = \text{Si}, \text{Ta}, \text{and Al}$ , in the proportions provided in the figure, all synthesized at 500 °C. While they are all amorphous, the same treatment done without carbon yielded black samples, very likely indicating formation of metal-nitrogen bonds. The broad peak at around 20° is graphitic carbon. Figure 5.9 shows the cycling result of those samples, at C/20. With the exception of  $\text{M} = \text{Al}$ , the amorphous samples did not have higher capacity than the  $\text{Nb}_{1-x}\text{O}_\gamma\text{N}_{1-\gamma}$ , made at 500 °C.  $\text{Nb}_{1-x-0.33}\text{Al}_{0.33}\text{O}_\gamma\text{N}_{1-\gamma}/\text{C}$ , while showing a higher current, is being cycled at 20 mA/g (or approximately C/50), making the capacity a bit less impressive. We therefore largely rejected the hypothesis, and instead decided to focus on the ammonolysis temperature itself. It is a well-known phenomenon that the oxygen content in the nitride samples decreases as the ammonolysis temperature increases.<sup>25</sup>



**Figure 5.8.** Powder patterns of  $\text{Nb}_{1-x-y}\text{M}_y\text{O}_\gamma\text{N}_{1-\gamma}$ , where  $\text{M} = \text{Al}$  (blue),  $\text{Ta}$  (red),  $\text{Si}$  (mustard and green) made under flowing  $\text{NH}_3$  at 500 °C. Black trace is a replication from Figure 5.2, as a comparison/reference.

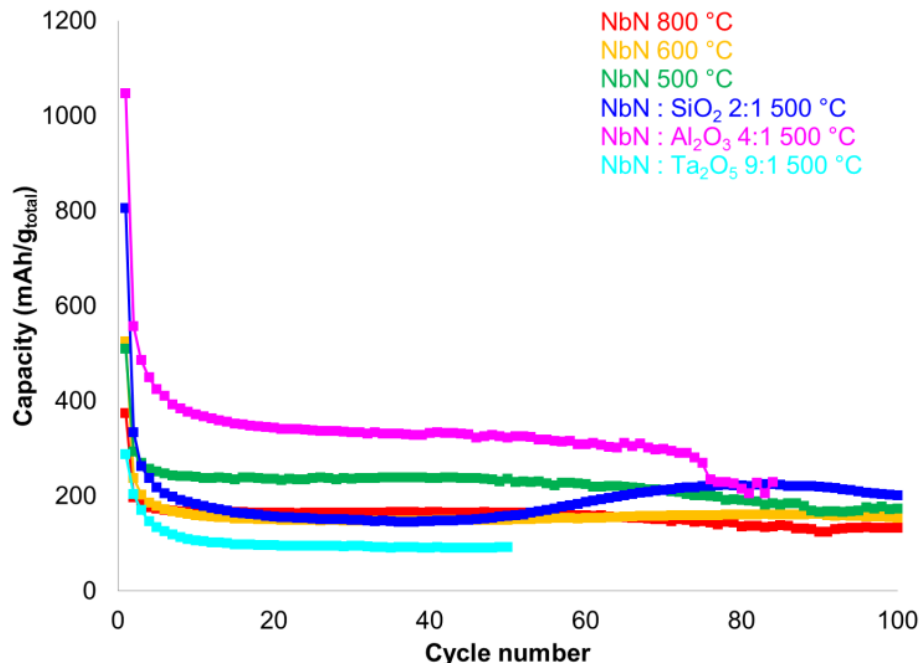


**Figure 5.9.** Discharge capacity of  $\text{Nb}_{1-x-y}\square_x\text{M}_y\text{O}_\gamma\text{N}_{1-\gamma}$  over 100 cycles.  $\text{M} = \text{Al}$  cycled at approximately  $C/50$  (20 mAh/g), all others at  $C/20$ .

Table 5.2 shows the O and N content, calculated from thermal analysis measurements. The content of oxygen decreases monotonically while the nitrogen content increases monotonically with the ammonolysis temperature, as expected. This means that the cationic vacancy concentration is considerably higher for the low-temperature samples, and in fact, for the sample heated under  $\text{NH}_3$  at  $500\text{ }^\circ\text{C}$ , half of the cationic sites are vacant. The sample made at  $800\text{ }^\circ\text{C}$  crystallized in  $\text{Nb}_4\text{N}_5$  (or  $\text{Nb}_{0.8}\text{N}$ ) structure, or in other words, NbN with ordered defect concentration of 0.2. Within the error of the O/N content measurement, the O/N data agree with the diffraction data. Therefore, at  $800\text{ }^\circ\text{C}$ , there are likely no defects other than the defects that are ordered.

Vacancies and defects in rock-salt structures is not a commonly reported phenomenon, but it is not without precedent. It was reported in 1954 that tungsten nitrides can have oxygen atoms in nitrogen sites, and very likely cationic vacancies as a way to balance charge.<sup>25</sup> Substoichiometric  $\text{TiN}_x$  ( $x < 1$ ) made by reacting urea with metallic titanium showed different

response to high-temperature annealing depending on the amount of vacancies.<sup>26</sup> HfN thin films with vacancies in either cationic or anionic sites were shown to have lower hardness and electrical conductivity than a HfN film without defects.<sup>27</sup> So, while vacancies in rock-salt structure are not a commonly discussed topic, they appear to play a critical role in materials properties. These results and literature precedence, if nothing else, highlight the problem with overreliance on XRD and the necessity to characterize the elemental composition of like (rock-salt) nitrides.

Anneal T (°C)	Nb (1-x)	Cation vacancy (x)	O ( $\gamma$ )	N (1- $\gamma$ )	Nb ox. St.
500	0.491	0.509	0.476	0.524	5.14**
600	0.625	0.375	0.368	0.632	4.21
700	0.669	0.331	0.311	0.689	4.01
800	0.837*	0.167	0.088	0.912	3.48

**Table 5.2.** Number of Nb, cationic vacancies, O, and N, if the product is written as Nb<sub>1-x</sub>O <sub>$\gamma$</sub> N<sub>1- $\gamma$</sub> , and average oxidation state of Nb as a result. “\*\*” indicates an unphysical value, but we attribute that to sampling error (less than 3%)

Looking again at Figure 5.7, we believe that the high capacity of the sample made at 500 °C may be attributed to a high defect density. It is not unreasonable to think that the mechanism of discharge is Li ions “inserting” into the defect sites. In fact, the math works out almost exactly as such. Reversible capacity of 239 mAh/g (for the sample heated at 500 °C) means that, assuming that the formula unit is Nb<sub>0.49</sub>O<sub>0.51</sub>N<sub>0.48</sub>, 0.54 moles of electrons are transferred per mole of Nb<sub>0.49</sub>O<sub>0.51</sub>N<sub>0.48</sub>. The same calculation for the sample heated at 600 °C (can be written as Nb<sub>0.62</sub>O<sub>0.38</sub>N<sub>0.63</sub>) yields 0.40 moles of electrons per mole of Nb<sub>0.62</sub>O<sub>0.38</sub>N<sub>0.63</sub>, which, again, is very close to the number of defect sites, and for the sample heated at 700 °C, 0.36 mol electrons are transferred of per mol of Nb<sub>0.67</sub>O<sub>0.33</sub>N<sub>0.69</sub>.

However, it is important to note that the defect density and number of electrons transferred do not match for the sample made at 800 °C. In theory there are approximately 0.2 moles of cation vacancies, but 0.5 moles of electron is transferred per mole of sample ( $\text{Nb}_{0.8}\text{O}_{0.1}\text{N}_{0.9}$ ). This set of data provides an interesting counterbalance with the fact that the samples with no N (the oxide samples) did not cycle well at all. Nitridation appears to be helpful in enhancing the performance but oxygen ions are still needed in the lattice to introduce vacancies.

It must be noted, however, that the capacity of the  $\text{Nb}_{1-x}\text{O}_x\text{N}_{1-y}$  batteries are sensitive to the cycling rate. Figure 5.10 shows the sample made at 700 °C, cycled at two different rates. The one cycled at C/20 shows approximately 28% lower capacity than the one cycled at 20 mAh/g, likely indicating a very slow rate of the charge/discharge reactions.

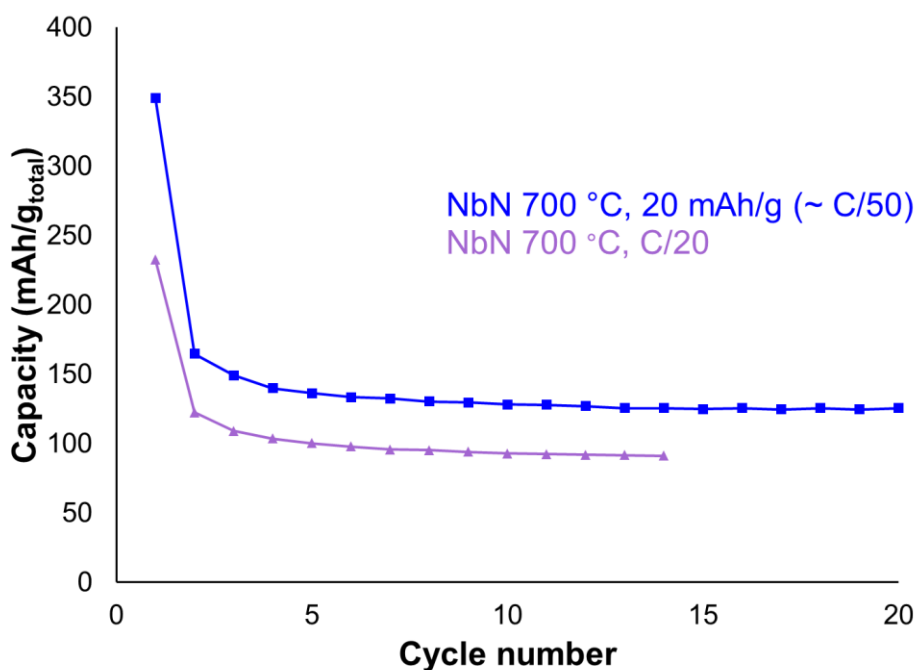


**Figure 5.10.** Discharge capacity of  $\text{Nb}_{1-x}\text{O}_x\text{N}_{1-y}$  made at 700 °C, cycled at 20 mAh/g (approx. C/50, blue) and C/20 (purple). Blue trace is a replication from Figure 5.7.

### 5.3.3 Operando X-ray Techniques (performed by Pastore)

*Operando* X-ray diffraction and X-ray absorption spectroscopy of coin cells made with sample heated under  $\text{NH}_3$  at  $500\text{ }^\circ\text{C}$  largely agree with this hypothesis. As shown in Figure 5.10, X-ray diffraction patterns showed no discernable differences in either the peak positions or the intensities of the peaks, from the start of discharge to the end of re-charge. This would be consistent with the idea that lithium simply occupies the vacant cationic sites upon discharging. Lithium ions are nearly the same size as niobium ( $\text{Li}^{1+} = 90\text{ pm}$ ,  $\text{Nb}^{3+} = 86\text{ pm}$ , though  $\text{Nb}^{5+} = 78\text{ pm}^{28,29}$ ), and lithium, with  $Z = 3$ , does not significantly change the intensities of the peaks in X-ray diffraction (peak intensities are roughly proportional to  $Z^2$ , and  $43^2 \gg 3^2$ ).

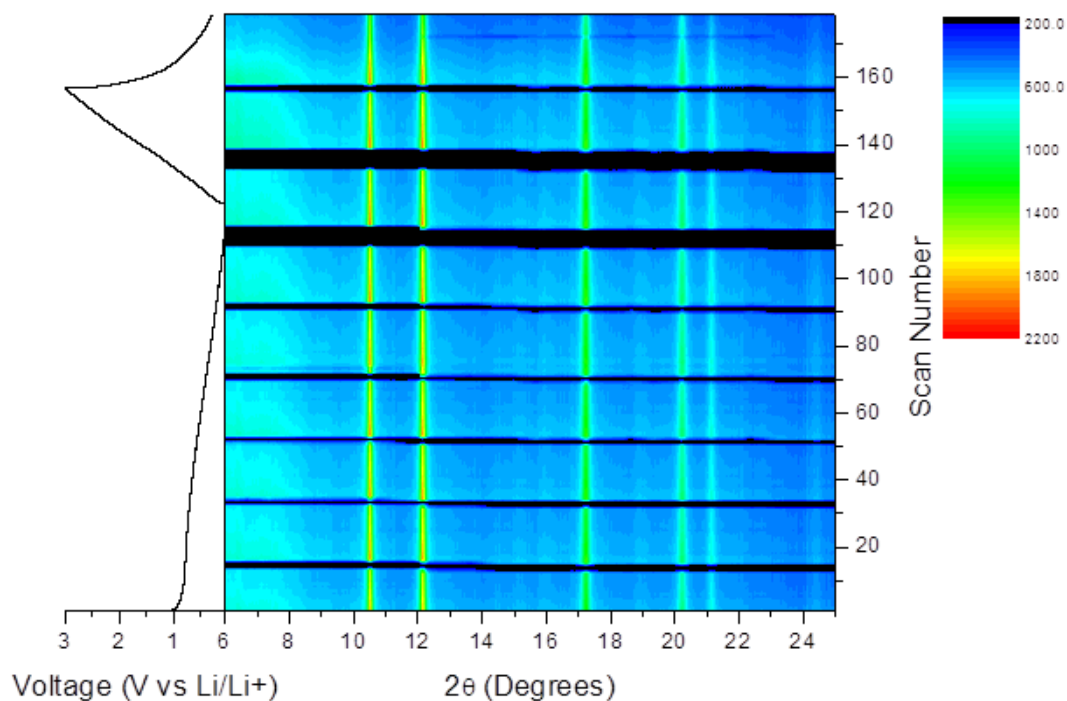


**Figure 5.11.** *Operando* XRD diffraction of  $\text{Nb}_{1-x}\square_x\text{O}_{\gamma}\text{N}_{1-\gamma}$  (made at  $500\text{ }^\circ\text{C}$ ). Curve on the left is the charge-discharge behavior, and the colored graph on the right side is the XRD peaks at corresponding state. The black streaks correspond to beam fill at CHESS. (Figure by James Pastore)

The *operando* X-ray absorption spectroscopy (specifically, XANES) of a sample heated under  $\text{NH}_3$  at 500 °C is shown in Figure 5.11. The battery capacity data are consistent with the *ex-situ* data (for the first cycle), indicating that the X-ray beam or the modified cell configuration did not significantly affect the chemistry of the battery. Initially, a clear “pre-peak” around 1.898 keV, indicative of +5 state of Nb, can be seen.<sup>30</sup> This is consistent with the data from the N/O analyzer. Reduction (curve shifting towards left, or lower energy) of approx. 1.7 eV was seen, indicating reduction. Charging shifts the edge back towards higher energy, but it does not go back to the original energy (shift of 1.2 eV; see Figure 5.11(c)), indicating irreversibility. Notably, the “pre-peak” does not reappear. As of this writing, quantification of the edge energies vs. oxidation state has not been done.

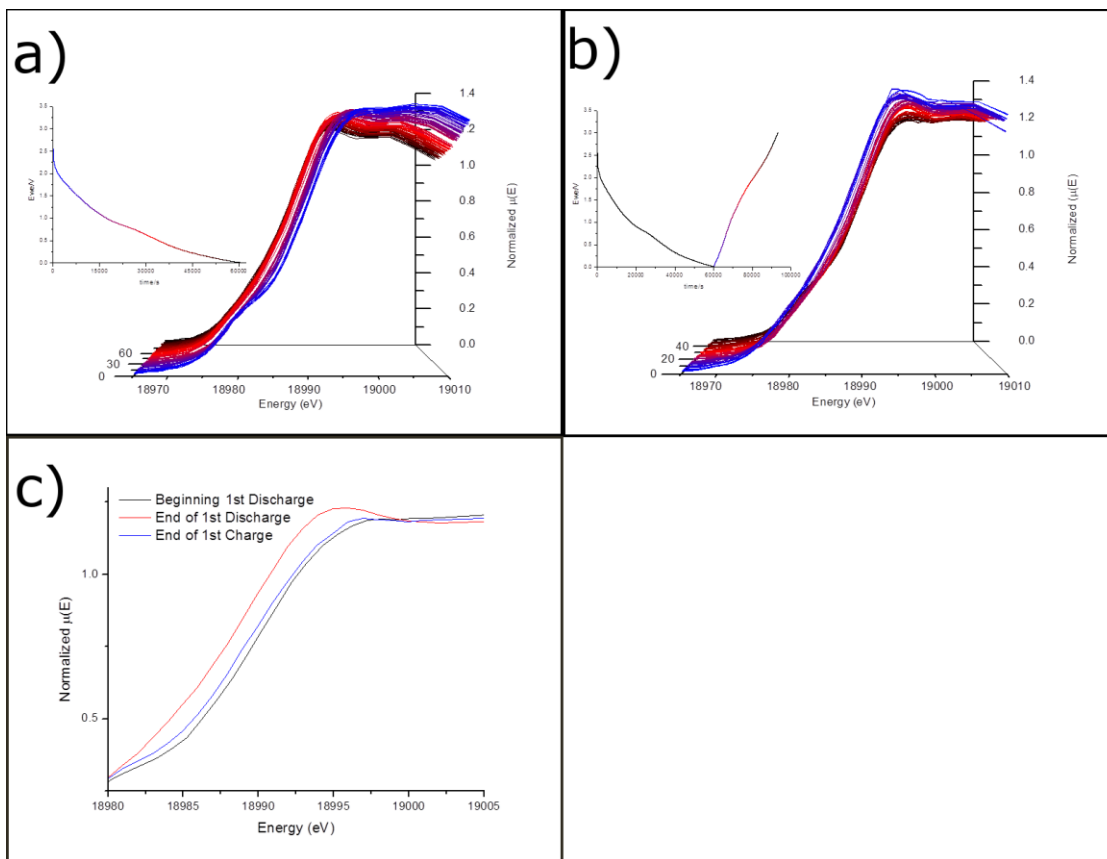


**Figure 5.12.** *Operando* XAS of  $\text{Nb}_{1-x}\text{O}_x\text{N}_{1-\gamma}$  (made at 500 °C), (a) discharge process and (b) charge process. (c) Summarizes the beginning and end of scans shown in (a) and (b).

(Figure by James Pastore)

## 5.4 Conclusions

$\text{Nb}_{1-x}\text{O}_x\text{N}_{1-\gamma}$ , and mixtures of  $\text{Nb}_{1-x}\text{O}_x\text{N}_{1-\gamma}$  with secondary elements such as Al, Ta, Si, and Sn, have been synthesized, and tested as anodes in lithium-ion batteries. It was found that the rock-salt NbN structure can actually incorporate a varying amount of oxygen, and cationic vacancies for the charge balance, and that the amount of oxygen/vacancies is clearly correlated to the ammonolysis temperature. It appeared to be largely due to the defect content, introduced as a result of oxygen atoms occupying the N sites of the rock-salt nitrides, that affect the battery chemistry, which is supported by N/O data analysis, as well as *operando* XRD and XANES.

### 5.5 Future Directions

It would be interesting to synthesize the other transition metal nitrides that were tested in Figure 1, but at lower temperatures. We now know that the ammonolysis temperature is highly relevant in terms of elemental composition and battery performance. Given that, we may be able to get TiN and other nitrides to cycle far better.

Also, a smaller potential window for the cycling may improve the reversibility of the nitride electrodes. It has been shown in some cases that most of the irreversible changes occur at the very low voltage.

### 5.6 Acknowledgments

This work is based upon work supported as part of the Energy Materials Center at Cornell (EMC<sup>2</sup>), an Energy Frontier Research Center funded by the U.S. Department of Energy, Office of Science, and Office of Basic Energy Sciences under Award Number DE-SC0001086. This work made use of the Cornell Center for Materials Research Shared Facilities which are supported through the NSF MRSEC program (DMR-1120296). The authors would also like to thank Prof. Tessier (University of Rennes 1) for assistance with the elemental analysis measurements, and Dr. Minghui Yang (now professor at the Dalian Institute of Chemical Physics) for his nitride samples.

### REFERENCES

- (1) Whittingham, M. S. Electrical Energy Storage and Intercalation Chemistry. *Science* **1976**, *192*, 1126–1127.
- (2) Cabana, J.; Monconduit, L.; Larcher, D.; Palacín, M. R. Beyond Intercalation-Based Li-Ion Batteries: The State of the Art and Challenges of Electrode Materials Reacting Through Conversion Reactions. *Adv. Mater.* **2010**, *22*, E170–E192.
- (3) Tang, D.; Yi, R.; Gordin, M. L.; Melnyk, M.; Dai, F.; Chen, S.; Song, J.; Wang, D. Titanium Nitride Coating to Enhance the Performance of Silicon Nanoparticles as a Lithium-Ion Battery Anode. *J. Mater. Chem. A* **2014**.
- (4) Chan, C. K.; Peng, H.; Liu, G.; McIlwrath, K.; Zhang, X. F.; Huggins, R. A.; Cui, Y. High-performance lithium battery anodes using silicon nanowires. *Nat. Nanotechnol.* **2008**, *3*, 31–35.

- (5) Wu, H.; Chan, G.; Choi, J. W.; Ryu, I.; Yao, Y.; McDowell, M. T.; Lee, S. W.; Jackson, A.; Yang, Y.; Hu, L.; Cui, Y. Stable cycling of double-walled silicon nanotube battery anodes through solid-electrolyte interphase control. *Nat. Nanotechnol.* **2012**, *7*, 310–315.
- (6) Song, T.; Kil, K. C.; Jeon, Y.; Lee, S.; Shin, W. C.; Chung, B.; Kwon, K.; Paik, U. Nitridated Si–Ti–Ni alloy as an anode for Li rechargeable batteries. *J. Power Sources* **2014**, *253*, 282–286.
- (7) Yoshio, M.; Wang, H.; Fukuda, K.; Umeno, T.; Dimov, N.; Ogumi, Z. Carbon-Coated Si as a Lithium-Ion Battery Anode Material. *J. Electrochem. Soc.* **2002**, *149*, A1598–A1603.
- (8) Sun, Q.; Fu, Z.-W. An Anode Material of CrN for Lithium-Ion Batteries. *Electrochem. Solid-State Lett.* **2007**, *10*, A189–A193.
- (9) Sun, Q.; Fu, Z.-W. Vanadium nitride as a novel thin film anode material for rechargeable lithium batteries. *Electrochimica Acta* **2008**, *54*, 403–409.
- (10) Baggetto, L.; Verhaegh, N. A. M.; Niessen, R. A. H.; Roozeboom, F.; Jumas, J.-C.; Notten, P. H. L. Tin Nitride Thin Films as Negative Electrode Material for Lithium-Ion Solid-State Batteries. *J. Electrochem. Soc.* **2010**, *157*, A340–A347.
- (11) Nandi, D. K.; Sen, U. K.; Choudhury, D.; Mitra, S.; Sarkar, S. K. Atomic Layer Deposited Molybdenum Nitride Thin Film: A Promising Anode Material for Li Ion Batteries. *ACS Appl. Mater. Interfaces* **2014**, *6*, 6606–6615.
- (12) Nandi, D. K.; Sen, U. K.; Sinha, S.; Dhara, A.; Mitra, S.; Sarkar, S. K. Atomic layer deposited tungsten nitride thin films as a new lithium-ion battery anode. *Phys. Chem. Chem. Phys.* **2015**, *17*, 17445–17453.
- (13) Sun, Q.; Fu, Z.-W. Mn<sub>3</sub>N<sub>2</sub> as a novel negative electrode material for rechargeable lithium batteries. *Appl. Surf. Sci.* **2012**, *258*, 3197–3201.
- (14) Li, Y.; Yan, Y.; Ming, H.; Zheng, J. One-step synthesis Fe<sub>3</sub>N surface-modified Fe<sub>3</sub>O<sub>4</sub> nanoparticles with excellent lithium storage ability. *Appl. Surf. Sci.* **2014**, *305*, 683–688.
- (15) Pereira, N.; Klein, L. C.; Amatucci, G. G. The Electrochemistry of Zn<sub>3</sub>N<sub>2</sub> and LiZnN A Lithium Reaction Mechanism for Metal Nitride Electrodes. *J. Electrochem. Soc.* **2002**, *149*, A262–A271.
- (16) Nishijima, M.; Takeda, Y.; Imanishi, N.; Yamamoto, O.; Takano, M. Li Deintercalation and Structural Change in the Lithium Transition Metal Nitride Li<sub>3</sub>FeN<sub>2</sub>. *J. Solid State Chem.* **1994**, *113*, 205–210.
- (17) Takeda, Y.; Nishijima, M.; Yamahata, M.; Takeda, K.; Imanishi, N.; Yamamoto, O. Lithium secondary batteries using a lithium cobalt nitride, Li<sub>2.6</sub>Co<sub>0.4</sub>N, as the anode. *Solid State Ion.* **2000**, *130*, 61–69.
- (18) Nishijima, M.; Kagohashi, T.; Imanishi, M.; Takeda, Y.; Yamamoto, O.; Kondo, S. Synthesis and electrochemical studies of a new anode material, Li<sub>3</sub> – xCoxN. *Solid State Ion.* **1996**, *83*, 107–111.
- (19) Gillot, F.; Oró-Solé, J.; Palacín, M. R. Nickel nitride as negative electrode material for lithium ion batteries. *J. Mater. Chem.* **2011**, *21*, 9997–10002.
- (20) Cui, H.; Zhu, G.; Liu, X.; Liu, F.; Xie, Y.; Yang, C.; Lin, T.; Gu, H.; Huang, F. Niobium Nitride Nb<sub>4</sub>N<sub>5</sub> as a New High-Performance Electrode Material for Supercapacitors. *Adv. Sci.* **2015**, *2*, n/a–n/a.
- (21) Cong-Ming Ying; Lu-Qiang Xu; Zhi-Cheng Ju; Yi-Tai Qian Cubic Niobium Nitride Nanomaterials as Anode Materials in Lithium Ion Rechargeable Battery: Synthesis and Property. *Chin. J. Inorg. Chem.* **2012**, *28*, 2612–2616.
- (22) DeBeer, S. X-Ray Absorption Spectroscopy. In *Nitrogen Fixation; Methods in Molecular Biology*; Springer; Vol. 766, pp. 165–176.

- (23) Yang, M.; MacLeod, M. J.; Tessier, F.; DiSalvo, F. J. Mesoporous Metal Nitride Materials Prepared from Bulk Oxides. *J. Am. Ceram. Soc.* **2012**, *95*, 3084–3089.
- (24) Yang, M.; Ralston, W. T.; Tessier, F.; Allen, A. J.; DiSalvo, F. J. Mesoporous VN prepared by solid–solid phase separation. *J. Solid State Chem.* **2013**, *197*, 398–401.
- (25) Kiessling, R.; Peterson, L. The nitrides and oxide-nitrides of tungsten. *Acta Metall.* **1954**, *2*, 675–679.
- (26) Xu, S.; Wang, M.; Qiao, L.; Bing, J.; Zou, Q.; Zhao, Y. Enhancing the sintering ability of TiN<sub>x</sub> by introduction of nitrogen vacancy defects. *Ceram. Int.* **2015**, *41*, 9514–9520.
- (27) Hu, C.; Zhang, X.; Gu, Z.; Huang, H.; Zhang, S.; Fan, X.; Zhang, W.; Wei, Q.; Zheng, W. Negative effect of vacancies on cubic symmetry, hardness and conductivity in hafnium nitride films. *Scr. Mater.* **2015**, *108*, 141–146.
- (28) Shannon, R. D.; Prewitt, C. T. Effective ionic radii in oxides and fluorides. *Acta Crystallogr. B* **1969**, *25*, 925–946.
- (29) Shannon, R. D. Revised effective ionic radii and systematic studies of interatomic distances in halides and chalcogenides. *Acta Crystallogr. Sect. A* **1976**, *A32*, 751–767.
- (30) Friedrichs, O.; Martínez-Martínez, D.; Guilera, G.; Sánchez López, J. C.; Fernández, A. In Situ Energy-Dispersive XAS and XRD Study of the Superior Hydrogen Storage System MgH<sub>2</sub>/Nb<sub>2</sub>O<sub>5</sub>. *J. Phys. Chem. C* **2007**, *111*, 10700–10706.

## CHAPTER 6

### AN ATTEMPT TO SYNTHESIZE AND CHARACTERIZE IONICALLY CONDUCTIVE MATERIALS

#### 6.1 Introduction

*This chapter discusses an attempt to synthesize and characterize ionically conductive materials. While no positive result was obtained, there are some results that may be of value to future students. They are reported below.*

Lithium-ion batteries have become one of the most common energy storage systems in use, largely due to the high energy density, voltage and cyclability. Typical anode and the cathode reactions include:

Anode:  $\text{LiC}_6 \leftrightarrow \text{Li}^+ + \text{e}^- + \text{C}_6$  (theoretical capacity 372 mAh/g<sup>1</sup>, practical ~250 mAh/g)

Cathode:  $\text{Li}_{1-x}\text{CoO}_2 + x \text{Li}^+ + x \text{e}^- \leftrightarrow \text{LiCoO}_2$  (theoretical capacity 274 mAh/g, practical ~150 mAh/g<sup>2</sup>)

Engineering both electrodes to perform at their theoretical capacities is highly unlikely, since for  $x > 0.5$  in the second reaction written above may result in O<sub>2</sub> gas formation,<sup>1</sup> which can lead to major safety hazards). It is clear, then, that the energy density of lithium-ion batteries is unlikely to see significant gains in the future. As it stands, it is difficult to utilize this type of energy storage at large scale. For example, electric cars today are either very expensive and/or have shorter driving ranges than gasoline-based cars. Perhaps new battery chemistries will yield better performance.

One promising venue is to move away from the liquid electrolyte. In most lithium-ion batteries today, a lithium salt (such as LiPF<sub>6</sub> or LiTFSI) is dissolved in an organic solvent mixture (carbonate-based) is used as the electrolyte system. The solvents, however, are only kinetically stable over the operation voltages of most batteries.<sup>3,4</sup> In addition, organic solvents are flammable (combusts at around 230 °C<sup>5</sup>), meaning a thermal runaway can have

catastrophic consequences. Lastly, should carbon anodes be replaced with metallic lithium in batteries like lithium-sulfur batteries, dendrite formation giving rise to an electrical short represents a significant fire hazard.<sup>6</sup> Even polymer-based electrolytes<sup>7,8,9</sup> have problems with dendrites, as dendrites can eventually penetrate through the polymers<sup>10</sup>.

A solid state electrolyte could solve all of the issues listed above. Many oxides are stable over wide potential windows.<sup>11</sup> Most oxides are stable at 200-300 °C, as many of the synthetic processes to make them involve heating at much higher temperatures. Lastly, many oxides are hard, mechanically strong materials (though generally brittle), so dendrites are not able to penetrate through these materials. However, there has not been much research devoted to this area.

There are several battery systems that take advantage of these benefits. Sodium  $\beta''$ -alumina is used as the electrolyte in high-temperature molten sodium-sulfur batteries,<sup>12,13</sup> and the technology has even been commercialized as part of a renewable energy grid system in Aomori, Japan,<sup>14</sup> among other places. However, this technology cannot be used for non-stationary applications such as automobiles because the operating temperature is approximately 300 °C or higher.<sup>13</sup> Given that ions move at ca.  $D = 10^{-10-14}$  cm<sup>2</sup>/s in most solids at RT, it should not be surprising that there is currently no known oxide material that can conduct alkali metal ions at a sufficient rate ( $\sim 10^{-2}$  S/cm at RT).

In addition, many of the best solid ionic conductors, especially for lithium, are only kinetically stable in contact with alkali metals. Lithium has the lowest reduction potential of any metal (-3.0 V vs. SHE<sup>15</sup>), making it attractive for high-voltage batteries. It also means, however, that from a thermodynamic point of view, it will reduce most things that come in contact with it. Using the simplest approximation, the following must be true in order for an oxide (or any compound, by substituting O for N, P, etc.) to be thermodynamically stable upon contact with an alkali metal:



This holds for only a few binary metal oxides. Many of the known solid electrolytes for both Na and Li, such as NASICON type  $A_x M_2 (XO_4)_3$ <sup>1</sup> ( $A = Na^{16}$ ,  $Li$ ;  $M = V, Fe, Ti$ ;  $X = P, W, S$ ), LISICON-type  $Li_{14} Zn Ge_4 O_4$ <sup>17</sup> (and variants), thio-LISICON ( $Li_{10} Ge P_2 S_{12}$ <sup>18</sup> and its variants<sup>19</sup>) LiPON<sup>20</sup>,  $Li_3 PS_4$ ,<sup>21</sup> conductive glasses (both  $Na$ <sup>22,23</sup> and  $Li$ <sup>24,25,26</sup>), silicates<sup>27</sup> and others all fail to meet the criterion above. In fact, no sulfides or phosphides satisfy the requirement. Only the following oxides are stable against lithium and sodium (Fig. 6.1 (a) and (b), respectively):

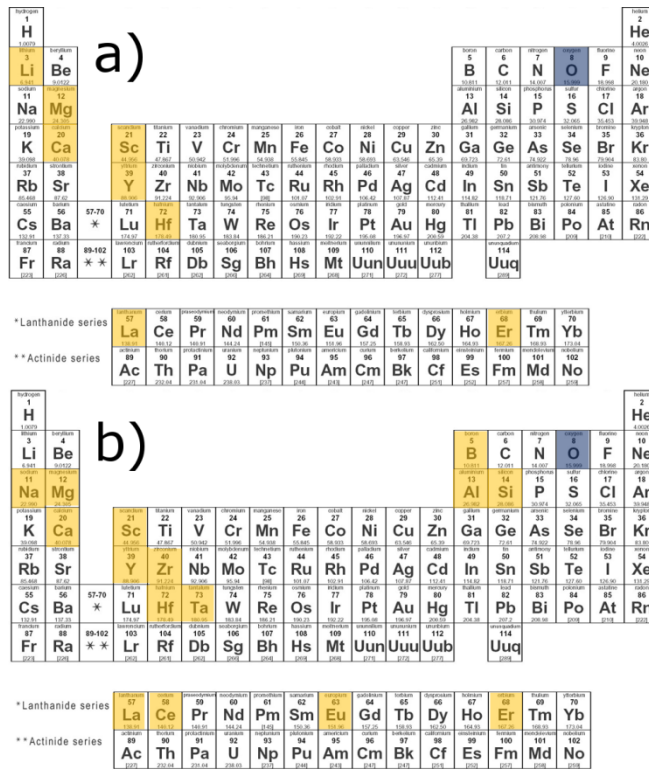


**Figure 6.1.** Binary metal oxides that are thermodynamically stable upon contact with metallic lithium (a) and metallic sodium (b) are highlighted in yellow.

Since it is unlikely that any of the known binary or ternary oxides of the metals highlighted in Figure 1 are good ionic conductors at room to moderate temperature, one would have to explore new quaternary compounds. Some exceptions exist, like sodium  $\beta''$ -alumina<sup>12,13,28,29</sup>. Garnet-like  $Li_7 La_3 Zr_2 O_{12}$ <sup>11,30</sup> is a known ionic conductor with  $\Delta G^\circ$  just below 0 ( $\Delta G^\circ = -57$  kJ/mol for reaction of  $ZrO_2$  and  $Li$ ). Both of them only conduct Na or Li at around  $10^{-3}$  S/cm,

and since doping is unlikely to dramatically improve their ionic conductivity, a completely new phase is likely needed to find a better ionic conductor at room temperature.

With all of these factors in mind, this chapter describes an effort to discover new phases of quaternary oxides that contain only the elements highlighted in Figure 6.1. A factor to consider here is the crystal structure. Typically, fast ionic conductors have either a channel-like structure through which the metal cations can rapidly diffuse (can either be 2-dimensional as in sodium  $\beta''$ -alumina<sup>12,13,28,29</sup> or 3-dimensional as in the NASICON structure<sup>31,32</sup>).

Alternatively, a network-like arrangement of alkali metal, as seen in the garnet-like  $\text{Li}_7\text{La}_3\text{Zr}_2\text{O}_{12}$ ,<sup>11,30</sup> is another possibility. Following these considerations, I first hypothesized that an ideal compound would have metals that typically have high coordination number (like 6 or 8 coordinate La) and a low coordination number (like 4 coordinate Al, for example). So, many of the systems that were investigated include these metals.

A method to measure ionic conductivity is also discussed in this chapter. Electronic and ionic conductivity in electrochemical systems are often characterized using electrochemical impedance spectroscopy (EIS). Unlike most electrochemical experiments, EIS is an alternating current (AC) experiment. From the perspective of electrochemistry, the greatest benefit of the method lies in the fact that resistance contributions from each components and phenomenon can be modeled. Every component in an electrochemical cell can be represented by an equivalent circuit, usually consisting of a combination of resistors, capacitors (or constant phase element, CPE, in non-ideal cases), and diffusion-controlled components (Warburg diffusion element). These components all respond differently to AC frequencies:

$$Z_{\text{resistor}} = R, \text{ independent of } \omega$$

$$Z_{\text{capacitor}}(\omega) = \frac{1}{j\omega C}$$

$$Z_{\text{CPE}}(\omega) = \frac{1}{Q_o \omega^n} \exp\left(-\frac{\pi}{2} ni\right), 0 < n < 1, Q_o = \frac{1}{|Z|} \text{ at } \omega = 1 \frac{\text{rad}}{\text{s}}$$

$$Z_{\text{Warburg}}(\omega) = \frac{A_W}{\sqrt{\omega}} - \frac{jA_W}{\sqrt{\omega}}$$

As written above, there are both real and imaginary components of the impedance in a typical circuit. Therefore, the impedance as a function of  $\omega$  are typically plotted with  $Z_{\text{real}}$  (sometimes written as  $Z'$ ) on the x axis and  $Z_{\text{imag}}$  (sometimes written as  $Z''$ ) on the y axis, called a Nyquist plot. By performing regression on the plot with a model, one can calculate the contribution of each component, such as bulk electrode resistance, grain boundary resistance, and double-layer capacitance. For the purpose of this work, the most important region of a Nyquist plot is the first x-intercept, where there is zero contribution of any capacitive response, meaning that the impedance corresponds directly to the bulk resistance of the electrode (or electrolyte).

There is no need to use elemental metal electrodes (lithium or sodium) to determine the ionic conductivity of the oxides. In most all-solid systems containing alkali metals, alkali metals are the most mobile components, so the responses from them dominate. This is called a blocking electrode experiment.<sup>33</sup> Finally, in order for the data to be considered valid, Kramers-Kronig transformation is applied to the data. It determines if the data are causal (response is solely due to the applied perturbation), has a linear response to frequency (which typically implies  $< 10$  mV AC, and usually smaller than  $RT/q$ ), returns to its original state after measurement (stability), and are finite for all frequencies.<sup>34</sup>

## **6.2 Experimental**

### **6.2.1 Synthesis**

The Pechini method<sup>35</sup> of oxide synthesis was used in most cases. Briefly, stoichiometric amounts of metal salts (generally adding up to approx. 0.001 mol), such as  $\text{Al}(\text{NO}_3)_3 \cdot 9\text{H}_2\text{O}$ ,  $\text{Ca}(\text{OH})_2$ ,  $\text{LiOH}$ ,  $\text{Na}_2\text{CO}_3$ ,  $\text{La}(\text{NO}_3)_3 \cdot 6\text{H}_2\text{O}$ , and  $\text{Mg}(\text{OH})_2$ , citric acid (at least 1x the total metal mol), and ethylene glycol (1x total metal mol) were dissolved in approx. 30

mL of water. Some of the metal salts listed above are not soluble in neutral pH water, but the addition of citric acid makes the solution sufficiently acidic for all of the metal salts to dissolve. Citric acid is a chelating agent that randomly chelates the metal cations to mix multiple species of cations at the atomic level, and ethylene glycol is a linking agent to link the citrates. The solution was stirred vigorously for at least 10 minutes. Then, 1.5 M  $\text{NH}_4\text{OH}$  was slowly added until the solution was neutralized. This was done so that the carboxylic acid groups on the citric acid were deprotonated, which is essential for chelation of the metal salt cations. The solution was then heated to 100 °C in a furnace to yield a solid product (usually brown), which was then calcined and annealed at various temperatures to obtain a white, powdered product.

Some metals, like Si, B, and Zr, are extremely difficult to dissolve in water under any conditions. In such cases, starting reagents, such as  $\text{SiO}_2$ ,  $\text{B}(\text{OH})_3$ ,  $\text{ZrO}_2$ ,  $\text{La}(\text{OH})_3$ ,  $\text{Y}_2\text{O}_3$ , and  $\text{Al}_2\text{O}_3$  were mixed thoroughly in a Pulverisette 7 (Fritsch) planetary mill, then pressed into pellets (5/16 in diameter) with 5 wt. % Butvar ® B-98 (Sigma) as an organic binder, and then heated at various temperatures (typically 900-1100 °C) in air. The binder is fluorine-free and combusts away during sintering.

### *6.2.2 Physical Characterization*

X-ray diffraction was performed using a Rigaku Ultima IV using  $\text{Cu K}_\alpha$  ( $\lambda=1.5406 \text{ \AA}$  for  $\text{K}_{\alpha 1}$ ,  $1.5444 \text{ \AA}$  for  $\text{K}_{\alpha 2}$ ). Refinement was done using PDXL (Rigaku) software. Scanning electron microscope images and energy-dispersive X-ray spectroscopy (EDX) were taken using a LEO Keck FESEM.

### *6.2.3 Ionic Conductivity Measurement*

A home-made apparatus (described below) was used to make electrical contact.

Electrochemical impedance spectroscopy (EIS) was performed using a Solartron 1280B potentiostat or a GAMRY Reference 3000. No DC voltage was applied and 5 mV of AC

voltage was applied, over a frequency range between 20,000 Hz to 1 Hz (Solartron) or 1,000,000 Hz to 1 Hz (GAMRY). In a typical experiment, no DC bias was applied, and 10-40 mV of AC bias was applied.

### **6.3 Results and Discussions**

#### *6.3.1 Development of Impedance Spectroscopy Methods*

Since no one in the Abruña group had previously worked on electrochemistry of all-solid systems, establishing an experimental protocol was necessary, though not trivial. First, having a good standard was important. We used a cast proprietary thin oxide film sample generously provided to us by Dr. Michael Badding (Corning), of thickness ca. 120  $\mu\text{m}$ . However, since we knew that we were unable to make pellets at this thickness (or density), we needed a pellet of known material as a standard, and  $\text{Li}_7\text{La}_3\text{Zr}_2\text{O}_{12}$  was chosen as the standard material. The synthesis was not trivial; often times, repeating procedures from the literature resulted in small but detectable amount of lanthanum oxide or lanthanum zirconium oxide impurities. After numerous modifications, it was found that making a pellet (ca. 0.02 in thick) with 5 wt. % binder (Butvar) and heating it at 600° C then 850 °C was the optimal procedure (see Figure 6.2). Even then, at least some portions of the sample crystallized in a tetragonal polymorph, which is less conductive than the cubic phase<sup>30</sup> (doublet peaks ca.  $2\theta = 26^\circ$ , etc. see Figure 6.2).

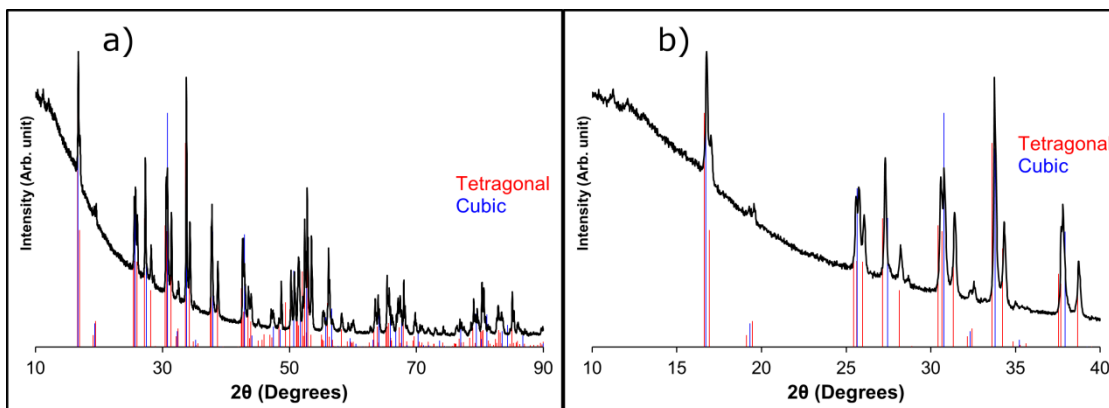


**Figure 6.2.** pXRD patterns of  $\text{Li}_7\text{La}_3\text{Zr}_2\text{O}_{12}$ . (b) is a zoom into  $10\text{-}40^\circ$ . Vertical lines are database peak locations for cubi and tetragonal polymorphs of  $\text{Li}_7\text{La}_3\text{Zr}_2\text{O}_{12}$ .

We also obtained the design for an electrochemical cell suitable for all-solid-state impedance spectroscopy from Dr. Badding (Corning Inc.). Figure 6.3 shows photographs of the cell. Copper was chosen as the material for the outer shell of the cell because it is inexpensive, easy to machine, and heavy. In order to prevent short circuit, copper pieces were wrapped with clear tape. Silver sheet was used as the electrical contact (“lead”) because silver is the most conductive metal. Nickel foam was used for both electrodes because deformable foams form a good contact with hard materials such as oxide pellets.



**Figure 6.3.** Images of the Electrochemical cell used for all-solid-state EIS.

Making a good electrical contact between the pellets and the cell was not trivial, either. The samples from Dr. Badding were all coated with evaporated Au, so we also sputtered Au on the center of the pellets by using a mask (aluminum with holes). In some cases, an additional Ag paste coating was applied.

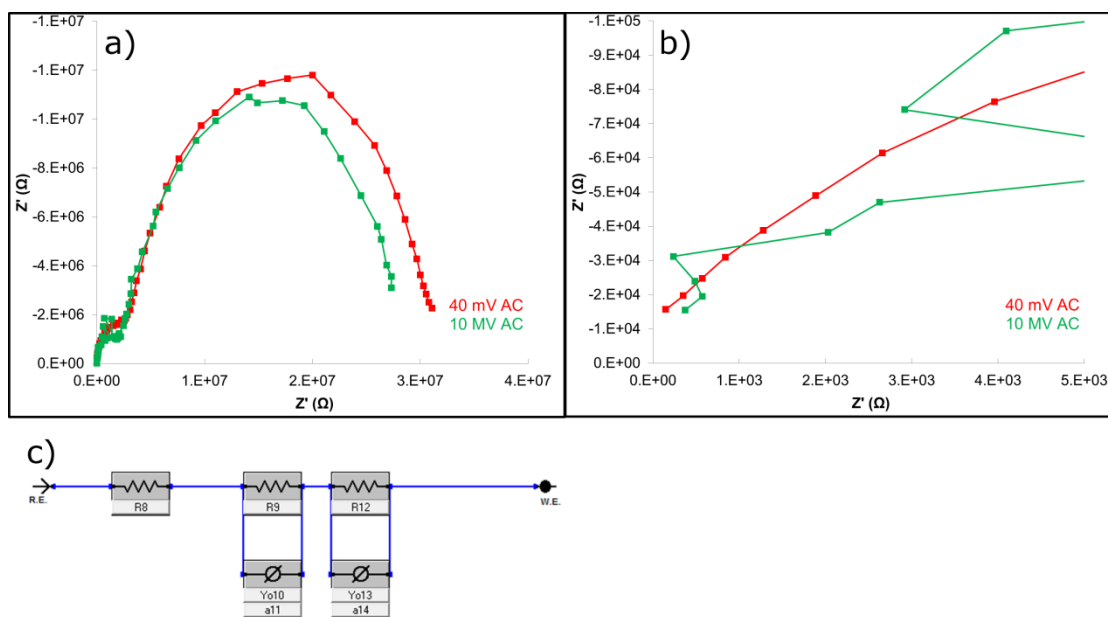


**Figure 6.4.** Nyquist Plot of  $\text{Li}_7\text{La}_3\text{Zr}_2\text{O}_{12}$ , taken at 40 mV AC (red) and 10 mV AC (green).

(b) is a zoomed-in plot of (a) at low  $Z'$  (or high frequency). AC frequency 1 MHz to 1 Hz ( $Z'$  and  $Z''$  increase as the frequency decreases) (c) is the model used for fitting

Figure 6.4 shows the Nyquist plot of  $\text{Li}_7\text{La}_3\text{Zr}_2\text{O}_{12}$  (0.021 in thick), taken at 10 mV and 40 mV AC (0 V DC). The use of a higher AC amplitude yields much more stable results at higher  $\omega$  (see Figure 6.4) This is not an unusual result with solid electrolytes.<sup>36</sup> The data fits Kramers-Kronig transformation well, indicating that the data obtained were valid.

Extrapolating from the first data point (highest  $\omega$ , or first x-axis of the semicircle if extrapolated), the conductivity of  $\text{Li}_7\text{La}_3\text{Zr}_2\text{O}_{12}$  was determined to be  $3.6 \times 10^{-4}$  S/cm at room temperature, in reasonable agreement with known values for the cubic  $\text{Li}_7\text{La}_3\text{Zr}_2\text{O}_{12}$ <sup>30,37</sup>. Using a model to fit the data (Figure 6.4 (c)), which is the more rigorous way of calculating resistance, yielded a significant uncertainty ( $1.98 \times 10^{-3} \pm 367$  Ω).

### 6.3.2 In search of New Ionic Conductors

Based on the criteria introduced above, I selected a few systems to study. One of the first unexplored quaternary spaces I decided to study was a  $\text{Li}_2\text{O-CaO-Al}_2\text{O}_3$  space. Although

$\text{Al}_2\text{O}_3$  is not an oxide highlighted in Figure 6.1,  $\Delta G^\circ$  is very small ( $\Delta G^\circ = -101.3\text{kJ/mol}$  for reaction of  $\text{Al}_2\text{O}_3$  and Li). In addition, a phase diagram of these compounds does not exist, and all three components are extremely inexpensive. I searched for new phases by mixing the three metal oxide precursors in various ratios and examining the pXRD patterns of the products. Figure 4.5 shows a 1:2:7 mixture of  $\text{Li}_2\text{O}$ - $\text{CaO}$ - $\text{Al}_2\text{O}_3$ , prepared via the Pechini method and heated at  $900^\circ\text{C}$ . Three known ternary phases ( $\text{LiAlO}_2$ ,  $\text{CaAlO}_4$ , and  $\text{LiAl}_5\text{O}_8$ ) can be indexed to all of the visible peaks. The Gibbs Phase Rule at constant pressure is  $C + 1 = F + P$  (where  $C$  = number of components,  $F$  = degrees of freedom, and  $P$  = number of phases). So,  $C = 3$  (exclude oxygen) and  $P = 3$  (as seen in Figure 6.5) yields 1 degree of freedom ( $T$ ), indicating that there cannot be any more phases at equilibrium. Therefore, within the triangle that has  $\text{LiAlO}_2$ ,  $\text{CaAlO}_4$  and  $\text{LiAl}_5\text{O}_8$  as corners (Figure 6.6), there is likely no new quaternary phase, at least under the synthetic conditions employed. Going through a similar process for all the points indicated with blue dots in Figure 4.6, I was able to conclude that no new quaternary phase of  $\text{Li}_2\text{O}$ - $\text{CaO}$ - $\text{Al}_2\text{O}_3$  exists. Peritectoid decomposition cannot be ruled out (i.e. a high-temperature only phase), but the furnaces in the lab are not well-equipped for a fast quench ( $>300^\circ\text{C}/\text{min}$ ), so the option was not explored further.

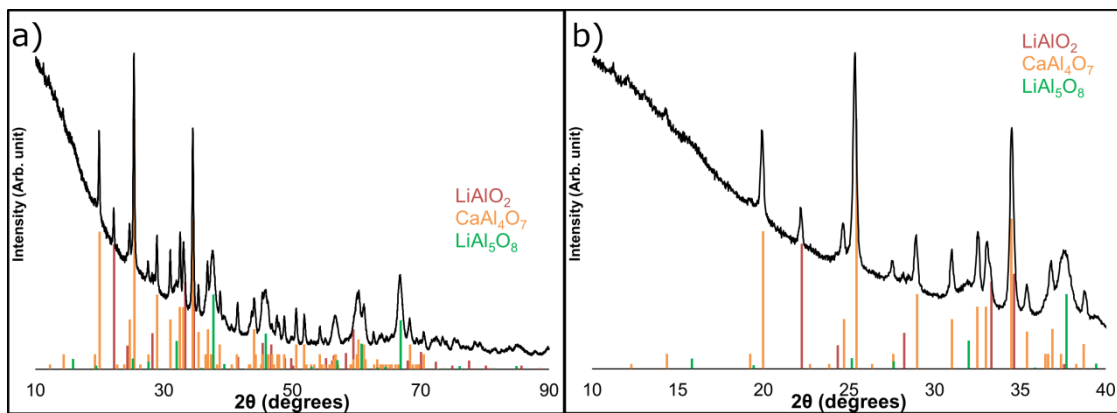


**Figure 6.5.** pXRD of mixture of  $\text{Li}_2\text{O}:\text{CaO}:\text{Al}_2\text{O}_3$  mixed in 1:2:7 ratio (using Pechini method), and heated at 900 °C. The vertical lines are database peak locations for the phases indicated. (b) is a zoomed version of (a).

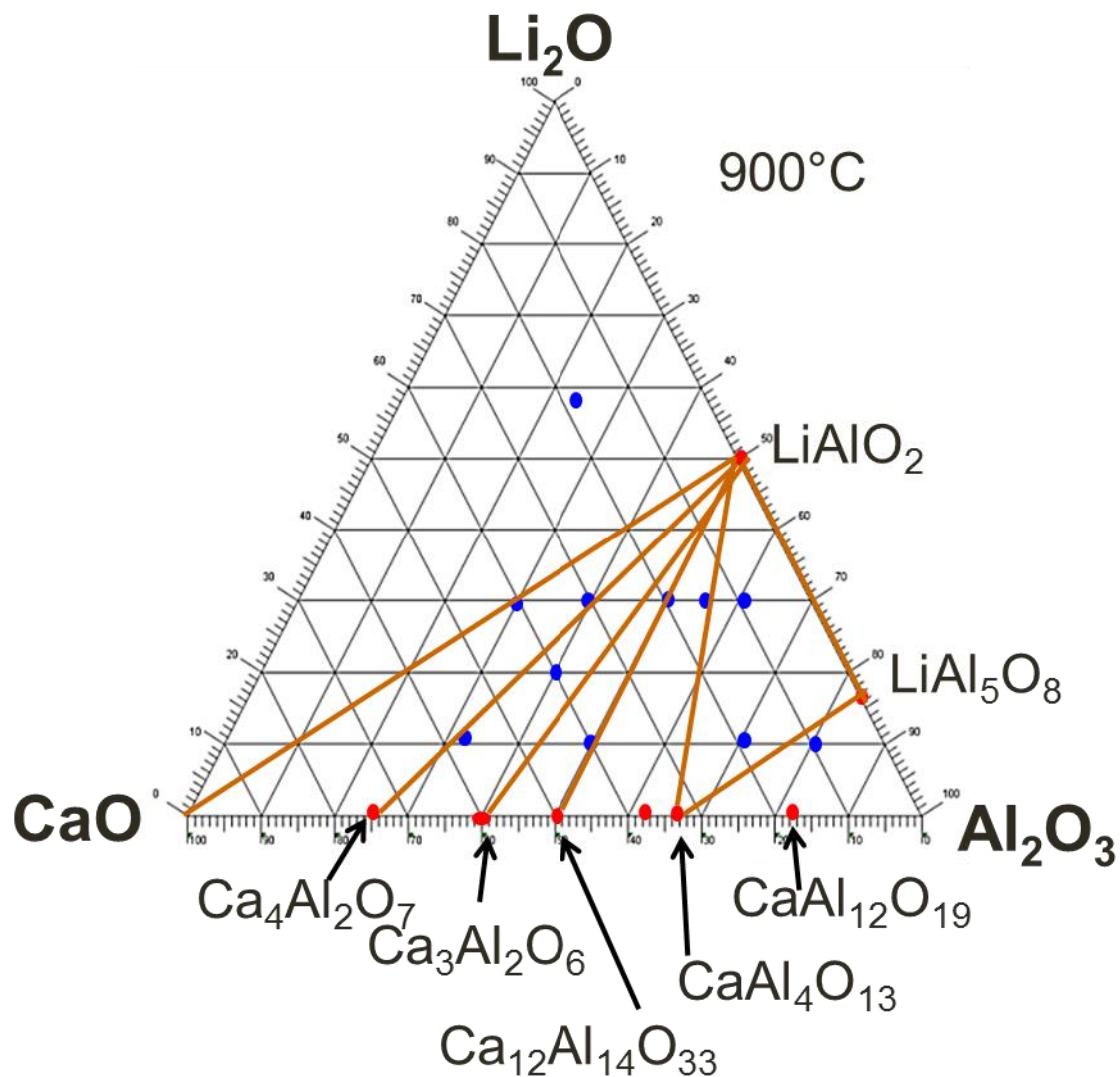


**Figure 6.6.** Phase diagram of  $\text{Li}_2\text{O}$ - $\text{CaO}$ - $\text{Al}_2\text{O}_3$ , at  $900\text{ }^\circ\text{C}$ . Blue dots: experimental reactant compositions; red dots = known phases, brown lines = sides of compatibility triangles implied from the obtained diffraction patterns.

A similar set of experiments was carried out for the  $\text{Na}_2\text{O}$ - $\text{La}_2\text{O}_3$ - $\text{Al}_2\text{O}_3$  system (Figure 6.8), using the Pechini method, but heating to a higher annealing temperature ( $1000\text{ }^\circ\text{C}$ ). No new phase was found. However, unlike the previous case, there were several  $\text{Na}_2\text{O}$ - $\text{La}_2\text{O}_3$ - $\text{Al}_2\text{O}_3$  ratios that only yielded peaks of one phase. The compositions circled in green only yielded  $\text{LaAlO}_3$  peaks (Figure 6.7), with weak secondary peaks seen. The sample

stoichiometry lies on the line between  $\text{Na}_2\text{O}$  and  $\text{LaAlO}$ .  $\text{Na}_2\text{O}$  likely would hydrolyze immediately on exposure to moisture in air to form  $\text{NaOH}$ , which is a deliquescent compound, so perhaps there was excess amorphous  $\text{NaOH}$  in the sample. Or, it could be that the structure factor of  $\text{Na}$  is far too small to be apparent. ( $57^2 \gg 11^2$ ).

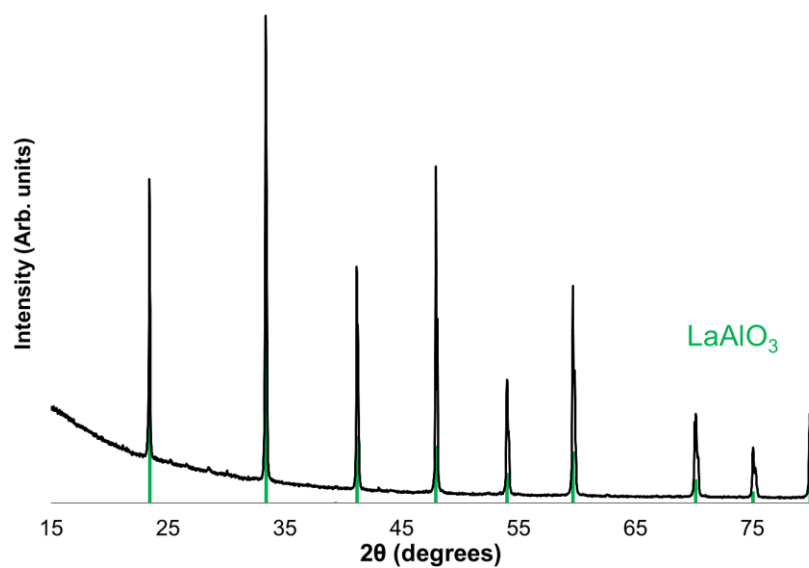


**Figure 6.7.** pXRD of mixture of  $\text{Na}_2\text{O}:\text{La}_2\text{O}_3:\text{Al}_2\text{O}_3$  mixed in 1:2:7 ratio (using Pechini method), and heated at 1000 °C. The vertical lines are database peak locations.

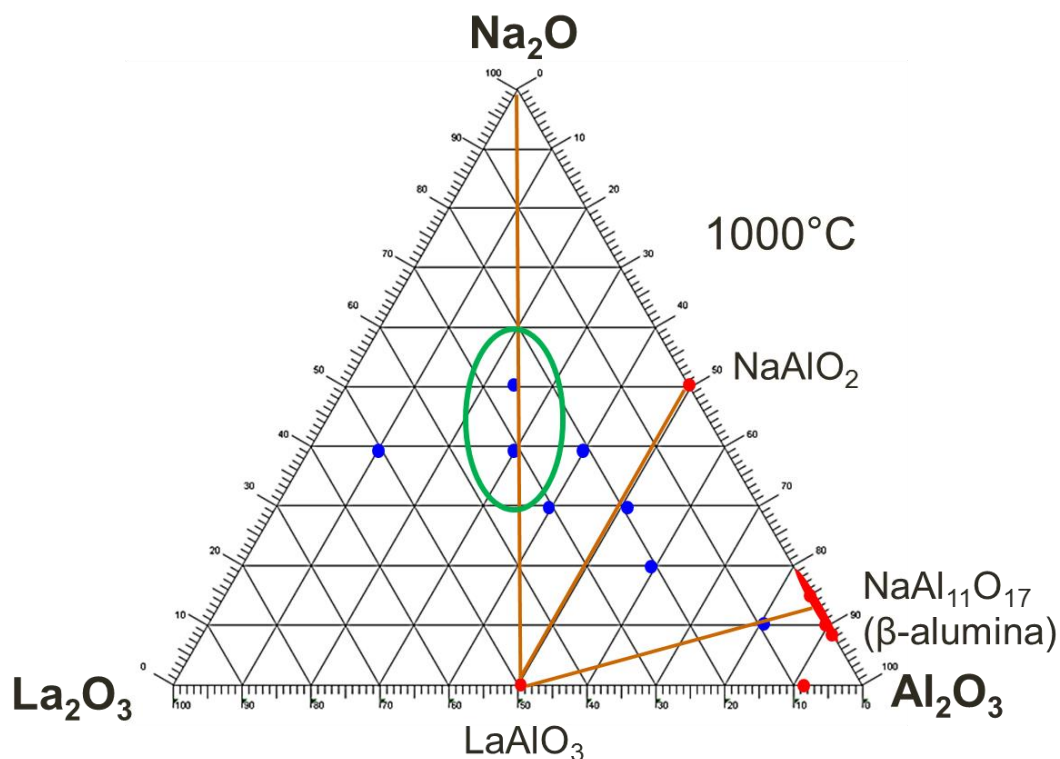


**Figure 6.8.** Phase diagram of  $\text{Na}_2\text{O}$ - $\text{La}_2\text{O}_3$ - $\text{Al}_2\text{O}_3$ , at 1000 °C. Blue dots: experimental reactant compositions, red dots = known phases, brown lines = sides of compatibility triangles, implied from the obtained diffraction peaks. Points circled in green only showed majority  $\text{LaAlO}_3$  peaks.

While data will not be presented here,  $\text{Na}_2\text{O}$ - $\text{Ta}_2\text{O}_5$ - $\text{Al}_2\text{O}_3$  and  $\text{Na}_2\text{O}$ - $\text{Y}_2\text{O}_3$ - $\text{Al}_2\text{O}_3$ , systems were also explored using similar methodologies. No new quaternary phases were discovered.

#### **6.4 Conclusions and Future Directions**

In the end, this project proved to be too big a challenge, so it was terminated to pursue other topics. I am not entirely certain that my hypothesis was right (high coordination number means close packing, which is nice if the alkali metals form a network as a result, but that is far from certain). Also, this project proved to be incredibly time consuming. Aside from the thermodynamic stability criterion, the method chosen was fairly close to a blind guess with

multiple variables, including compositions and annealing temperatures. No new phase was found. However, under different conditions or with a larger effort, perhaps interesting phases could be found.

Even the development of the EIS characterization method proved to be much more difficult and time-consuming than initially anticipated, even with tremendous help from Dr. Badding. Electrical contact to the pellet surfaces proved to be extremely difficult and variable, but a combination of sputtering and increase in the pellet density, via addition of a combustible binder (Butvar), proved to be useful. Given more time and/or knowledge, perhaps I could have developed a casting method similar to that done by Dr. Badding. Combined with the fact that a new phase was incredibly difficult to find, though, it was probably in my best interest to not spend extra time on this part.

Also, with metals that can be dissolved in water, a slightly more high-throughput approach may be of interest. Making stock solutions of each metal salts (with appropriate amount of citric acid) and taking aliquots, somewhat like the work done by the Abruña group in my time,<sup>38</sup> is a strategy I briefly considered, but never materialized.

### ***6.5 Acknowledgements***

This work is based upon work supported as part of the Energy Materials Center at Cornell (EMC<sup>2</sup>), an Energy Frontier Research Center funded by the U.S. Department of Energy, Office of Science, and Office of Basic Energy Sciences under Award Number DE-SC0001086.

The authors would like to thank Dr. Michael Badding (Corning Inc.) for his generosity in providing us with standard samples as well as the design for the impedance spectroscopy cell. The authors would like to thank Steve Kriske for his assistance with the CCMR sputtering measurements. This work made use of the Cornell Center for Materials Research Shared Facilities which are supported through the NSF MRSEC program (DMR-1120296)

## REFERENCES

- (1) Croguennec, L.; Palacin, M. R. Recent Achievements on Inorganic Electrode Materials for Lithium-Ion Batteries. *J. Am. Chem. Soc.* **2015**, *137*, 3140–3156.
- (2) Melot, B. C.; Tarascon, J.-M. Design and Preparation of Materials for Advanced Electrochemical Storage. *Acc. Chem. Res.* **2013**, *46*, 1226–1238.
- (3) Goodenough, J. B. Rechargeable batteries: challenges old and new. *J. Solid State Electrochem.* **2012**, *16*, 2019–2029.
- (4) Asl, N. M.; Keith, J.; Lim, C.; Zhu, L.; Kim, Y. Inorganic solid/organic liquid hybrid electrolyte for use in Li-ion battery. *Electrochimica Acta* **2012**, *79*, 8–16.
- (5) Biensan, P.; Simon, B.; Pérès, J. ; de Guibert, A.; Broussely, M.; Bodet, J. . ; Perton, F. On safety of lithium-ion cells. *J. Power Sources* **1999**, *81–82*, 906–912.
- (6) Crowther, O.; West, A. C. Effect of Electrolyte Composition on Lithium Dendrite Growth. *J. Electrochem. Soc.* **2008**, *155*, A806–A811.
- (7) Kezuka, K.; Hatazawa, T.; Nakajima, K. The status of Sony Li-ion polymer battery. *J. Power Sources* **2001**, *97–98*, 755–757.
- (8) Baskakova, Y. V.; Yarmolenko, O. V.; Efimov, O. N. Polymer gel electrolytes for lithium batteries. *Russ. Chem. Rev.* **2012**, *81*, 367.
- (9) Yoshimoto, N.; Yakushiji, S.; Ishikawa, M.; Morita, M. Rechargeable magnesium batteries with polymeric gel electrolytes containing magnesium salts. *Electrochimica Acta* **2003**, *48*, 2317–2322.
- (10) Brissot, C.; Rosso, M.; Chazalviel, J.-N.; Lascaud, S. Dendritic growth mechanisms in lithium/polymer cells. *J. Power Sources* **1999**, *81–82*, 925–929.
- (11) Ohta, S.; Kobayashi, T.; Asaoka, T. High lithium ionic conductivity in the garnet-type oxide  $\text{Li}_{7-X}\text{La}_3(\text{Zr}_{2-X}\text{Nb}_X)\text{O}_{12}$  ( $X = 0-2$ ). *J. Power Sources* **2011**, *196*, 3342–3345.
- (12) Folly, J.; Lasne, C.; Lazennec, Y. von; Cars, Y. L.; Margotin, P. Study of a Beta-Alumina Electrolyte for Sodium-Sulfur Battery. *J. Electrochem. Soc.* **1973**, *120*, 1296–1298.
- (13) Lu, X.; Xia, G.; Lemmon, J. P.; Yang, Z. Advanced materials for sodium-beta alumina batteries: Status, challenges and perspectives. *J. Power Sources* **2010**, *195*, 2431–2442.
- (14) Rokkasho village, Aomori, Japan | Case Studies | NAS  
[https://www.ngk.co.jp/nas/case\\_studies/rokkasho/](https://www.ngk.co.jp/nas/case_studies/rokkasho/) (accessed Apr 16, 2016).
- (15) Xu, K. Nonaqueous Liquid Electrolytes for Lithium-Based Rechargeable Batteries. *Chem. Rev.* **2004**, *104*, 4303–4418.
- (16) Lalère, F.; Leriche, J. B.; Courty, M.; Boulineau, S.; Viallet, V.; Masquelier, C.; Seznec, V. An all-solid state NASICON sodium battery operating at 200°C. *J. Power Sources*.
- (17) Bruce, P. G.; West, A. R. Ionic conductivity of LISICON solid solutions,  $\text{Li}_2+2x\text{Zn}_{1-x}\text{GeO}_4$ . *J. Solid State Chem.* **1982**, *44*, 354–365.
- (18) Hassoun, J.; Verrelli, R.; Reale, P.; Panero, S.; Mariotto, G.; Greenbaum, S.; Scrosati, B. A structural, spectroscopic and electrochemical study of a lithium ion conducting  $\text{Li}_{10}\text{GeP}_2\text{S}_{12}$  solid electrolyte. *J. Power Sources* **2013**, *229*, 117–122.
- (19) Wang, Y.; Liu, Z.; Zhu, X.; Tang, Y.; Huang, F. Highly lithium-ion conductive thio-LISICON thin film processed by low-temperature solution method. *J. Power Sources* **2013**, *224*, 225–229.
- (20) West, W. . ; Whitacre, J. . ; Lim, J. . Chemical stability enhancement of lithium conducting solid electrolyte plates using sputtered LiPON thin films. *J. Power Sources* **2004**, *126*, 134–138.

- (21) Lin, Z.; Liu, Z.; Dudney, N. J.; Liang, C. Lithium Superionic Sulfide Cathode for All-Solid Lithium–Sulfur Batteries. *ACS Nano* **2013**, *7*, 2829–2833.
- (22) Mahani, R. M.; Marzouk, S. Y. AC conductivity and dielectric properties of SiO<sub>2</sub>–Na<sub>2</sub>O–B<sub>2</sub>O<sub>3</sub>–Gd<sub>2</sub>O<sub>3</sub> glasses. *J. Alloys Compd.* **2013**, *579*, 394–400.
- (23) Martin, S. W. Conductivity Activation Energy Relations in High-Sodium-Content Borate and Aluminoborate Glasses. *J. Am. Ceram. Soc.* **1988**, *71*, 438–445.
- (24) Bauer, U.; Welsch, A.-M.; Behrens, H.; Rahn, J.; Schmidt, H.; Horn, I. Li Diffusion and the Effect of Local Structure on Li Mobility in Li<sub>2</sub>O–SiO<sub>2</sub> Glasses. *J. Phys. Chem. B* **2013**, *117*, 15184–15195.
- (25) Das, S. S.; Srivastava, P. K.; Singh, N. B. Fast ion conducting phosphate glasses and glass ceramic composites: Promising materials for solid state batteries. *J. Non-Cryst. Solids* **2012**, *358*, 2841–2846.
- (26) Thokchom, J. S.; Kumar, B. Water Durable Lithium Ion Conducting Composite Membranes from the Li<sub>2</sub>O - Al<sub>2</sub>O<sub>3</sub> - TiO<sub>2</sub> - P<sub>2</sub>O<sub>5</sub> Glass-Ceramic. *J. Electrochem. Soc.* **2007**, *154*, A331–A336.
- (27) Shannon, R. D.; Taylor, B. E.; Gier, T. E.; Chen, H. Y.; Berzins, T. Ionic conductivity in sodium yttrium silicon oxide (Na<sub>5</sub>YSi<sub>4</sub>O<sub>12</sub>)-type silicates. *Inorg. Chem.* **1978**, *17*, 958–964.
- (28) Kennedy, J. H.; Sammells, A. F. Conductivity of Beta-Alumina and Its Dependence on Sodium and Magnesium Content. *J. Electrochem. Soc.* **1972**, *119*, 1609–1613.
- (29) Kim, K. K.; Mundy, J. N.; Chen, W. K. Diffusion and ionic conductivity in sodium beta alumina. *J. Phys. Chem. Solids* **1979**, *40*, 743–755.
- (30) Kokal, I.; Somer, M.; Notten, P. H. L.; Hintzen, H. T. Sol–gel synthesis and lithium ion conductivity of Li<sub>7</sub>La<sub>3</sub>Zr<sub>2</sub>O<sub>12</sub> with garnet-related type structure. *Solid State Ion.* **2011**, *185*, 42–46.
- (31) Xie, H.; Li, Y.; Goodenough, J. B. NASICON-type Li<sub>1+2x</sub>Zr<sub>2-x</sub>Ca<sub>x</sub>(PO<sub>4</sub>)<sub>3</sub> with high ionic conductivity at room temperature. *RSC Adv.* **2011**, *1*, 1728–1731.
- (32) Kabbour, H.; Coillot, D.; Colmont, M.; Masquelier, C.; Mentré, O.  $\alpha$ -Na<sub>3</sub>M<sub>2</sub>(PO<sub>4</sub>)<sub>3</sub> (M = Ti, Fe): Absolute Cationic Ordering in NASICON-Type Phases. *J. Am. Chem. Soc.* **2011**, *133*, 11900–11903.
- (33) Huang, V. M.-W.; Vivier, V.; Frateur, I.; Orazem, M. E.; Tribollet, B. The Global and Local Impedance Response of a Blocking Disk Electrode with Local Constant-Phase-Element Behavior. *J. Electrochem. Soc.* **2007**, *154*, C89–C98.
- (34) Boukamp, B. A. Electrochemical impedance spectroscopy in solid state ionics: recent advances. *Solid State Ion.* **2004**, *169*, 65–73.
- (35) Pechini, M. Method of preparing lead and alkaline earth titanates and niobates and coating method using the same to form a capacitor **1967**.
- (36) Victoria, S. N.; Ramanathan, S. Effect of potential drifts and ac amplitude on the electrochemical impedance spectra. *Electrochimica Acta* **2011**, *56*, 2606–2615.
- (37) Gu, W.; Ezbiri, M.; Prasada Rao, R.; Avdeev, M.; Adams, S. Effects of penta- and trivalent dopants on structure and conductivity of Li<sub>7</sub>La<sub>3</sub>Zr<sub>2</sub>O<sub>12</sub>. *Solid State Ion.* **2015**, *274*, 100–105.
- (38) Almeida, T. S.; Van Wassen, A. R.; VanDover, R. B.; de Andrade, A. R.; Abruña, H. D. Combinatorial PtSnM (M = Fe, Ni, Ru and Pd) nanoparticle catalyst library toward ethanol electrooxidation. *J. Power Sources* **2015**, *284*, 623–630.

## CHAPTER 7

### CONCLUDING REMARKS

This dissertation has presented very collaborative efforts to synthesize and characterize various oxide and nitrides to be used in fuel cells and batteries. Some of the materials studied may be attractive alternatives for existing materials and components.

In Chapter 2, the synthesis  $Ti_xTa_yAl_zN_{1-\delta}O_\gamma$  of various compositions was presented, and characterized to be used as catalyst supports in PEMFC. It was discovered that the nitride products are much more complicated than generally assumed, in that they have high cationic defect densities and various levels of oxygen as well as nitrogen content depending on the amount of Ta and Al ions. It was also discovered that the addition of Ta greatly improves the materials' electrochemical stability, despite the fact that the electrical conductivity decreases by 30-50 %.

In Chapter 3, a simple, facile, yet effective method to turn thin film samples into RDE electrodes was presented. The design and constructions of a novel apparatus was discussed. The apparatus was used in a collaborative effort for the exploration of novel thin film oxide catalysts. I firmly believe that it will be a useful tool for the Abruña group as the group further continues its efforts in electrocatalysis.

In Chapter 4, using the results from Chapter 3 as a guide, I presented the synthesis of  $Mn_xRu_{1-x}O_2$ , a previously unknown solid solution. Not only is it the first solid solution of manganese and ruthenium oxides, it showed a remarkable activity towards the ORR and the OER. This was especially notable because the oxide is significantly less expensive than platinum. It was also shown that, strictly for catalysis,

it needs not be a single-phase product to achieve the high activity. This chapter was also a perfect demonstration of the benefits of being co-advised by a solid state chemist and an electrochemist, as well as the power of collaborative efforts encouraged by Profs. DiSalvo and Abruña.

In Chapter 5, an exploratory effort to use metal nitrides as high-capacity lithium-ion battery anodes was presented. While the performance of the materials was not as good as hoped, physical characterization results combined with *operando* coin cell testing/X-ray techniques showed that the mechanism of charge and discharge may heavily involve vacancies that are created upon ammonolysis of oxide precursors. This was an unexpected result that went against the conventional wisdom on reaction of lithium with nitrides.

In Chapter 6, an attempt to invent new alkali oxide-containing phases that may be useful as a solid state electrolyte was presented. Unfortunately, there were too many challenges to overcome. Perhaps a second look is worth the effort, as the promise is tantalizing, but it would likely be far easier to focus on small changes to existing structures (or compounds) rather than a discovery of a new phase that also happens to be ionically conductive.

It must be stressed that none of the work presented in this dissertation would have been possible without collaborative efforts with other students and postdoctoral associates, both within and outside of the DiSalvo and the Abruña groups (please refer to each chapter for specific collaborators). It is my sincere hope that the results presented in this dissertation will be of great help to future researchers. Specifically, I believe that the  $\text{Mn}_x\text{Ru}_{1-x}\text{O}_2$  work presented in Chapter 4 is worth further investigation.

Addition of another *3d* metal like Fe, which my collaborator has already begun investigating as of this writing, or replacing ruthenium with a more inexpensive (likely *3d*) metal, would make the material even more attractive. Furthermore, the procedure to load the metal oxide catalyst on carbon black, the catalyst weight loading on carbon black, and the catalyst ink recipe can all be improved and engineered so as to improve the electrochemical stability (see Figure 5.4). The optimized oxide/carbon matrix should be an attractive candidate to be tested in an MEA stack as well.